eman ta zabal zazu

euskal herriko
unibertsitatea

universidad
del pais vasco

Structural Relaxation and Chain Dynamics in Polymer Melts: a Computational Investigation on the Role of the Intramolecular Barriers

by

Marco Bernabei

Thesis Director:
Dr. Ángel José Moreno Segurado

Donostia-San Sebastián, 2011

© Servicio Editorial de la Universidad del País Vasco
Euskal Herriko Unibertsitateko Argitalpen Zerbitzua

ISBN: 978-84-694-5815-0

Structural Relaxation and Chain Dynamics in Polymer Melts: a Computational Investigation on the Role of the Intramolecular Barriers

by

Marco Bernabei

Thesis director:

Ángel José Moreno Segurado

A Franca, Pietro e i miei fratelli

Acknowledgements

Quisiera antes de nada mostrar mi profunda gratitud al director de esta tesis, el Dr. Ángel José Moreno Segurado, por haber dirigido mi trabajo con experiencia, competencia y sobre todo pasión. Gracias Ángel por haberme enseñado, en estos tres años y medio, lo que significa hacer ciencia. También quisiera mostrarle mi agradecimiento al Prof. Juan Colmenero, por haberme dado la posibilidad de incorporarme y trabajar en el grupo de investigación dirigido por él, y de crecer desde un punto de vista tanto científico y profesional como humano. Otro importante agradecimiento va a la fundación Donostia International Physics Center y al Prof. Pedro Echenique en calidad de presidente, por el apoyo económico e institucional, imprescindibles para la consecución de esta Tesis.

Me gustaría darle las gracias a todos los compañeros y amigos del trabajo, que me han acompañado en esta aventura científica: mis compañeros de despacho Lourdes, Sandra, Petra, Mario y Zakaria; los amigos del Master y del doctorado Giuseppe, Itziar, Izaro, Elton, Eneko, Leonardo, Juan Pablo, Fernando, Ali, Lourdes, Sandra, Txabo, Johanna y Jessica; los amigos de las comidas de los viernes Marisa, Nora, Claudio, Fabienne, Virginie, Alejandro; compañeros del cafe de la tarde; los del centro de calculo Txomin, Belen, Carmen, Iñigo, Zuriñe, gracias por vuestra siempre amable disponibilidad en resolver mis pequeños y grandes problemas informáticos; Ekaitz el brazo duro de la ley, por ser un buen amigo y cuidar de mi moto; las de la administración y de la secretaría del DIPC y CFM, en particular Ana, Marimar y Eli, mi primera compañera de despacho, si conozco algunas palabras de euskera, se lo debo a ella; los amigos y compañeros del grupo: Gustavo, Silvina, Daniele, Reidar, Arantxa, Silvia, Dimas, Roberto y Sara (soprattutto a te Sara grazie, per i preziosi consigli iniziali, per le risate, gli sfoghi, i rodimenti e le allegrie, e le ruote che non abbiamo mai mangiato). Gracias a todos ustedes por vuestro apoyo, vuestra amistad, y por haber compartido conmigo momentos agradables.

Un agradecimiento más que especial va para mi 'cuadrilla', mis amigos fraternos y hermanos del 'clan': José, Juan Pablo 'Patxi' y Diana, Leonardo 'Txema'. Grandi uomini. Gracias chicos, simplemente no tengo palabras. Además me gustaría darle las gracias a los amigos del otro lado del charco: los amigos de 'Sin Payola' y en particular Rose Fatima. Gracias Xhunca por haber estado siempre ahí apoyándome, aconsejándome y aguantándome aunque a la distancia.

Un último agradecimiento va a todo los amigos, que he tenido el placer de encontrar y conocer durante todo este tiempo, los que no son del gremio, y que con curiosidad siempre han estado preguntando: '¿me explicas en dos palabras de que va tu tesis?¿ Che, inventaste algo nuevo con los polímeros?': Leo y Ernesto mi familia argentina en Donostia; la familia artística y musical del Leize; Martin y Laura mis amigos made in UK.

Un ringraziamento speciale va al Prof. Francesco Sciortino e la Dr. Emanuela Zaccarelli, per avermi dato la possibilità di lavorare nel loro gruppo e per il loro fondamentale contributo, scientifico e umano, a questa tesi.

Vorrei ringraziare i miei genitori Pietro e Franca, i miei fratelli Salvatore, Alessia, Ornella e Andrea, mia cognata Chiara e mia nipote Sara. Un sincero e profondo grazie a tutti voi, per il vostro appoggio incondizionato, per aver creduto in me, per essere stati sempre presenti, anche se lontano e in silenzio. Vi voglio bene.

Un grazie speciale va alla mia famigliola qui a San Sebastián: Sara, Fabio, Sofia e Flavia. Saranno sempre poche le parole per esprimervi la mia profonda gratitudine e il mio profondo affetto.

San Sebastián, April de 2011

Marco Bernabei

Contents

Introduction

0.1 Complex Dynamics in Soft Matter

0.1.1 The Problem of the Glass Transition

Let us consider a system in its liquid state. At high temperatures it can be expected that the viscosity η is small and that the typical relaxation time τ is microscopic, i.e. it is of the order of a typical vibrational period of the system. If the system is cooled down it undergoes a first-order phase transition at its melting temperature T_m, i.e. it crystallizes. However it is found that most liquids can be cooled down below T_m, in a metastable regime. These liquids, for which crystallization has been bypassed, are known as 'supercooled liquids'. As a supercooled liquid is cooled down to lower temperatures, its viscosity rapidly increases [1], and its molecules move and rearrange more and more slowly. When this structural rearrangements cannot follow the cooling rate, the liquid falls out of equilibrium [2]. Its structure therefore appears 'frozen' on the laboratory time scale (for example, minutes). This phenomenon, known as the glass transition, takes place on a temperature range which depends on the experimental cooling conditions. Usually this temperature range is represented by only one temperature, the glass transition temperature T_g. In practice T_g can be defined as the temperature at which the viscosity reaches the value of $\eta = 10^{13}$ poise (= 10^{12} Pa s), or also as that for which the structural relaxation time is 100 seconds. From a practical point of view glasses can be considered as 'stable' solids, because they can sustain static shear stress, but on the other hand they lack the spatial long-range order that is characteristic for crystalline solids, and the static structure factors (chapter 1) show the behaviour of a typical dense disordered system. From looking at a single snapshot of the system one cannot distinguish if the system is in its glassy or fluid state. Many experiments and computer simulations have shown that the structural as well as the thermodynamical properties of supercooled liquids show only a relatively weak temperature dependence, and that in principle this dependence can be extrapolated smoothly from the data above T_m. No divergence of thermodynamic quantites is observed when approaching the liquid-glass tansition. In this sense the laboratory liquid-glass transition is not really a thermodynamic phase transition. If structural and thermodynamic properties change weakly with temperature, this is not the case for most dynamic properties, like viscosity or relaxation times. In figure 1 we show an example, for a canonical glass-former (orthoterphenyl) of the strong T-dependence of the viscosity $\eta(T)$, accompanied by just a weak T-dependence of the static structure factor [3]. We see that a small change in temperature leads to a small change in the structure of the system, and at the same time, to an increase of $\eta(T)$ of about 10 decades.

Let us discuss now the main features distinguishing the dynamical behaviour of a glass-forming system and a simple liquid. In fig. 2 we show a schematic representation of the time dependence of a typical correlation funcion $\phi(t)$ (e.g., the density-density correlator discussed in chapter 2). The two curves correspond to two temperatures: one at which the system is in its normal liquid state and one at which it relaxes only slowly. At the high temperature, $\phi(t)$ decays in a single step at short time. After the inital 'ballistic regime', $\phi(t)$ enters the so-called 'microscopic regime' governed by the interaction between particles. For longer times the t-dependence of the correlation function is well approximated by an exponential function. At low temperature $\phi(t)$ shows a more complex time dependence. At short times one finds the ballistic regime followed by the microscopic regime. At intermediate times the correlator shows a plateau. This time window is called β-relaxation. After longer time the correlator decays from the plateau to zero. This time window is called α-relaxation. Note that the early part of the α-relaxation coincides with the last part of the β-relaxation. The physical meaning of the plateau is given by the so-called 'cage effect'. For intermediate times each particle is trapped by its neighbours and hence the correlator is almost constant. Only for much longer times the particles are able to leave the cage, due to cooperative rearrangement of the particles, and hence the correlator decays to zero. In contrast with the case at high T, the final decay of the correlation function is non-exponential. One usually finds that the shape of the decay is described by an empirical Kohlrausch-Williams-Watts (KWW) function, $\propto \exp[-(t/\tau)^\beta]$, with $\beta < 1$.

It is the aim of the Mode Coupling Theory of the glass transition (MCT) [4–8] to

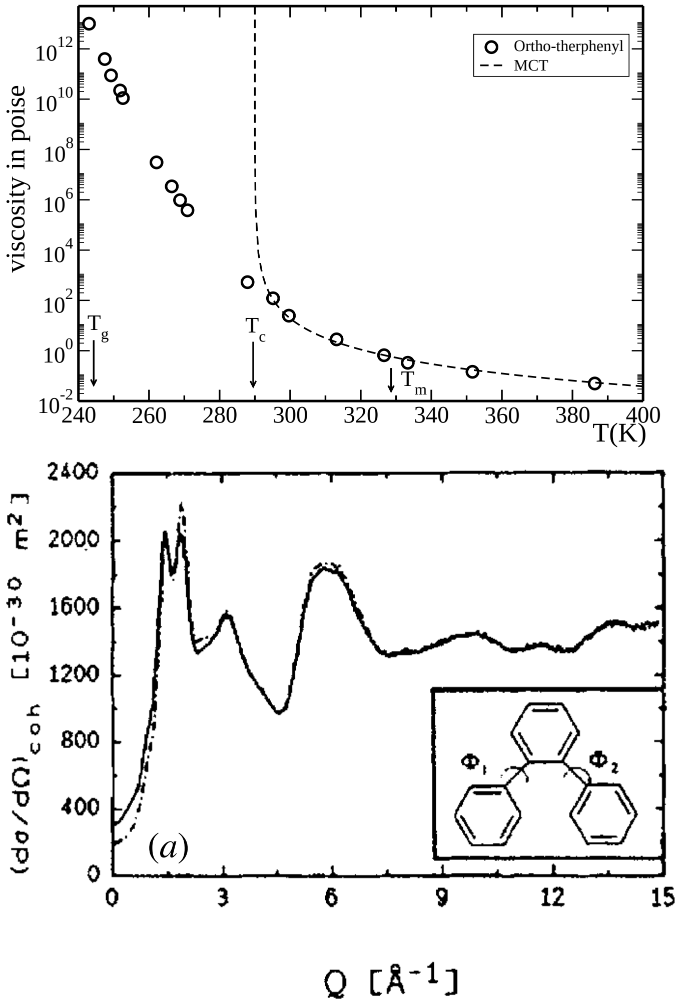

Figure 1: Upper panel: temperature dependence of the viscosity for the orthoterphenyl (OTP). The glass transition temperature, defined by the relation $\eta(T_g) = 10^{13}$ poise is $T_g \simeq 243K$. The melting temperature $T_m = 329K$ and critical MCT temperature $T_c = 290K$ are also indicated. The dashed line represents a fit to the MCT power law $\eta(T) \sim (T - T_c)^{-2.59}$ Lower panel: static structure factor of fully deuterated OTP at $314K$ (full curve) and $255K$ (dashed-dotted curve).

capture these nontrivial features of the dynamics of a liquid in the *weakly* supercooled regime (see below). The MCT is a first-principle theory which predicts the behaviour of dynamic correlators from the knowledge of the static correlations of the system. In the idealized version of MCT, the liquid-glass transition is a dynamic transition induced by the slowing down of the density fluctuations and occurs at a critical transition temperature T_c. Approaching T_c from above MCT predicts divergence of viscosity and

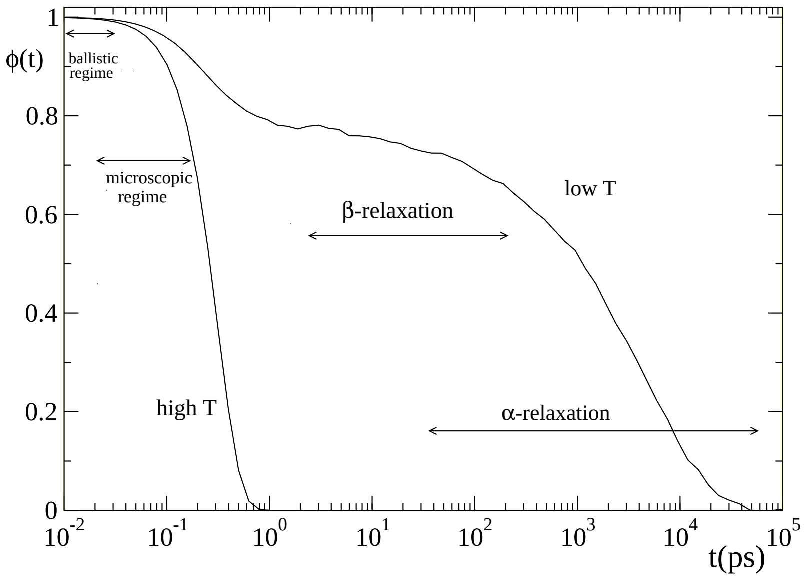

Figure 2: Time dependence of a typical correlation function $\phi(t)$. The two curves correspond to a high temperature, corresponding to typical simple liquid relaxation dynamics, and to a lower temperature in which the relaxation dynamics is the one of a supercooled liquid.

relaxation times with a power law power behaviour : $\eta \sim \tau_\alpha \sim (T - T_c)^{-\gamma}$. However the critical temperature lies above the glass transition temperature T_g determined by thermodynamic experiments such as scanning calorimetry.

Upper panel in Fig 1 shows that the behaviour of $\eta(T)$ (or relaxation time $\tau_\alpha(T)$) cannot be described by the MCT power law $\eta \sim (T - T_c)^{-2.59}$ over the whole temperature range. In particular we note a change of regime at about $T_c \sim 290K$. Within MCT this is interpreted as a cross-over from liquid-like dynamics in *weakly supercooled fluids* ($T_c < T < T_m$), to hopping localized solid-like dynamics in *strongly supercooled fluids* ($T_g < T < T_c$).

Thus at its present state of development, the MCT is inadequate to deal with long time scales beyond ≈ 10 ns (note that the time scale for the laboratory glass transition is 100 seconds!). In the deeply supercooled regime other theoretical frameworks are invoked to account for *partial* dynamic features associated to the glass transition (at present we are far from disposing of a unified theory of the glass transition!). For an overview of the current theoretical approaches to the glass transition problem, see e.g.

the extensive reviews in [9, 10].

Having noted its major drawback, the MCT is a rather exceptional theory. The great success of MCT is to predict an amazingly huge variety (not achieved by any other theory of the glass transition) of highly non-trivial experimental/simulation phenomenologies in glass-formers of very different nature. Some theoretical predictions of MCT confirmed by experiments or simulations include roto-translational decoupling in asymmetric colloids [11], reentrant diffusivities in colloid-polymer mixtures [12] and in concentrate solutions of star polymers [13–15], different types of glasses in mixtures of star polymers [16], and decoupling of self- and collective dynamics in colloidal mixtures [17, 18] and alkali silicates [19].

0.1.2 Dynamics in Polymer Systems

A polymer is a macromolecule constituted of several repetead structural units called monomers, connected through chemical covalent bonds. Monomers are small organic molecules, typically made of hydrogens and carbons. Polymers formed by a single type of monomers are known as homopolymers. An important feature which determines polymer properties is the polymer architecture. The simplest one is the linear chain, in which monomers are connected along a single backbone. Other more complex architectures include for example, branched polymers, star polymers, dendrimers and combs. The polymer architecture is extremely important for the rheological properties, which are related to chain reorientation at large scales. The latter is strongly modified by the presence of branch points [20, 21]. Instead, the polymer architecture has a much weaker influence in the structural relaxation at local scales.

The different dynamic processes present in polymers in amorphous state cover a extremely broad range of characteristic time scales, spanning from about 100 femtoseconds up to years. There are two main reasons for this. First, polymers are usually good glass-formers, which inherently exhibit the universal features (see above) characterizing these materials: a dramatic increase of the viscosity and structural (α-)relaxation times on approaching the glass transition temperature $T_{\rm g}$. As in non-polymeric glass-formers, localized dynamic processes are also present below $T_{\rm g}$ [22]. Second, their macromolecular character introduces relaxation processes related to the dynamics of the internal chain degrees of freedom. In the case of low-molecular weight, nonentangled, polymer chains a sublinear increase (Rouse-like) arises in the mean squared displacement prior to the linear diffusive regime (see discussion in chapter 2). In the case of high-molecular weight, strongly entangled, chains further sublinear regimes are found between the Rouse and linear regimes, which are usually interpreted in terms of reptation dynamics [21, 27, 28]. Such processes are inherent to chain connectivity, and extend over more time decades on increasing chain length. This broad time window for chain dynamics is observed even for temperatures far above T_{g}, when the structural relaxation extends over just a few picoseconds.

Another particular ingredient of polymers is the presence of intramolecular barriers. They are in fact responsible of partial or total crystallization [23, 24], and can enhance reptation effects (which control the rheological properties of the system). The dynamical properties of fully flexible linear polymers in solution or in melt have been worked out in the fundamental works of Rouse [25] and Zimm [26] for nonentangled polymers, as well as of Doi and Edwards [27] and de Gennes [28] for entangled polymers. In contrast to fully flexible polymers, semiflexible polymer models have received only recently substantial attention. Such models are of great interest, since they can be applied to many important biopolymers such as proteins, DNA, rodlike viruses, or actin filaments [29–31]. Moreover, the chain stiffness seems to play an important role in the adsorption behaviour of polymers onto surfaces [32, 33] and viscoelastic properties [34]. Thus, an understandig of the role of the intramolecular barriers on structural and dynamic properties of polymer systems is of practical as well as of fundamental interest in many fields of research.

0.2 Motivations of this work

0.2.1 MCT in Polymer Melts

A possible theroretical approach to the former problem is provided by the Mode Coupling Theory (MCT) [6]. In the first part of this memory we investigate the role of intramolecular barriers on the glass transition and chain dynamics in homopolymer melts. We perform molecular dynamics simulations of a single bead-spring model for homopolymers with intramolecular barriers of tunable strength. We analyze simulation data in the framework of the Mode Coupling Theory and compare results of the simulation data analysis with the numerical solution of the MCT equations. MCT introduces a closed set of coupled Mori-Zwanzig equations (see chapter 3) for the time dependence of density correlators. Static correlations enter the memory kernel as external input. Since the former can be related to the interaction potential through liquid state theories, MCT constitutes a first-principle theory for slow dynamics in complex systems. MCT has been developed over the last years to include systems with intramolecular structure (see e.g., [35–37]). This includes the approach of Chong and co-workers for simple polymer melts [38, 39], based on the polymer reference interaction site model (PRISM) [40] for the static correlations. This approach was applied by Chong *et al.* to the specific case of fully-flexible chains [38,39], i.e., without intramolecular barriers. A major success was the derivation, from first-principles, of the scaling laws predicted by the phenomenological Rouse model [25,27] for chain dynamics in nonentangled polymer melts. Likewise, it provided a unified microscopic description of both chain dynamics and the structural relaxation associated to the glass transition [38, 39].

In this thesis work we investigate, by means of molecular dynamics simulations, the decisive role of intramolecular barriers on the glass transition of polymer melts, by systematically tuning the barrier strength in a simple bead-spring model. We discuss the obtained results within the framework of the Mode Coupling Theory. MCT asymptotic laws have been already tested in different polymeric systems. The values of the associated dynamic exponents exhibit significant differences between the limits of fully-flexible bead-spring chains [41] and fully-atomistic polymers [42–44]. In particular, the so-called exponent parameter takes standard values $\lambda \sim 0.7$ for the former case and values approaching the upper limit $\lambda = 1$ for chemically realistic polymers [42–44]. While the former λ-values are characteristic of systems dominated by packing effects, as the archetype hard-sphere fluid, the limit $\lambda = 1$ arises at higher-order MCT transitions [45]. The latter, or more generally transitions with λ close to 1, arise in systems with different competing mechanisms for dynamic arrest. These systems include short-ranged attractive colloids [46–48] (competition between short-range attraction and hard-sphere repulsion) or binary mixtures with strong dynamic asymmetry [17, 18, 49, 50] (bulk-like caging and confinement).

Motivated by these analogies, we argue that values of $\lambda \to 1^-$ for real polymers also arise from the competition between two distinct mechanisms for dynamic arrest: usual packing effects and polymer-specific intramolecular barriers. Such barriers are not present in fully-flexible bead-spring chains, which exhibit standard λ-values [41]. In order to shed light on this question, we perform a systematic investigation of the interplay between packing and intramolecular barriers. Starting from fully-flexible bead-spring chains, stiffness is introduced by implementing intramolecular bending and torsion terms. The barrier strength is systematically tuned in order to induce competition between the former two mechanisms. Values of λ and critical temperature T_c are obtained by means of a consistent fitting procedure of the MCT asymptotic laws to simulation data. In order to test the quality and limitation of the MCT theory we compare simulation results with numerical solutions of the long-time limit of MCT equations. We also solve the time-dependent MCT equations for density correlators, and compare simulation and theoretical trends in α-relaxation times. We find that there is a progressive discrepancy between simulation results and MCT numerical solutions as the limit of stiff chains is approached. We critically discuss the limitations of the theory by analyzing the accuracy of the several approximations assumed in the derivation of the theory.

We also present here a systematic investigation on the effect of intramolecular barriers on the internal chain dynamics of nonentangled polymers. We analyze correlators for the chain normal modes (Rouse modes) and for bond reorientation. It is well-known that the presence of strong intramolecular barriers violates the Rouse assumption of gaussian behaviour for the static intrachain correlations. Indeed, simulations reveal strong deviations from the Rouse model on increasing chain stiffness, as also observed in [51–55]. Thus, the chains studied in this work are semiflexible in the meaning that they can be deformed but, unlike fully-flexible chains, the static intramolecular correlations are strongly non-gaussian within all the chain length scale.

In the same spirit as the Rouse model for fully-flexible chains, phenomenological models for semiflexible polymers usually model the interactions of the tagged chain with the surroundings by means of a friction term and random forces [56,57]. As in the Rouse model for gaussian chains, the dynamics of the tagged chain is encoded in the assumed form of the intramolecular interactions (e.g., worm-like chains). Memory effects induced by slow density fluctuations of the surrounding matrix are neglected, and non-Rouse effects are of intramolecular origin. The latter is entirely related to static contributions and the amplitudes and relaxation times of the Rouse modes follow the same scaling behaviour [55]. We compare the non-trivial dynamic features observed in simulations with the solutions of the time dependent MCT equations for Rouse correlators. We show that MCT qualitatively reproduces the trends observed in simulations for Rouse mode correlators and Rouse relaxation times. The latter can be easily approximated by the scaling laws proposed in [55]. This generalizes the analysis by Chong *et al.* of

Ref. [39], which was limited to fully-flexible chains, to polymers with intramolecular barriers of arbitrary strength.

0.2.2 Chain Dynamics in Polymer Blends

In the second part of the memory (chapter 7) we investigate, by means of simulations, the effect of blending with a slower matrix on the dynamic scenario observed for the semiflexible homopolymer, aiming to discriminate static and dynamic contributions to anomalous chain dynamics in the blend.

It is well known that miscible polymer blends exhibit dynamic disparity. By starting from two homopolymers with different mobilities, two separated structural relaxations are still found in the blend state [58, 59]. When the two homopolymers exhibit very different glass transition temperatures, and the concentration of the fast component is low, the respective time scales in the blend can differ by orders of magnitude, leading to strong dynamic asymmetry [60]. This effect is enhanced on decreasing the temperature, and can be of even 12 decades for high dilution of poly(ethylene oxide) (PEO) in poly(methyl methacrylate) (PMMA) [61]. In conditions of strong dynamic asymmetry, the motion of the fast component is confined by the slowly relaxing matrix formed by the slow component. Unusual dynamic features arise for the fast component in this case. Neutron scattering experiments in the blend PEO/PMMA reveal decoupling between self-motions and intrachain collective relaxation for the PEO [62]. Atomistic simulations of the former system reveal logarithmic decays of the scattering functions probing the segmental relaxation of the PEO [63]. Moreover, the Rouse modes of the PEO chains exhibit anomalous behaviour [64]. All these observations have also been found in simulations of a simple blend of bead-spring chains with strong dynamic asymmetry [65–67], suggesting that they are generic features of real blends.

The simple bead-spring chains of the blends investigated in Refs. [65–67] are fully-flexible. No intramolecular barriers are implemented. The chain length, N, in all the investigated cases is smaller than the entanglement value. In such conditions, the simulations for the homopolymer system are consistent with expectations from the Rouse model [27,68–71]. This is also the case for the slow component in the blend state [67]. However a rather different scenario is found for the fast component in the blend [67], which only shows Rouse dynamics for vanishing dynamic asymmetry. Increasing the latter (by decreasing temperature) induces a progressive deviation from Rouse-like behaviour for *dynamic* observables of the fast component. These include intrinsic non-exponentiality of the Rouse modes and anomalous scaling of the corresponding relaxation times, $\tau_p \sim p^{-x}$, where p is the mode index. On increasing the dynamic asymmetry the exponent increases from the Rouse prediction, $x = 2$, to values $x \lesssim 3.5$. The origin of these features is dynamic. Indeed the static amplitudes of the Rouse modes are not affected by blending, and show gaussian, Rouse-like, scaling as in the homopolymer state [67].

The mentioned dynamic crossover, on increasing the dynamic asymmetry, from $\tau_p \sim p^{-2}$ to $\tau_p \sim p^{-3.5}$ in the *non-entangled* fast component is strikingly similar to that observed for entangled homopolymers on increasing the mode wavelength, N/p, beyond the entanglement length [70, 72, 73]. The crossover for the fast component in the blend is observed even in the limit of short chains. Thus, it was concluded that this feature is entirely controlled by the dynamic asymmetry in the blend, and not by a characteristic entanglement length scale [67]. Related observations have been presented by simulations of short fully-flexible chains in matrixes of fixed obstacles [74–77]. Rouse modes were not analyzed but a crossover, similar to the observation in homopolymers on increasing N, was found. Thus, the diffusivities changed from $D \sim N^{-1}$ to $D \sim N^{-2}$ on increasing the concentration of obstacles. Concomitantly, the end-to-end relaxation time changed from $\tau_\mathrm{e} \sim N^2$ to $\tau_\mathrm{e} \sim N^3$. Again, these observations are not related to particular static intramolecular features or to characteristic entanglement length scales, but being entirely controlled by the concentration of obstacles [76, 77].

In summary, the former results of Refs. [67, 74–77] reveal a crossover to entangled-like dynamic features in non-entangled chains. This crossover is not connected to particular static features of the intrachain correlations. It has a entirely dynamic origin, related to the strength of the confinement effects induced by the surrounding matrix. Theories based on generalized Langevin equations (GLE) introduce a memory kernel accounting for the slow relaxation of density fluctuations around the tagged chain [78]. The Rouse model, which neglects memory effects, arises from such theories in the limit of fast relaxation of the kernel [78, 79]. Memory effects are enhanced on increasing the chain length beyond the entanglement value, and the theory reproduces non-exponentiality and anomalous scaling of the Rouse modes in entangled homopolymers [79]. It has been suggested that GLE methods may also account for the analogous dynamic features exhibited by the non-entangled fast component in polymer blends [67], through the incorporation in the kernel of the memory effects induced by the matrix, formed by the slow component in the blend or by the fixed obstacles in the systems of Refs. [74–77].

As mentioned above, the simulations of Refs. [67, 74–77] were performed for fully-flexible chains. In this memory we briefly review the results of [67] and present new results for blends where the fast component is semiflexible, i.e., it has intramolecular barriers. These are introduced by implementing bending and torsion potentials by means of the same interaction model employed in the homopolymer case. We find that results for the semiflexible component in the blend can be analyzed in terms of the scaling laws proposed in the Markovian model of [55] for the semiflexible homopolymer. This suggests that, unlike for fully flexible chains, memory effects are not relevant for semiflexible chains in the blend in comparison with the role of the intramolecular barriers. Presumably, memory effects will only be relevant, for sufficiently long chains, at large length scales for which the semiflexible character is lost and Gaussian statistics is recovered.

Chapter 1

Homopolymers: Model and Simulation Details

Computer simulations constitute an excellent tool for the investigation of the properties of complex systems [80, 81]. Given a model for the interactions in the system we are interested in, simulations provide a bridge between the model and theoretical predictions on the one hand, and between models and experimental results on the other hand. By integrating the equations of motion of the system, molecular dynamics (MD) simulations provide, within statistical averages, exact results for the interaction model that can be used to test the quality of the predictions of an approximate theory applied to the same model. If theory and simulations disagree, theory must be improved. On the other hand, we can compare the results of the simulations of a model system with experiments. If simulations and experiments disagree, it means that the model for the interactions needs to be improved.

We can distinguish between three different levels to model polymer systems (Fig. 1.1). The first one is the quantum level. We can choose for example to model polymers At a quantum level we can choose for example to model polymers via the Car-Parrinello method [82,83]. This method is an *ab initio* molecular dynamics technique which combines a molecular dynamics scheme with a first principle electronic structure method, which generates the interactions 'on the fly' within the framework of the density functional theory (DFT). The system is placed in a periodically replicated supercell and the valence orbital are expanded into a basis set of plane waves. The effect of the ionic core is described *via ab initio* pseudo-potentials. Such a method is computationally too demanding to study dynamic properties of polymer melts. The inclusion of the

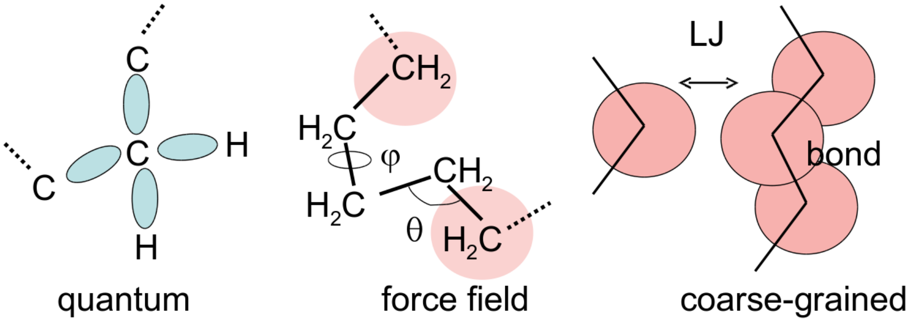

Figure 1.1: Schematic representation of different levels one may utilize to model polymers.

electrons in the simulations restrict the system size to about 100 nuclei and requires a time step of $10^{-17}s$. Thus, as typically 10^8 time steps are performed in a simulation run, a typical Car-Parrinello simulation can simulate a melt of 10 chains of $N = 10$ monomers for about 1 ns [41]. This time is far below typical time scales of relevant processes in polymer systems, as the $\alpha-$time scale in weakly supercooled regime, or time scales probing chain dynamics which typically lie in the range between $1\mu s$ and $1s$ [27, 84]. Simplifications can be introduced by means of a systematic coarse-graining procedure [85–87]. At the atomistic level electronic degrees of freedom are averaged out by means of a force field. The classical force field represents the potential energy of an ensemble of N atoms as a sum of non-bonded interactions and contributions due to all bonds, valence bend and dihedral interactions. The functional form of these force fields is postulated and their parameters are determined from ab-initio quantum-chemistry calculations or from experiments. By standard parallel simulation (with ~ 16 processors) this coarse-graining procedure allows to simulate $\sim 10^4$ atoms over a time range of several 100 ns. Several atomistic force fields have been carefully designed to provide quantitative comparison with experiments of static and dynamic properties of real polymers. The following expression represents the funtional form of the $COMPASS$ [88, 89] (Condensed-phase Optimized Molecular Potential for Atomistic

Simulation Studies):

$$\begin{aligned}
V \;=\;& \sum_b [K_2(b-b_0)^2 + K_3(b-b_0)^3 + K_4(b-b_0)^4] + \\
&+\sum_\theta [H_2(\theta-\theta_0)^2 + H_3(\theta-\theta_0)^3 + H_4(\theta-\theta_0)^4] + \\
&+\sum_\phi \Big[V_1\,[1-\,\cos(\phi-\,\phi_1^0)] + V_2\,[1-\,\cos(2\phi-\,\phi_2^0)] + V_3\,[1-\,\cos(3\phi-\,\phi_3^0)] \Big] + \\
&+\sum_\chi k_\chi \chi^2 + \sum_b \sum_{b'} F_{bb'}(b-b_0)(b'-b'_0) + \sum_\theta \sum_{\theta'} F_{\theta\theta'}(\theta-\theta_0)(\theta'-\theta'_0) + \\
&+\sum_b \sum_\theta F_{b\theta}(b-b_0)(\theta-\theta_0) + \sum_b \sum_\phi (b-b_0)[V_1\cos\phi + V_2\cos 2\phi + V_3\cos 3\phi] + \\
&+\sum_{b'} \sum_\phi (b'-b'_0)[V_1\cos\phi + V_2\cos 2\phi + V_3\cos 3\phi] + \\
&+\sum_\theta \sum_\phi (\theta-\,\theta_0)[V_1\cos\phi + V_2\cos 2\phi + V_3\cos 3\phi] + \\
&+\sum_\theta \sum_{\theta'} \sum_\phi K_{\theta\theta'\phi}(\theta-\theta_0)(\theta'-\theta'_0)\cos\phi + \sum_{i>j} \frac{q_i q_j}{\varepsilon r_{ij}} + \sum_{i>j} \left[\frac{A_{ij}}{r_{ij}^9} - \frac{B_{ij}}{r_{ij}^6} \right]
\end{aligned} \qquad (1.1)$$

Two main classes of terms can be distinguished: the valence terms and the nonbond interaction terms. The valence terms, including diagonal and off-diagonal cross-coupling terms, represent internal coordinates of bond b, bend angle θ, torsion angle ϕ and out-of-plane angle χ. The nonbond interactions include a Lennard-Jonnes 9-6 function for the van der Waals term and a Coulombian function for the electrostatic interaction. The nonbond terms operate for atoms separated by two or more intervening atoms or for those belonging to different molecules.

However, in simulations of hydrocarbon chains, further approximations can be introduced in the force field. Coulomb interactions can be neglected and we can avoid to treat the hydrogen atoms explicitly, but combine them with the carbon atoms to which they are bonded into spherical sites, the so-called united atoms (UAs) [85], and constrain the carbon-carbon bonds to their mechanical equilibrium values. This approximation reduces the number of non-bonded interaction sites leading to the computational advantage of allowing longer simulation times. It also removes the highest frequency oscillations, i.e. the $C-H$ bond length and $H-C-H$ and $H-C-C$ bond angles, from the model. However this approximation is only feasible if we want to study static and dynamic properties of polymers without any specific local interaction, like strong electrostatic interactions or hydrogen bonding. The functional form of UAs force fields reads as:

$$V_{UA} = \sum_i V(b_i) + \sum_j V(\theta_j) + \sum_k V(\Phi_k) + \sum_{n,m} V_{nb}(r_{nm}) \tag{1.2}$$

where the sum extends over all bonds, bends, torsions and interacting atoms, respectively. Both atomistic and united-atoms force fields have been utilized in the study of glass-forming polymers, in order to provide a quantitative comparison between experiment and simulations, and additional information about static and dynamic properties which are not directly accesible from experiments. Examples include polyisoprene (atomistic [90, 91]), atactic polystyrene (united-atom [92, 93]), *cis-trans*-1,4–polybutadiene (atomistic and united-atoms [42, 43, 52, 85]) and polyethylene (atomistic and united-atoms [94–97]).

However there are properties which are generally observed for several classes of polymers, irrespective of the chemical structure. Concerning the glass transition, the strong slowing down of the dynamics on lowering temperature or increasing density, leading to a final dynamic arrest in an amorphous glassy state, is observed for polymer melts, independently on the chemical details. Analogously, if we are interested in the *qualitative* dynamic properties at length scales somewhat larger than the size of the monomer (of the order of ~ 1 nanometer), the detailed chemical structure of the building blocks is not important. These universal properties for example include subdiffusive regimes in the mean square displacements, which are a direct consequence of the presence of chain connectivity, and scaling behaviour of Rouse amplitudes and relaxation times (see next chapter).

Thus, if one is interested on predicting such general behaviours, it is useful to further coarse-grain the atomistic, or UAs, force-field. A new coarse-grained model can be obtained by retaining only the most basic features of polymers chains which include: chain connectivity, excluded volume interactions, possibly monomer-monomer attraction and stiffness along the chain backbone. A representative example of these coarse-grained models is the bead-spring model. Introduced by Kremer and Grest [68, 99], it is widely used by the computational community of polymer physics in many differents topics of research, predicting static and dynamic features of flexible polymer melts, from the caging regime to large scale dynamics. In this model the position of a monomer or bead, which comprises several real monomers, is described by their position vector $\mathbf{r}_j$. Chain connectivity is introduced by means of non-linear springs connecting consecutive beads along the chain backbone. Monomers belonging to the same chain or to differet chains interact through a simple potential, like shifted Lennard-Jones or soft sphere repulsive potentials (see next section for further details).

The bead-spring model is the starting point of our simulation work. We carried out MD simulations on bead-spring chains in melt conditions. Following Bulacu and Van der Giessen [53, 98], we extended the bead-spring model by introducing a bending and torsion potential, in order to study the role of intramolecular barriers on several dynamic aspects of nonentagled polymer melts. The investigated range extends from the caging regime characteristic of glass-formers to the relaxation of the chain Rouse modes.

1.1 Basic Notations

In the following $\mathbf{r}_j^a(\mathrm{t})$ is the position of the ath monomer placed in the jth chain at time t, with $a = 1, ..., N$ and $j = 1, ..., n$. The total number of monomers in the cubic box of volume V, is $M = nN$ with N the number of monomers per chain and n the number of chains. The chain and monomer densities are respectively defined as:

$$\rho_c \equiv \frac{n}{V} \qquad \text{and} \qquad \rho \equiv \frac{M}{V} \tag{1.3}$$

The position of the center of mass of the jth chain at time t is defined as:

$$\mathbf{R}_j(t) \equiv \frac{1}{N}\sum_{a=1}^{N} \mathbf{r}_j^a(t) \tag{1.4}$$

The squared radius of gyration and squared end-to-end radius reads like:

$$\langle R_g^2 \rangle \equiv \frac{1}{M}\langle \sum_{j=1}^{n}\sum_{a=1}^{N} (\mathbf{r}_j^a - \mathbf{R}_j)^2 \rangle \qquad \text{and} \qquad \langle R_{ee}^2 \rangle \equiv \frac{1}{n}\langle \sum_{j=1}^{n} (\mathbf{r}_j^1 - \mathbf{r}_j^N)^2 \rangle \tag{1.5}$$

The explicit time dependence will be dropped for static quantities. Here and in the following $\langle \cdot \rangle$ denotes ensemble average for temperature T.

1.2 Model and Simulation Details

We have performed molecular dynamics (MD) simulations on a bead-spring model very similar to the one originally introduced by Grest and Kremer for homopolymers [68,99], with the addition of bending and torsional intramolecular barriers.
The interaction between two monomers α and β, placed on different chains or in the same one, is given by a corrected soft-sphere potential

$$V_{\alpha\beta}(r) = 4\epsilon[(\sigma_{\alpha\beta}/r)^{12} - C_0 + C_2(r/\sigma_{\alpha\beta})^2], \tag{1.6}$$

where $\epsilon = 1$ and $\sigma_{\alpha\beta} = 1$ for each (α, β). The potential $V_{\alpha\beta}(r)$ is set to zero for $r \geq c\sigma$, with $c = 1.15$.

The values $C_0 = 7c^{-12}$ and $C_2 = 6c^{-14}$ guarantee continuity of potential and forces at the cutoff distance $r = c\sigma$. The potential $V(r)$ is purely repulsive, it does not show any local minima within the interaction range $r < c\sigma$. Thus, it drives dynamic arrest only through packing effects.
Along the polymer backbone an additional FENE [68, 99–101] (finitely extensible non-linear elastic) potential was used to introduce bonds between consecutive monomers:

$$V_{\alpha\alpha}^{\mathrm{FENE}}(r) = -\epsilon K_{\mathrm{F}} R_0^2 \ln[1 - (R_0\sigma_{\alpha\alpha})^{-2} r^2], \tag{1.7}$$

where $K_F = 15$ and $R_0 = 1.5$. The superposition of potentials (1.6) and (1.7) provides an effective bond potential for consecutive monomers with a sharp minimum at $r \approx 0.985\sigma_{\alpha\alpha}$, which makes bond crossing impossible (see fig. 1.2).

Intramolecular barriers have been implemented by means of a combined bending, V_B, and torsional potential V_T. We used the potentials proposed in [53, 98]. The bending potential acts on three consecutive monomers along the chain. The angle between adjacent pairs of bonds is mantained close to the equilibrium value $\theta_0 = 109.5^{\mathrm{o}}$ by the cosine harmonic bending potential

$$V_{\mathrm{B}}(\theta_i) = (\epsilon K_{\mathrm{B}}/2)(\cos\theta_i - \cos\theta_0)^2, \tag{1.8}$$

where θ_i is the bending angle between consecutive monomers $i-1$, i and $i+1$ (with $2 \leq i \leq N-1$).

The torsional potential constrains the dihedral angle $\phi_{i,i+1}$, which is defined for the consecutive monomers $i-1$, i, $i+1$ and $i+2$ (with $2 \leq i \leq N-2$), as the angle

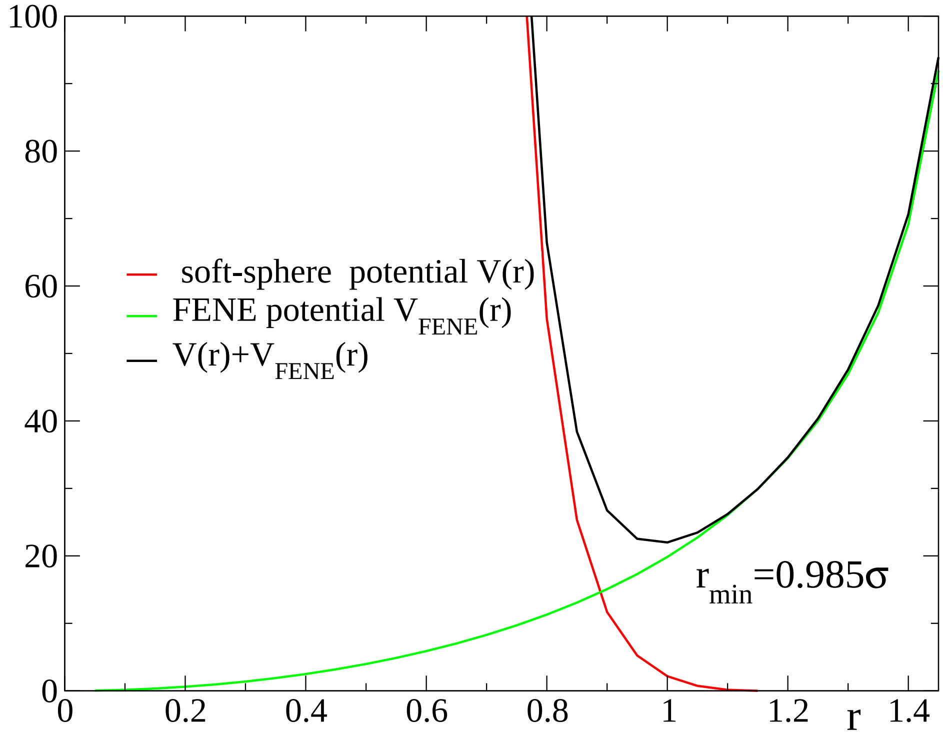

Figure 1.2: Representation of the corrected soft-sphere potential $V(r)$ and the FENE potential V_{FENE} as a function of the monomer-monomer distance. The superposition $V(r) + V_{FENE}(r)$ provides an effective bond potential for consecutive monomers with a sharp minimum at $r \approx 0.985\sigma_{\alpha\alpha}$, which makes bond crossing impossible.

between the two planes defined by the sets $(i-1,\ i,\ i+1)$ and $(i,\ i+1,\ i+2)$. The form of this potential is

$$V_{\mathrm{T}}(\theta_i, \theta_{i+1}, \phi_{i,i+1}) = \epsilon K_{\mathrm{T}} \sin^3\theta_i \sin^3\theta_{i+1} \sum_{n=0}^{3} a_n \cos^n \phi_{i,i+1}. \tag{1.9}$$

The third-order polynomial in $\cos\phi_{i,i+1}$ follows from *ab-initio* calculations for $n-$butane and has the coefficients $a_0 = 3.00$, $a_1 = -5.90$, $a_2 = 2.06$, $a_3 = 10.95$ [53,98]. Note that the potential in eq. 1.9 depends both on the dihedral angle $\phi_{i,i+1}$ and on the bending angles θ_i and θ_{i+1}. In this way the numerical instabilities arising when two consecutive bonds align are naturally eliminated without the need of imposing rigid constraints on the bending angles.

In the following, temperature T, time t, and length are given respectively in units of ϵ/k_{B} (with k_{B} the Boltzmann constant), $\sigma(m/\epsilon)^{1/2}$, and σ. Simulation units can be qualitatively mapped to real units as $\sigma \sim$ 5-10 Å, $\sigma(m/\epsilon)^{1/2} \sim$ 1-10 ps, and $\epsilon/k_{\mathrm{B}} \sim$ 300-500 K (see the discussion in, e.g., Refs. [41, 68]).

Simulations for this simple model of intramolecular barriers reproduce qualitative features observed in real polymers. For example in [53, 98] the authors rationalize non-trivial trends exhibited by the exponents z for the N-dependence of the diffusivity, $D \sim N^{-z}$, below and above the entanglement length. Thus, they find:

i) Power-law scaling of the diffusivity, with two regimes $D \sim N^{-x_1}$, $D \sim N^{-x_2}$ for respectively small and large N. Both x_1 and x_2 grow on increasing chain stiffness. This effect is stronger for x_1 and both exponents tend to approach a common value $x \sim 2$, for realistic values of C_∞. As discussed in [53], this is apparently consistent with the experimental observation of an almost N-independent exponent (also there $x \sim 2$).

ii) The former exponent grows on decreasing temperature towards the glass transition. As discussed in [98], this observation is again apparently consistent with experiments. Actually, united-atoms models (eq. 1.2) consist typically of Lennard-Jones non-bonded interactions, bonding potentials, and intramolecular barriers are reduced to simple bending and torsion terms. Though not aiming to describe properties of any specific polymer, the model used here is sufficiently realistic to describe qualitatively properties of a broad family of polymer systems.

We investigate at fixed monomer density $\rho = 1$, which corresponds to melt conditions in bead-spring models [41, 102], the temperature dependence of the dynamics for different values of the bending and torsion strength, (K_{B},K_{T}) = (0,0), (4,0.1), (8,0.2),(15,0.5), (25,1), (25,4), and (35,4). We investigate typically 8-10 different temperatures for each set of values (K_{B},K_{T}). The investigated range of barrier strength corresponds to a strong variation of the chain stiffness. This can be quantified by the characteristic ratio $C_\infty^{\mathrm{r}} \equiv \lim_{N\to\infty} C_N^{\mathrm{r}}$, where $C_N^{\mathrm{r}} = \langle R_{\mathrm{ee}}^2 \rangle / (N \langle b^2 \rangle)$. Here R_{ee} and b denote respectively the chain end-to-end radius and the bond length. Brackets denote ensemble average. We simulated only short chains with $N = 10$ monomers, so we can only provide the values of C_{10}^{r}. Fig. 1.3 displays the obtained values of C_{10}^{r} at all the investigated state points ($K_{\mathrm{B}}, K_{\mathrm{T}}, T$). As expected, chain stiffness is enhanced by increasing the strength of the barriers and by decreasing temperature. Moreover, the effect of temperature is much more pronounced in chains with strong barriers than in fully-flexible chains, for which C_{10}^{r} is nearly T-independent. The investigated state points cover a broad range of stiffness, with values of C_{10}^{r} varying from $C_{10}^{\mathrm{r}} \approx 1.3$ for fully-flexible chains up to $C_{10}^{\mathrm{r}} = 4.3$ for the strongest barriers, $(K_{\mathrm{B}}, K_{\mathrm{T}}) = (35, 4)$, at the lowest investigated T. However the data of C_{10}^{r} given here are considerably smaller than the limit C_{∞}^{r} estimated from simulations or experiments on much longer chains. This is clearly a finite size effect. Thus, at $T = 1.0$ we find $C_{10}^{\mathrm{r}} = 3.0$ for $(K_{\mathrm{B}}, K_{\mathrm{T}}) = (25, 1)$. Data in Ref. [53] for the same model of intramolecular barriers and much longer chains $(N = 200)$ provide an estimation of C_{∞}^{r}, with a value almost twice larger, $C_{200}^{\mathrm{r}} = 5.8$, than C_{10}^{r} for the former $(K_{\mathrm{B}}, K_{\mathrm{T}}, T)$. The value $C_{\infty}^{\mathrm{r}} \gtrsim C_{200}^{\mathrm{r}} = 5.8$ is comparable to characteristic ratios of, e.g., polybutadiene and polypropylene [103]. The stiffest case investigated here (not studied in [53]), will presumably yield values $C_{\infty}^{\mathrm{r}} \sim 10$, similar to that of polystyrene [103].

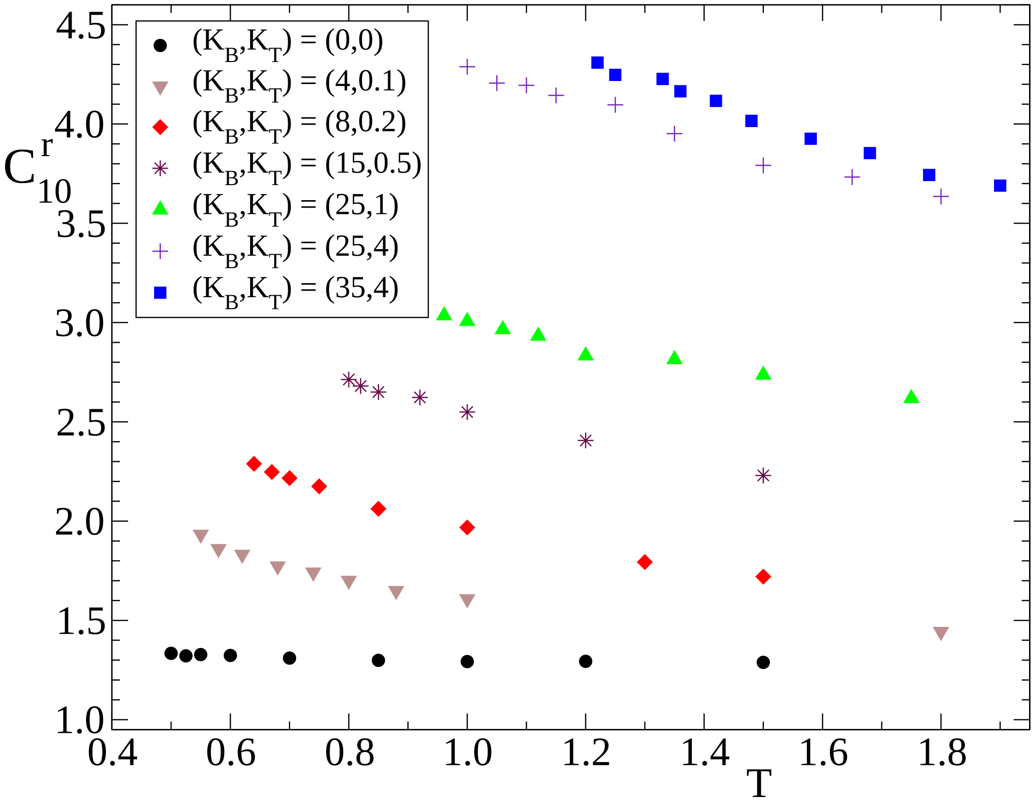

Figure 1.3: Temperature dependence of the characteristic ratio C_{10}^{r} for all the investigated state points.

We simulate $n = 300$ chains, each chain consisting of $N = 10$ monomers of mass $m = 1$, placed in a cubic simulation box with periodic boundary conditions. The choice of the chain length $N = 10$ is not unjustified. On the one hand a smaller value of N would not allow to observe polymer specific effects, e.g. Rouse dynamics(see next chapter). On the other hand much larger values of N would be computationally too demanding in order to study chain relaxation processes on decreasing temperature. Because we are interested in comparing simulation results with the predictions of the MCT theory for nonentangled polymers, the chain length N should be shorter than the entanglement length of our model, which is approximately $N_e \sim 35$ [68, 104].

Equations of motion are integrated by using the velocity Verlet scheme [80]:

$$\mathbf{r_i}(t+h) = \mathbf{r_i}(t) + h\mathbf{v_i}(t) + \frac{h^2}{2}\mathbf{F_i}(t) \tag{1.10}$$

$$\mathbf{v_i}(t+h) = \mathbf{v_i}(t) + \frac{h}{2}[\mathbf{F_i}(t) + \mathbf{F_i}(t+h)] \tag{1.11}$$

Here $\mathbf{r_i}(t)$ and $\mathbf{v_i}(t)$ are the position and the velocity of the particle i at time t, $\mathbf{F_i}$ is the force acting on this particle, and h is the time step. The error in the predicted coordinates is of the order of $O(h^4)$ and in the velocities of $O(h^2)$ [80].

We use a time step ranging from 10^{-4} to 5×10^{-3}. We take larger and shorter steps for respectively low and high values of temperatures, bending and torsional constants. A linked-cell method [80] is used for saving computational time in the determination of the particles within the interaction range of a given one. The basic idea of the method is the following: the simulation box is divided into cells with a size equal or slightly larger than the cutoff radius r_c (equal to $c\sigma$ in our model). Thus each particle in a given cell can only interact with the particles in the same or in neighbouring cells. Hence, we only need to calculate such distances for computing forces. Since the allocation of a particle to a cell is an operation that scales with N (number of particles), the linked-cell method scales with N. On the other hand, computing all the distances between all the particles is an operation that scales like N^2, which would require much more computational time.

The system is prepared by placing and growing the chains randomly in the simulation box, with a constraint for the interparticle distance $r \geq 0.75\sigma_{\alpha\beta}$ avoiding monomer core overlap. The initial monomer density is $\rho = 0.375$. Equilibration consists of a first run where the box is rescaled periodically by a factor $0.99 < f < 1$ until the target density ρ is reached, and a second isochoric run at that ρ. Thermalization at the target T is achieved by periodic velocity rescaling with a period $\tau \leq 0.25$ in simulation units. After reaching equilibrium, energy, pressure, chain radii of gyration, and end-to-end distances show no drift. Likewise, dynamic correlators and mean squared displacements show no aging, i.e., no time shift when being evaluated for progressively longer time origins. Once the system is equilibrated, a microcanonical run (at constant energy) is performed for production of configurations, from which static structure factors, dynamic correlators and mean squared displacements are computed. For each state point, the latter two quantitites are averaged over typically 40 equispaced time origins. The typical duration of a production run is of 40-300 million time steps for respectively high and low temperatures. The estimated sum of the CPU time, of all the simulation runs performed in this work, is about 4 years.

Even if a small time step is used, deviations from the true dynamics are unavoidable and an overall, upward drift in energy develops. In order to maintain the total energy approximately constant we periodically compute the quantity $\delta E = E(t) - E_0$, where $E_0 = E(t = 0)$ is the total energy evaluated at the starting point of the microcanonical run. When $|\delta E/E_0| > 10^{-3}$ a rescaling of velocities, irrelevant within fluctuations of temperature, is performed to correct the kinetic energy and recover the initial total energy E_0. This procedure avoids a long time drift in the total energy E. This rescaling was performed, as much, only a few times during the total simulation time (less than 20 times in typically 10^8 time steps), which does not affect statistical averages of static and dynamic observables.

Before addressing the static and dynamic aspects of the present system, we want to stress that the investigated state points correspond to isotropic phases. We do not observe signatures of *global* orientational order induced by chain stiffness for the investigated state points. Thus, by measuring the quantity $P_2(\Theta) = (3\langle\cos^2\Theta\rangle - 1)/2$, where Θ is the angle between the end-to-end vectors of two chains, and averaging it over all pairs of distinct chains, we obtain in all cases values $|P_2(\Theta)| < 3 \times 10^{-3}$. This is illustrated in Fig. 1.4, which shows the time evolution of $P_2(\Theta)$ along a typical simulation window, both for fully-flexible chains, $(K_{\mathrm{B}},K_{\mathrm{T}}) = (0,0)$, and for the stiffest investigated chains, $(K_{\mathrm{B}},K_{\mathrm{T}}) = (35,4)$. Data in both cases correspond to the lowest investigated temperatures.

Local orientational order is also negligible. This is evidenced by computing a similar correlator $P_2(\Theta; r_{\mathrm{cm}})$. In this case the average is performed only over pairs of distinct chains for which the distance between their respective centers-of-mass is less than r_{cm}. Fig. 1.4 displays, for the former cases of fully-flexible and stiff chains, data of $P_2(\Theta; r_{\mathrm{cm}})$ for several values of r_{cm}. Negligible values of $P_2(\Theta; r_{\mathrm{cm}})$ are obtained for

$r_{\rm cm} \geq 2.0$. Thus, the time average over the simulation time window, $t_{\rm sim}$, provides values $|\langle P_2(\Theta; r_{\rm cm} \geq 2.0)\rangle_{\rm t_{sim}}| < 0.02$. By comparing both panels we conclude that chain stiffness does not induce a significant increase, if any, of local orientational order in the investigated systems. Weak local orientational order $|\langle P_2(\Theta; r_{\rm cm})\rangle_{\rm t_{sim}}| \lesssim 0.1$ is observed only for very small interchain distances (see data for $P_2(\Theta; r_{\rm cm} = 1.4)$). Again, the introduction of chain stiffness does not induce clear changes in the orientational order at this length scale.

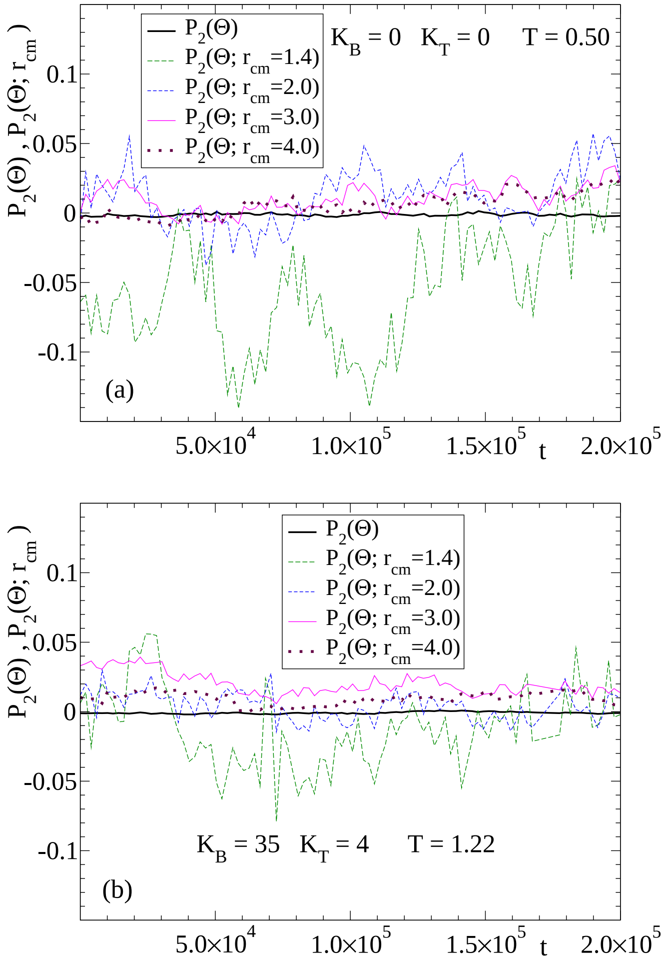

Figure 1.4: Time evolution of the global and local orientational parameter (see text) at two selected temperatures, for fully-flexible chains (a) and stiff chains (b) with $(K_{\rm B}, K_{\rm T}) = (35, 4)$.

Chapter 2

Homopolymers: Static and Dynamic Features

2.1 Density Correlators: Static Properties

In this section we present the static structural and conformational properties of our model. In particular we will discuss the case of fully flexible chains, ($K_{\mathrm{B}} = 0, K_{\mathrm{T}} = 0$) and a representative case of stiff chains ($K_{\mathrm{B}} = 25, K_{\mathrm{T}} = 1$).

We introduce the Fourier-transformed monomer densities at wave vector $\mathbf{q}$

$$\rho_j^a(\mathbf{q},t) \equiv \exp[i\mathbf{q}\cdot\mathbf{r}_j^a(t)] \qquad \text{and} \qquad \rho(\mathbf{q},t) \equiv \sum_{j=1}^{n}\sum_{a=1}^{N}\rho_j^a(\mathbf{q},t) \tag{2.1}$$

The static density-density correlation at the monomer level can be characterized by the monomer-monomer static structure factor

$$S_{ab}(q) = \frac{1}{n}\Big\langle \sum_{i,j=1}^{n} \rho_i^a(-\mathbf{q})\rho_j^b(\mathbf{q})\Big\rangle, \tag{2.2}$$

Since our systems are spatially homogeneous and isotropic, the static structure factors depend only on the modulus of the wave vector $q = |\mathbf{q}|$. The monomer-monomer static structure factor $S_{ab}(q)$ can be splitted into an intrachain and an interchain term, revealing static correlations between monomers belonging to a same chain or to different chains:

$$S_{ab}(q) = \omega_{ab}(q) + \rho_c h_{ab}(q) \tag{2.3}$$

Here $\omega_{ab}(q)$ denotes the intrachain contribution while the interchain contribution is given by $h_{ab}(q)$.

In the following we will discuss the structure factors averaged over all monomer pairs (a, b). So we obtain the collective structure factor in terms of the total monomer density distribution :

$$S(q) = \frac{1}{N} \sum_{a,b=1}^{N} S_{ab}(q) = \frac{1}{nN} \langle \rho(-\mathbf{q}) \rho(\mathbf{q}) \rangle \tag{2.4}$$

The averaged static structure factor $S(q)$ can also be splitted into intrachain and interchain parts

$$S(q) = \omega(q) + \rho h(q) \tag{2.5}$$

with $\omega(q) = N^{-1} \sum_{a,b} w_{ab}(q)$ and $h(q) = N^{-2} \sum_{a,b} h_{ab}(q)$. The intrachain term $\omega(q)$ is also known as the form factor of the chain.

Another important quantity for the description of the static properties of our systems is the site-site direct correlation function defined as the second functional derivative of the free energy of the system [105]. In the Fourier space the site-site direct correlation function $c_{ab}(q)$, is introduced via the generalized Ornstein-Zernike relation for polyatomic molecules, or 'reference interaction site model' (RISM) [106],

$$h_{ab}(q) = \sum_{x,y=1}^{N} \omega_{ax}(q) c_{xy}(q) [\omega_{yb}(q) + \rho_c h_{yb}(q)], \tag{2.6}$$

in which intramolecular contributions are accounted by the form factor terms $\omega_{ab}(q)$. By inserting (2.3) in Eq. (2.6), $c_{ab}(q)$ is related to $S_{ab}(q)$ and $\omega_{ab}(q)$ as:

$$\rho_c c_{ab}(q) = \omega_{ab}^{-1}(q) - S_{ab}^{-1}(q). \tag{2.7}$$

Here $\omega_{ab}^{-1}(q)$ and $S_{ab}^{-1}(q)$ are the elements of, respectively, the matrices $\mathbf{w}^{-1}(q)$ and $\mathbf{S}^{-1}(q)$, which are defined as the inverses of $\mathbf{w}(q)$ and $\mathbf{S}(q)$. For later reference (see chapter 3) we introduce the equivalent-site approximation for $c_{ab}(q)$. In the equivalent-site approximation (which is exact for polymer rings), chain end effects are neglected and all sites are treated equivalently for interchain correlations. Thus, c_{ab} is replaced by the average over all (a,b)-pairs:

$$c_{ab}(q) \approx c(q). \tag{2.8}$$

By introducing this approximation in Eq. (2.6) and averaging over all (a,b)-pairs we find $h(q) = \omega(q)c(q)[\omega(q) + \rho h(q)]$. By introducing Eq. (2.5) in the latter expression we arrive to the scalar equation

$$\rho c(q) = 1/\omega(q) - 1/S(q), \tag{2.9}$$

also known as PRISM equation [40]. The PRISM equation and the equivalent-site approximation are essential ingredients in the development of the Mode Coupling Theory for polymer melts. We will discuss these points in more detail in Chapter 3.

Another approximation (also exact for ring polymers) which is needed in the development of MCT for polymer melts involves the site-ste static structure factor $S_{ab}^{-1}(q)$. First of all we note that in a ring the quantity $\widetilde{S_a}(q) \equiv \Sigma_{b=1}^{N} S_{ab}(q)$ is a-independent, and that the relation $\widetilde{S_a}(q) = (1/N)\Sigma_{a=1}^{N}\widetilde{S_a}(q) = S(q)$ holds. Furthermore from the identity $\Sigma_{x,b} S_{ax}^{-1}(q) S_{xb}(q) = \Sigma_b \delta_{ab} = 1$ we also have $\widetilde{S_a^{-1}}(q) \equiv \Sigma_{b=1}^{N} S_{ab}^{-1}(q) = 1/S(q)$. With these relations in mind, we introduce the following approximations for linear chains:

$$\widetilde{S_a}(q) \equiv \sum_{b=1}^{N} S_{ab}(q) \approx S(q), \tag{2.10}$$

$$\widetilde{S_a}^{-1}(q) \equiv \sum_{b=1}^{N} S_{ab}^{-1}(q) \approx \frac{1}{S(q)}. \tag{2.11}$$

2.1.1 Static Structure Factors

In figures 2.1 and 2.2 we show the simulation results for $S(q)$ as a function of temperature for fully flexible $(K_{\mathrm{B}}, K_{\mathrm{T}}) = (0{,}0)$ and representative stiff chains $(K_{\mathrm{B}}, K_{\mathrm{T}}) = (25{,}1)$ respectively. In both cases, no signature of crystallization is present, in fact no sharp Bragg peaks are observed. Moreover there is no orientational order as noted in the previous chapter. The collective structure of the melt indeed follows the trends of dense disordered systems. In the $q \rightarrow 0$ limit, $S(q)$ takes small values due to low compressibility of the systems. In both cases, the static structure factor shows a maximum at $q^{max} \approx 7.0$. Since $S(q^{max})$ comes from the packing in the first shell around a monomer, the latter corresponds to a typical distance $2\pi/7.0 \approx 0.90$ in the real space between neighbouring monomers. On cooling the peak at $q^{max} \approx 7.0$ increases in intensity, which is a signature of increasing short-range order.

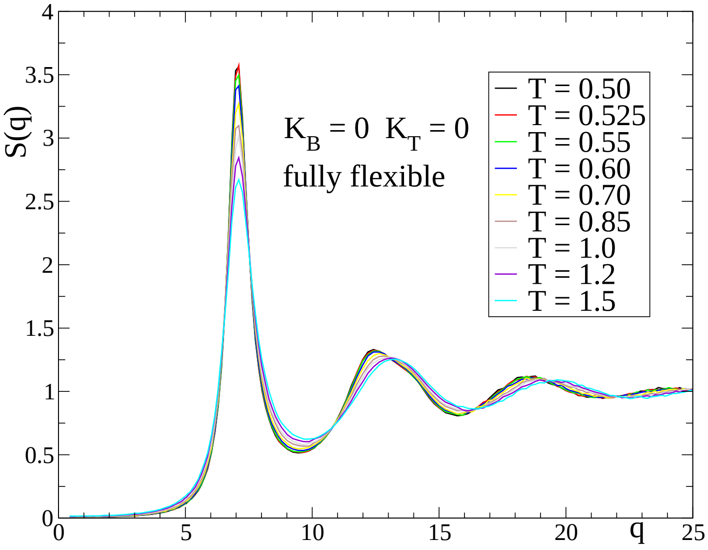

Figure 2.1: Static structure factor $S(q)$ as a function of temperature for the fully flexible chains $(K_{\mathrm{B}},K_{\mathrm{T}}) = (0,0)$.

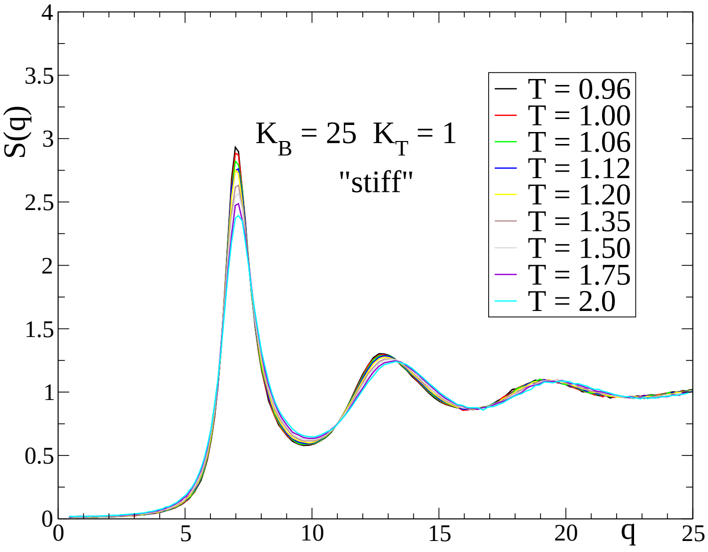

Figure 2.2: Static structure factor $S(q)$ as a function of temperature for the stiff chains $(K_{\mathrm{B}},K_{\mathrm{T}}) = (25,1)$

2.1.2 Form Factors

In figure 2.3 we show the simulation results for the form factors $w(q)$. We note that in the case of fully flexible chains, the form factor is nearly independent on temperature. On the contrary the $w(q)$ for stiff chains shows a weak dependence on temperature, this dependence being more clear at low q values. The way the form factor behaves on lowering the temperature is directly connected with the values of the mean chain end-to-end radius R_{ee}. Thus, by decreasing temperature R_{ee} increases from 4.8 to 5.5 for the stiff chains, leading to a stronger decay in $\omega(q)$ at low q. On the other hand R_{ee} mantains the value of 3.6 for the fully flexible chains, leading to an almost T-independent $\omega(q)$.

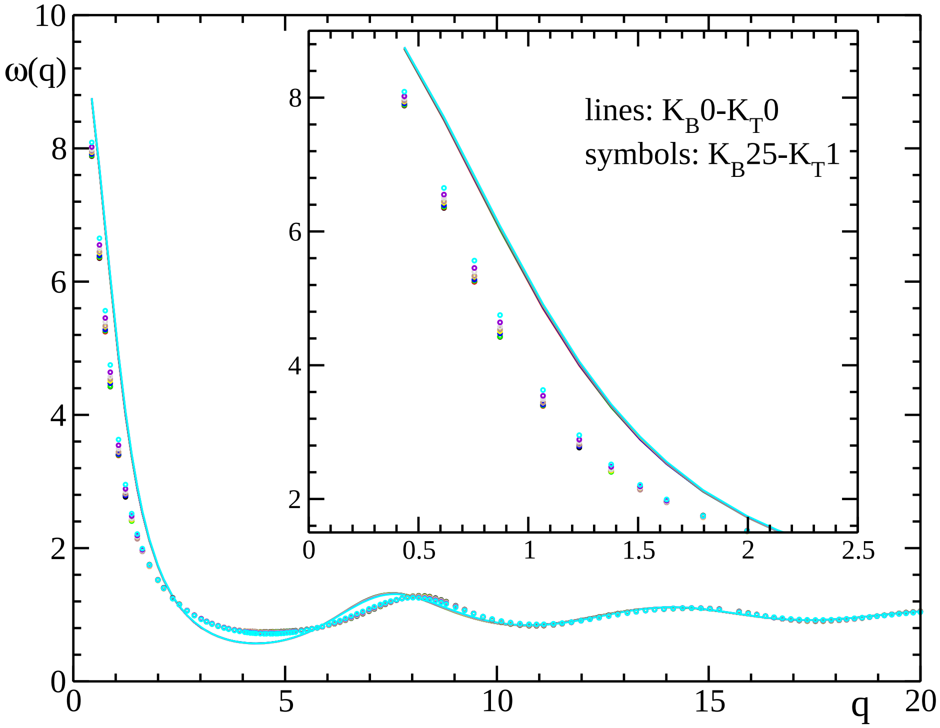

Figure 2.3: Form factor $\omega(q)$ as a function of temperature for fully flexible (lines) and stiff chains (points). The inset shows the same results at low q for clarity. Different colours correspond to different values of temperatures, following the legend in Fig 2.1 and 2.2.

2.1.3 Equivalent-Site Approximation and Ring Approximation

In figures 2.4 and 2.5 we test the validity of the equivalent site approximation for two representative cases here investigated of fully flexible chains ($K_{\mathrm{B}} = 0, K_{\mathrm{T}} = 0$) and stiff chains ($K_{\mathrm{B}} = 25, K_{\mathrm{T}} = 1$). Thus, we compare $c_{ab}(q)$ and $c(q)$ respectively obtained directly from Eq. (2.7) (i.e. from the RISM) and Eq. (2.9) (i.e. from the PRISM). Data correspond to the lowest temperature investigated for both cases. Both for fully flexible and for stiff chains, the approximation seems to be well satisfied. Only the functions involving the chain-end monomers, $a = 1$ (and $a = N$), present significant differences, which are just moderate in the region around $q_{\mathrm{max}} \approx 7$, the one giving the dominating contribution in the calculation of the integrals defining the MCT memory kernel (see chapter 3). Thus figures 2.4 and 2.5 suggest that Eq (2.8) is a reasonable approximation for the derivation of more tractable MCT equations for our model (see chapter 3).

Panels and their insets of Fig. 2.6 show a test of the ring approximation for respectively Eq. (2.10) and (2.11). The comparison is done both for the fully flexible case ($K_{\mathrm{B}} = 0, K_{\mathrm{T}} = 0$) and for a representative stiff case ($K_{\mathrm{B}} = 25, K_{\mathrm{T}} = 1$). Except for quantities related to end chain monomers, the ring approximation is well satisfied. The quality of the approximation is the same for fully flexible and stiff chains.

With all these results we conclude that the equivalent-site approximation of the PRISM theory and the additional ring approximation, introduced in the MCT equations (see chapter 3) are fulfilled, to the same degree of agreement with simulation results, in all the investigated systems covering the limits of fully flexible and stiff chains.

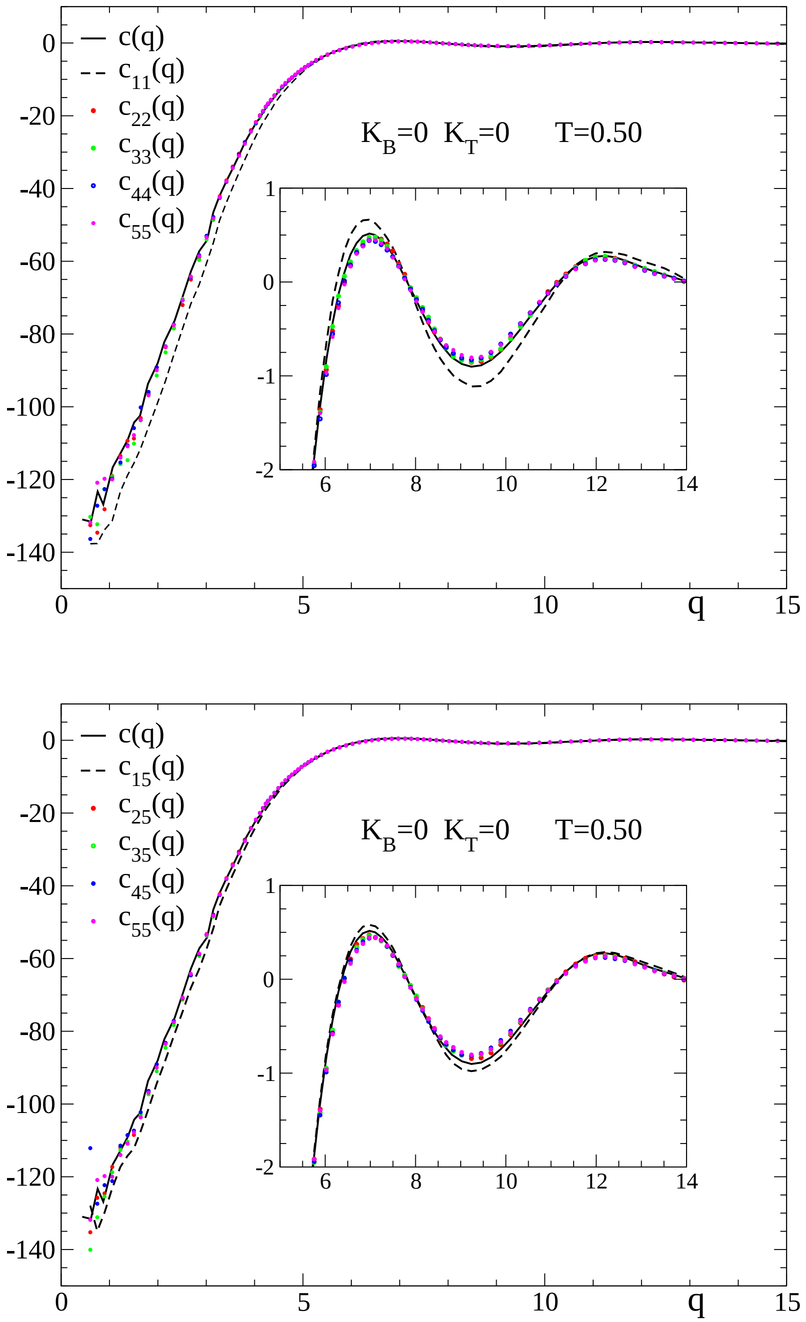

Figure 2.4: Test of the equivalent site approximation, Eq. (2.8), for the fully flexible chains at $T = 0.50$. Averaged functions $c(q)$ are determined from the simulation results for $S(q)$ and $\omega(q)$ via Eq. (2.9). The site-site direct correlation functions $c_{ab}(q)$ are calculated from the simulation results for $S_{ab}(q)$ and $\omega_{ab}(q)$ via Eq. (2.7). The insets represent the region around the maximum $q_{\max}$ of the static structure factor $S(q)$.

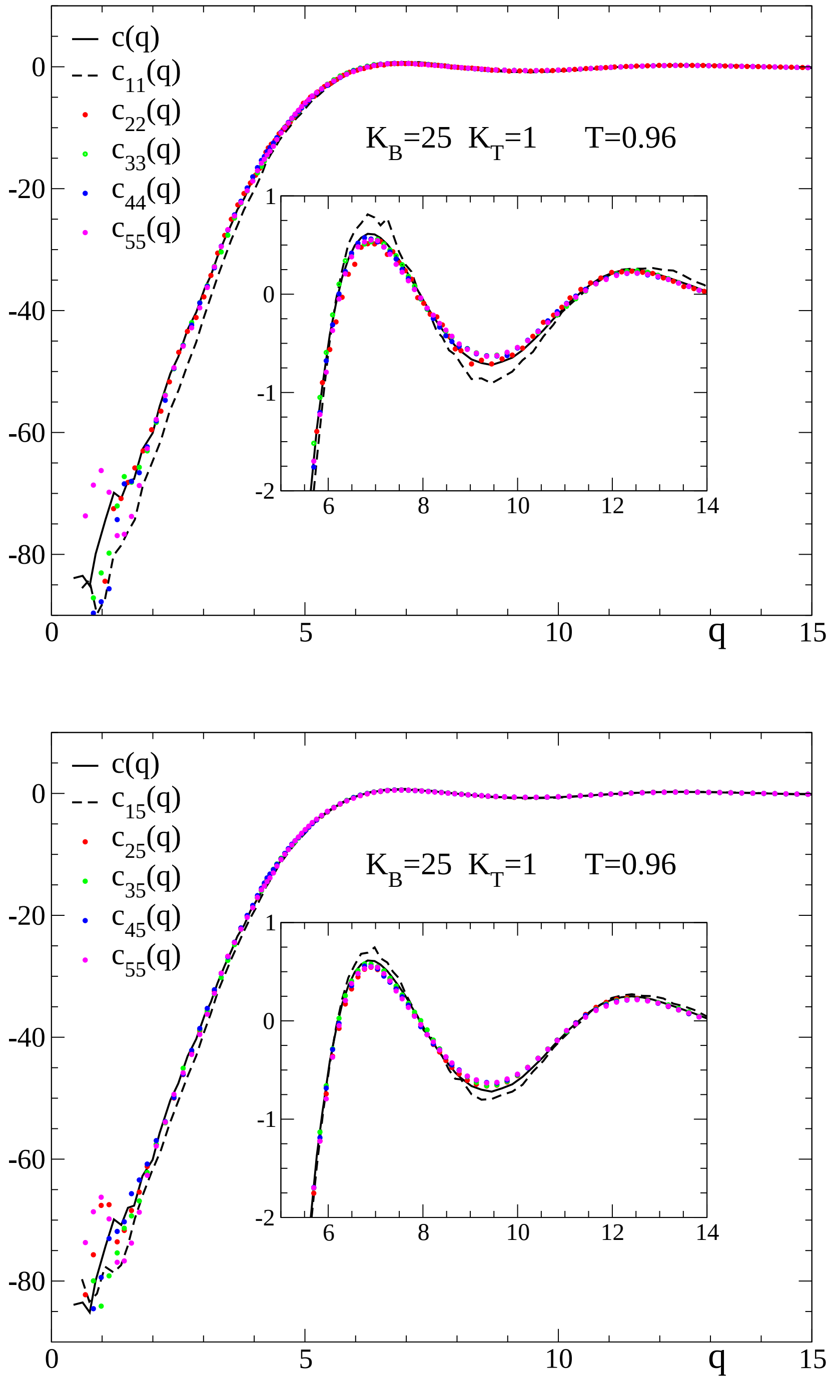

Figure 2.5: Test of the equivalent site approximation, Eq. (2.8), for a representative stiff case at $T = 0.96$. Averaged functions $c(q)$ are determined from the simulation results for $S(q)$ and $\omega(q)$ via Eq. (2.9). The site-site direct correlation functions $c_{ab}(q)$ are calculated from the simulation results for $S_{ab}(q)$ and $\omega_{ab}(q)$ via Eq. (2.7). Insets represent the region around the maximum $q_{\max}$ of the static structure factor $S(q)$.

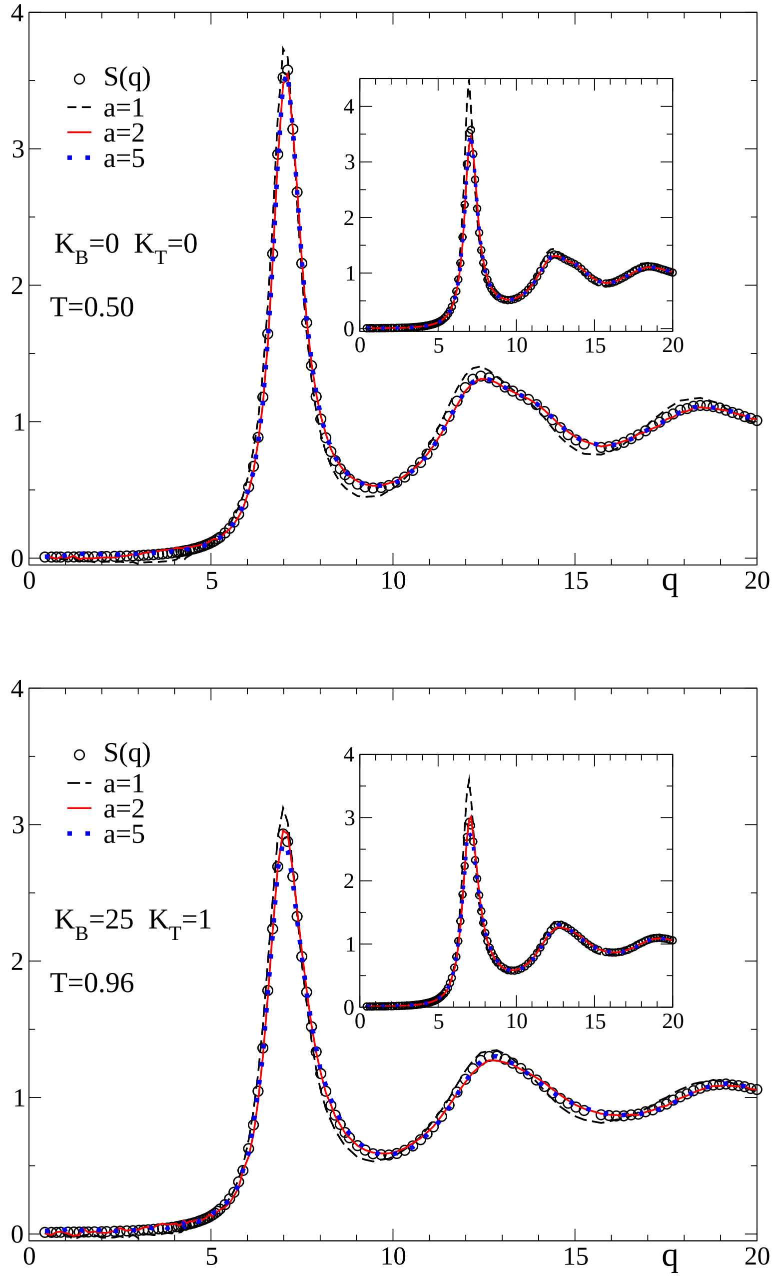

Figure 2.6: Test of the ring approximation for the fully flexible and stiff case, at respectively $T = 0.50$ and $T = 0.96$. The main panels show a comparison of the static structure factor $S(q)$ (circles) with the site-dependent structure factor (lines) $\widetilde{S_a}(q)$ for a=1,2 and 5. The insets compare $S(q)$ with $1/\widetilde{S_a}^{-1}(q)$ (lines) for a=1,2 and 5.

2.2 Dynamic Properties

In this section we show some phenomenological dynamic features induced by the introduction of intramolecular barriers in our model, going from the fully flexible to the stiff limit. At melt density of order of $\rho \sim 1$, as in our systems, there is no free space for large ballistic motion. The monomer is trapped in a cage and simultaneously cages its neighbours. Any displacement over large distances requires collective spatio-temporal fluctuations of the density around its mean value ρ on the scale of the nearest neighbour shells. These dynamic features are addressed by the dynamic density-density correlator (i.e., the intermediate coherent scattering function) $f(q,t) = \langle \rho(-\mathbf{q},0)\rho(\mathbf{q},\mathbf{t})\rangle / S(q)$ normalized to its initial value $S(q)$, the self density-density correlator (i.e., the incoherent scattering function) defined as $f^{\mathrm{s}}(q,t) = M^{-1}\langle \sum_{j=1}^{n}\sum_{a=1}^{N} \rho_j^a(-\mathbf{q},t)\rho_j^a(\mathbf{q},0)\rangle$ and the monomer mean squared displacement $\langle(\Delta r)^2(t)\rangle$.

2.2.1 Mean Squared Displacements (MSD)

Panels in Fig. 2.7 show the T-dependence of the monomer mean squared displacement (MSD) for fully-flexible and representative stiff chains with $(K_{\mathrm{B}}, K_{\mathrm{T}}) = (25,1)$. We observe similar features in both cases, but also some differences. After the initial ballistic regime, a plateau extends over longer times with decreasing temperature. This plateau corresponds to the caging regime — i.e., the temporary trapping of each monomer in the shell of neighboring monomers around it — which is usually observed when approaching a liquid-glass transition [5, 100, 107, 108]. At longer times, leaving the plateau, a crossover to a Rouse-like sublinear regime $\langle(\Delta r)^2(t)\rangle \propto t^{0.65}$ [100, 101] is observed for the fully-flexible case (see section 2.3). Thus this subdiffusive behaviour can be attributed to chain connectivity which determines the monomer dynamics in the range $1 \lesssim \langle \Delta r^2(t)\rangle \lesssim R_{ee}^2$. The final crossover to linear diffusion $\langle(\Delta r)^2(t)\rangle \propto t$ is reached, within the simulation time window, at long times only for the highest investigated temperatures. However, for the case of stiff chains it is difficult to discriminate power-law behaviour over significant time windows. Apparently, the linear diffusive regime is not reached within the simulation time window.

Figure 2.8 shows mean squared displacements for a fixed value of temperature $T = 1.5$, as a function of the barrier strength. We observe that increasing the strenght of the internal barriers in our model leads to slower dynamics at fixed temperature and density.

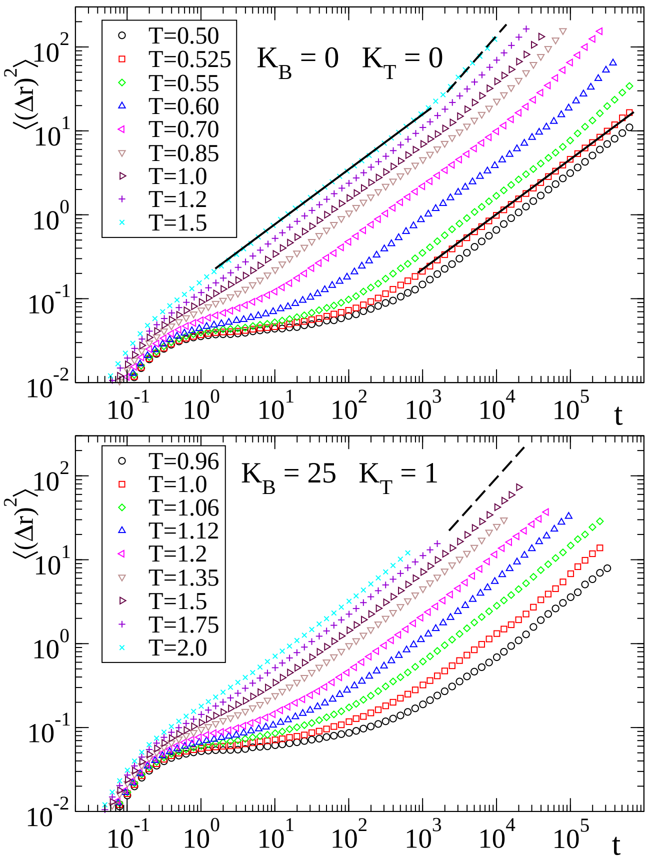

Figure 2.7: Temperature dependence of the monomer mean squared displacement for fully-flexible (top) and stiff chains with $(K_{\mathrm{B}}, K_{\mathrm{T}}) = (25, 1)$ (bottom). The solid and dashed lines indicate respectively sublinear ($\sim t^{0.65}$) and linear behavior.

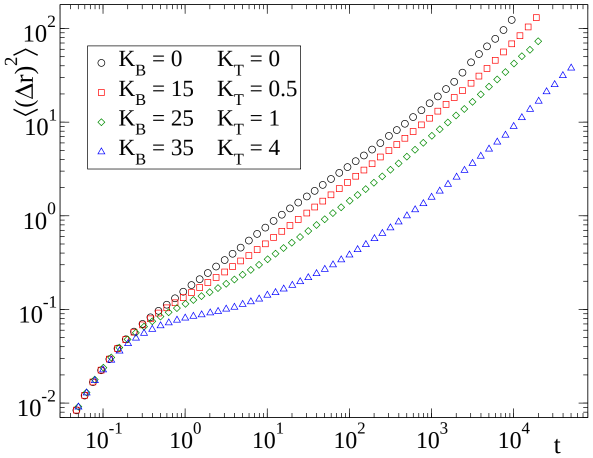

Figure 2.8: Mean squared displacement as a fuction of the barrier strength at fixed temperature $T = 1.5$.

2.2.2 Density-Density Correlators

Fig. 2.9 shows simulation results at several temperatures, both for fully-flexible and stiff chains, for the normalized density-density correlator $f(q, t)$. In both cases the correlator is evaluated at the maximum, $q_{\mathrm{max}} \approx 7$, of the static structure factor $S(q)$ (see Fig. 2.10). As in the case of the MSD, both the fully-flexible and stiff cases exhibit the standard behavior in the proximity of a glass transition [100, 101]. After the initial transient regime, $f(q, t)$ shows a first decay to a plateau connected with the caging regime, i.e., the temporary trapping of each particle by its neighbors. On lowering the temperature this plateau extends over longer time intervals. At long times, a second decay is observed from the plateau to zero. This second decay corresponds to the structural α-relaxation.

Fig. 2.11a shows the self-density correlator $f^{\mathrm{s}}(q, t)$ at fixed $T = 1.5$ and for several values of the barrier strength. In all the cases the correlator is evaluated at the maximum, $q_{\mathrm{max}} \approx 7$ of the static structure factor $S(q)$. We observe that increasing the strenght of the internal barriers at fixed ρ and T leads to slower dynamics. In the fully flexible case $f^{\mathrm{s}}(q, t)$ decays to zero in a single step. On increasing the strength of the internal barriers $f^{\mathrm{s}}(q, t)$ exhibits the standard behavior in the proximity of a glass transition, with a longer caging regime for stronger barriers. However if we look at the static structure factors $S(q)$ at $T = 1.5$ in fig. 2.10 for the same values of bending and torsion constants, they are almost indistinguishable, showing the same position and intensity of the main peak at $q_{\mathrm{max}} \sim 7$ which is associated to the typical first neighbor distance $r \sim 2\pi/q_{\mathrm{max}} \sim 0.9$. This suggests that the physical origin of this slowing down is mainly related to the strength of the intramolecular barriers more than to the packing in the first neighbor shell.

To quantify the loss of memory of the initial state and the concomitant decay to zero of the density correlators, we introduce the α-relaxation time τ_{α}. Let us define $\tau_{0.2}$ as the time for which $f^{\mathrm{s}}(q_{\mathrm{max}}, \tau_{0.2}) = 0.2$. This time corresponds to a significant decay from the plateau, and therefore it can be used as an operational definition of the α-relaxation time τ_{α}. Fig. 2.11b shows $\tau_{0.2}$ as a funcion of T, for different values of the bending and torsional constants. As observed in the analysis of the self-correlators (Fig. 2.11a), increasing the chain stiffness slows down the dynamics. At fixed temperature, the relaxation time for the stiffest investigated chains increases by several decades with respect to the fully-flexible case.

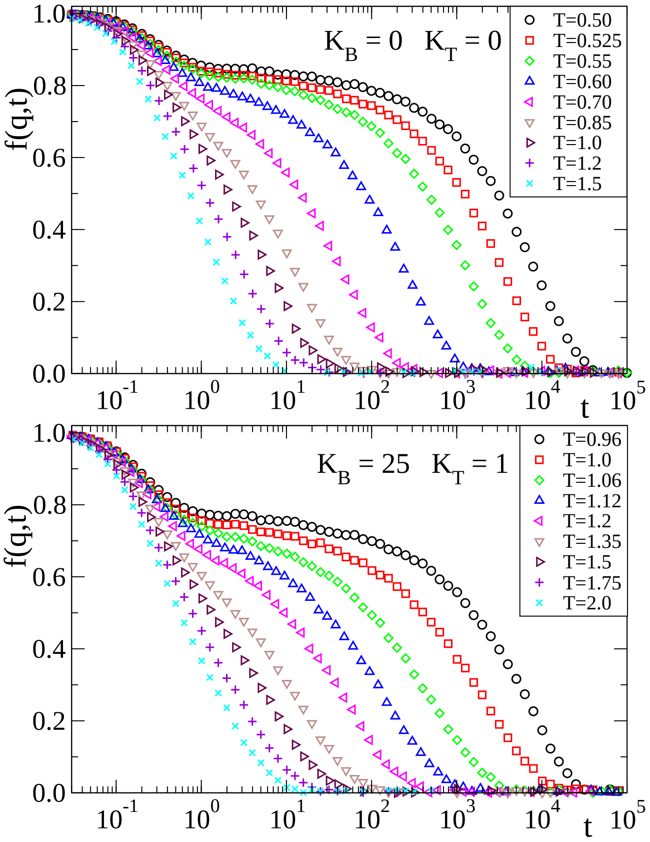

Figure 2.9: Temperature dependence of $f(q,t)$ for fully-flexible (top) and stiff chains with $(K_\mathrm{B}, K_\mathrm{T}) = (25, 1)$ (bottom). The wave vector is $q_\mathrm{max} \approx 7$, in both cases corresponding to the maximum of the static structure factor $S(q)$.

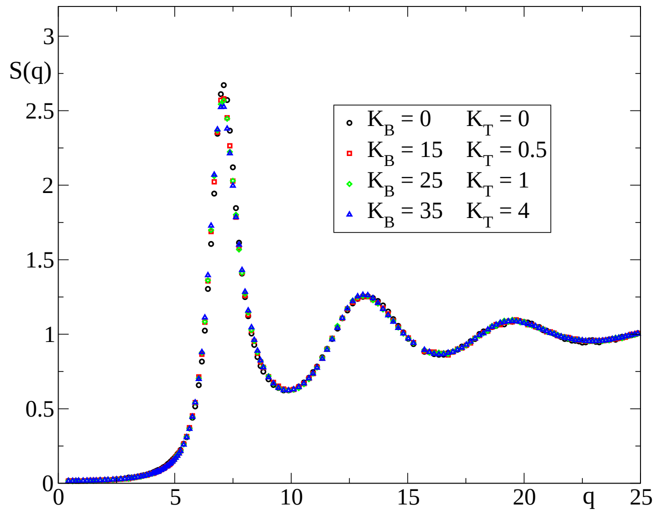

Figure 2.10: Static structure factor $S(q)$ for several values of the barrier strength at fixed temperature $T = 1.5$.

In this section we have demonstrated a main dynamic feature: the slowing down of the dynamics, at fixed density and temperature, by progressively increasing the strength of the intramolecular barriers. This feature strongly suggests that intramolecular barriers constitute an additional mechanism for dynamic arrest, coexisting with the general packing effects, present in all glass-formers, induced by density and temperature. In the next chapter we will discuss these simulation dynamic features within the framework of the Mode Coupling Theory.

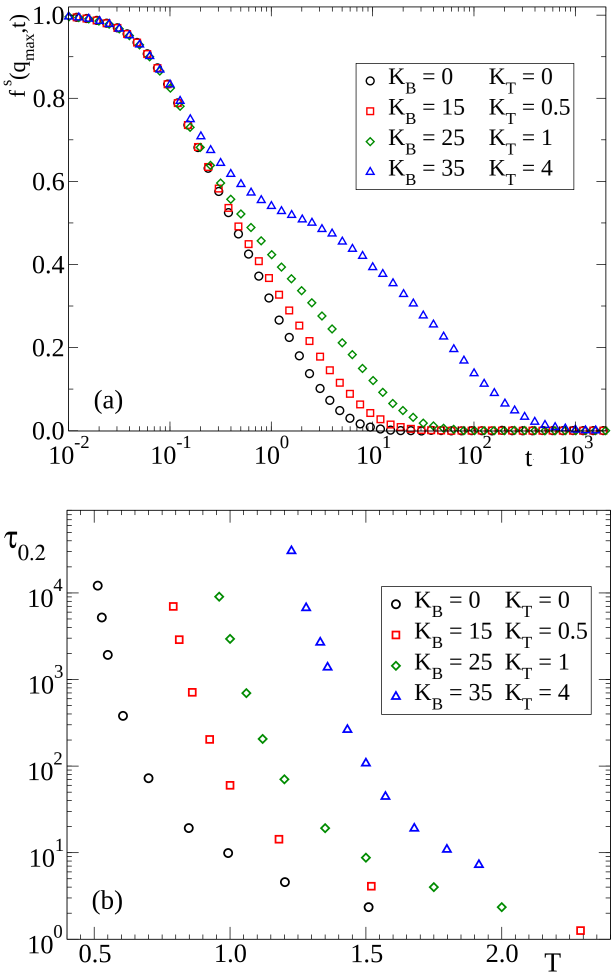

Figure 2.11: Panel (a): self-density correlator $f^{s}(q_{\max}, t)$, for several values of the barrier strength at fixed temperature $T = 1.5$. Panel (b): temperature dependence of the relaxation times $\tau_{0.2}$ of $f^{s}(q_{\max}, t)$, for the former values of the barrier strength.

2.3 Chain Dynamics: Rouse Model

The phenomenological Rouse model [25,27,84] is a Markovian model for polymer chain dynamics. It is the basic model describing dynamic features of non-entangled polymers. The starting point of a Markovian model for polymer dynamics is to assume a specific form for the intramolecular static correlations. In particular the starting point of the Rouse model is the Gaussian chain [27,109]. The Gaussian chain is the simplest model available to describe static properties of polymer chains. If we look at the conformation of a flexible polymer chain on length scales larger than the main bond length l_0, we can coarse grain the chemical details and the chain conformation will be close to a random walk of N steps. Several chain bonds are coarse grained onto a gaussian segment (or bead) of vector $\mathbf{x}_j = \mathbf{r}_j - \mathbf{r}_{j-1}$, where $\mathbf{r}_j$ is the position vector of the segment $j = 1, ..., N$. The length distribution of the end-to-end vector $\mathbf{R}_{ee} = \mathbf{r}_N - \mathbf{r}_1$ is Gaussian:

$$\Psi(R_{ee}) = \left(\frac{3}{2\pi N l^2}\right)^{3/2} \exp\left(-\frac{3R_{ee}^2}{2Nl^2}\right) \tag{2.12}$$

For the segment length we have $l^2 = l_0^2 C_\infty$, where the characteristic ratio C_∞ accounts for the local stiffness arising from the non-random distribution of the bond lenght l_0. In this way the average square end-to-end radius can be expressed as $\langle R_{ee}^2 \rangle = N l_0^2 C_\infty$. In the Gaussian model, a chain is considered ideal, in the sense that every bond vector $\mathbf{x}$ of the chain has a Gaussian distribution of lenghts:

$$\Phi(x) = \left(\frac{3}{2\pi b^2}\right)^{3/2} \exp\left(-\frac{3x^2}{2b^2}\right) \tag{2.13}$$

with $b^2 = \langle x^2 \rangle$. Thus for a Gaussian chain $C_\infty = 1$. A cornerstone of polymer physics is the ideality hypothesis formulated by Flory in the 1940s [109–111]. The Flory's hypothesis states that in a polymer melt chain conformations are Gaussian on a length scale much larger than the monomer diameter. The justification of this hypothesis is that, unlike in a good solvent, in a melt intrachain and interchain excluded volume interactions compensate each other beyond some length scale. Thus all the correlations are assumed to be short ranged. In chapter 1 we observed that $C_\infty \sim 1.3$ for fully flexible bead-spring chains (no intramolecular barriers). Hence chain conformations provided by MD simulations on the fully-flexible bead-spring model are almost Gaussian. Differences are related to the intrinsic stiffness of the bead-spring chains, due to intrachain excluded volume interactions at the monomer level.

By introducing intramolecular barriers, the value of C_∞ (see Fig. 1.3) increases and chain conformations progressively depart from Gaussian behaviour. This feature will be discussed in the next section in the framework of the Rouse model. Let us now introduce the basic features of the Rouse Model [25].

In the Rouse model a tagged chain is represented as a string of N beads of coordinates $\mathbf{r}_j$ connected by harmonic springs of force constant $k_s = 3k_\mathrm{B}T/b^2$, which represents the entropic restoring force driving the dynamics. The interactions of the tagged chain with the surroundings are given by a constant and position independent friction coefficient ζ and by a set of stochastic forces $\mathbf{f}_j(t)$ acting over each jth bead and fulfilling the condition $\langle \mathbf{f}_j(t)\rangle = 0$. The Markovian approximation enters the model by neglecting memory effects related to slow density fluctuations of the surroundings around the tagged chain. This means that the motion of a bead of the tagged chain is slow compared to the stochastic surroundings. As a consequence, stochastis forces are spatially and time uncorrelated and are related to the friction coefficient through the fluctuation dissipation theorem:

$$\langle \mathbf{f}_j(t)\cdot \mathbf{f}_k(t')\rangle = 6\zeta k_\mathrm{B}T\delta_{jk}\delta(t-t') \tag{2.14}$$

With these ingredients the Langevin equation for bead motion, neglecting the intertial term, reads:

$$\zeta\frac{\partial \mathbf{r}_j(t)}{\partial t} = -\frac{\partial U\{\mathbf{x}_j\}}{\partial \mathbf{r}_j} + \mathbf{f}_j(t) \tag{2.15}$$

The free energy $U\{\mathbf{x}_j\}$ of the Gaussian chain is given by the configurational entropy:

$$U\{\mathbf{x}_j\} = -TS\{\mathbf{x}_j\} = -k_\mathrm{B}T\ln P(\{\mathbf{x}_j\}) \tag{2.16}$$

where $P(\{\mathbf{x}_j\})$ is the Gaussian probability of a conformation $\{\mathbf{x}_j\}$:

$$P(\{\mathbf{x}_j\}) = \left(\frac{3}{2\pi b^2}\right)^{\frac{3}{2}N} \exp\left[-\sum_{j=2}^{N}\frac{3\left[\mathbf{r}_j - \mathbf{r}_{j-1}\right]^2}{2b^2}\right] \tag{2.17}$$

The Rouse equation of motion now reads:

$$\zeta\frac{\partial \mathbf{r}_j(t)}{\partial t} = k_s[\mathbf{r}_{j+1}(t) - 2\mathbf{r}_j(t) + \mathbf{r}_{j-1}(t)] + \mathbf{f}_j(t) \tag{2.18}$$

Hydrodynamic and excluded volume interactions are neglected in the Rouse model. Initially developed for describing the chain dynamics in solutions, where hydrodynamic interactions are important, (indeed the Zimm model [26, 27] is used in this case), the Rouse model turned out to be more succesful to describe chain dynamics in polymer melts, where hydrodynamic and excluded volume interactions are screened [27].

Equation 2.18 can be solved by mapping the chain motion onto a set of normal modes (Rouse modes) labelled by $p = 0, 1, 2, ..., N-1$, of wavelength N/p, and defined as:

$$\mathbf{X}_p(t) = \sum_{j=1}^{N} P_{jp}\mathbf{r}_j(t) \qquad \text{with} \qquad P_{jp} = \sqrt{(2-\delta_{p0})/N}\cos[(j-1/2)p\pi/N] \tag{2.19}$$

Let us note that we will use here and in the following, definitions and notations adapted to the scheme proposed by Chong *et al.* [39] for the MCT equations of the Rouse modes. Standard definitions differ from the ones used here only by constant factors and constant additive terms [27].

The Langevin equation for the Rouse modes now reads:

$$2N\zeta\dot{\mathbf{X}}_p(t) = -k_p\mathbf{X}_p(t) + \mathbf{g}_p(t) \tag{2.20}$$

where $k_p = 24Nk_\mathrm{B}Tb^{-2}\sin^2[p\pi/2N]$ and the external force for the pth mode reads $\mathbf{g}_p(t) = 2\sum_{j=1}^{N}\mathbf{f}_j(t)\cos[(j-1/2)p\pi/N]$. Integration of equation 2.20 leads to:

$$\mathbf{X}_p(t) = \frac{1}{2N\zeta}\int_{-\infty}^{t} dt' \exp\left((t-t')/\tau_p\right)\mathbf{g}_p(t') \tag{2.21}$$

Let us define the Rouse mode correlators as $C_{pp'}(t) = [\langle\mathbf{X}_p(0)\cdot\mathbf{X}_{p'}(t)\rangle - \delta_{0,p\times p'}\langle\mathbf{X}_p(0)\cdot\mathbf{X}_{p'}(0)\rangle]/3N$. From the definition it is obvious that $C_{00}(0) = 0$ and $C_{0p}(0) = 0$ for $p > 0$. Full uncorrelation of the Rouse stochastic forces, i.e. $\langle\mathbf{g}_p(t)\cdot\mathbf{g}_{p'}(t')\rangle \sim \delta_{pp'}\delta(t-t')$ yields orthogonality and exponentiality of the Rouse modes, leading to the expression for $p, p' > 0$:

$$C_{pp'}(t) = \hat{C}_{pp'}(0)\exp[-t/\tau_p] \qquad \text{with} \qquad \hat{C}_{pp'}(0) = \delta_{pp'}(b^2/24N^2)\sin^{-2}[p\pi/2N]. \tag{2.22}$$

The relaxation time τ_p of the mode p reads:

$$\tau_p = (\zeta b^2/12k_\mathrm{B}T)\sin^{-2}[p\pi/2N] \tag{2.23}$$

Thus according to the Rouse model, for $p << N$, $\hat{C}_{pp}(0)$ and τ_p scale as $\sim p^{-2}$.

The chain center-of-mass coincides with $\mathbf{R}_{cm} = \mathbf{X}_0(t)/\sqrt{N}$, thus the correlator $C_{00}(t)$ is related to the mean squared displacement of the center of mass of the chain:

$$\langle(\mathbf{R}_{cm}(t) - \mathbf{R}_{cm}(0))^2\rangle = -6C_{00}(t) = 6\frac{k_\mathrm{B}T}{N\zeta}t. \tag{2.24}$$

The motion of the center of mass of the bead-spring chain is identical to the motion of a particle that experiences a friction ζ. The self-diffusion coefficient can be easily evaluated:

$$D = \lim_{t\to\infty}\frac{\langle\Delta R_{cm}^2\rangle}{6t} = \frac{k_\mathrm{B}T}{N\zeta}. \tag{2.25}$$

By back transforming Eq 2.19 together with Eq. 2.22 it is possible to express the bead mean squared displacement as:

$$\langle\Delta r^2(t)\rangle = \langle\Delta R_{cm}^2\rangle + 6\sum_{p=1}^{N-1}[C_{pp}(0) - C_{pp}(t)] \tag{2.26}$$

For $N \to \infty$, inserting Eq. (2.22) and taking the continuous limit for the second term of the right side [27, 84], Eq. 2.26 is transformed into:

$$\langle\Delta r^2(t)\rangle = 6Dt + 2b^2\left(\frac{3k_\mathrm{B}Tt}{\pi\zeta b^2}\right)^{1/2}. \tag{2.27}$$

In contrast to normal diffusion, the bead mean square displacement at intermediate times shows a subdiffusive regime, growing as $\sim t^{1/2}$. The existence of such subdiffusive regime is one of the fundamental predictions of the Rouse model. In the previous section we observed this sub-diffusive regime $\langle\Delta r^2(t)\rangle \sim t^\beta$ for fully flexible chains (see Fig. 2.7). However the exponent was found to be $\beta \sim 0.65$, higher than the predicted value of 0.5. This difference arises from finite size effects due to the short length of our chains. Remember that the exponent 0.5 arises from integration in Eq. 2.26 in the limit $N \to \infty$.

Despite the Rouse model has been particularly successful in the description of chain dynamics in polymer melts, it has intrinsic limitations. First of all the predictions of the Rouse model are not valid at short lenght scales, i.e., the high p-regime. Indeed the $\alpha-$structural relaxation occurs at such length scales. Dynamics in the time window around the $\alpha-$relaxation time is implicitly coarse-grained in the phenomenological Rouse model. Moreover for sufficiently long chains topological interactions, which are a manifestation of the chain connectivity and uncrossability of the chains, play a crucial role. For the number of monomers N larger than the so-called entanglement lenght N_e, chain dynamics are better described by the reptation theory [27]. Looking at the mean squared displacement, for $N > N_e$ after the Rouse regime new sublinear regimes arise before the final crossover to free diffusion occurs. However this is not our case, since for our model the $N_e \sim 35$ and we are simulating chains of $N = 10$ monomers.

In the next sections we will test the Rouse predictions for our systems, and we will show how these predictions are strongly altered by the introduction of intramolecular barriers.

2.3.1 Intrachain Static Correlations

In this secion we test orthogonality and scaling behaviour for the static amplitudes $\hat{C}_{pp'}(0)$. In order to test the orthogonality of the Rouse modes for our systems we computed off-diagonal terms of the static observable $\Psi_{pp'} = \langle \mathbf{X}_p(0) \cdot \mathbf{X}_{p'}(0)/(X_p(0)X_{p'}(0)) \rangle$, the diagonal terms are trivially $\Psi_{pp} \equiv 1$. Data for fully-flexible chains (not shown) exhibit small deviations from orthogonality, indeed $|\Psi_{pp'}| < 0.05$ for all $p \neq p'$, independently of T. Instead, orthogonality is clearly violated for strong intramolecular barriers, as shown in the contour plot of Fig. 2.12a. Moreover, deviations are enhanced by decreasing T. Having noted this, modes p, p' of distinct parity fulfill $|\Psi_{pp'}| < 0.1$, i.e., they are approximately orthogonal even for the stiffest investigated system. Fig. 2.12b shows the diagonal terms $\hat{C}_{pp}(0)$ normalized by $\hat{C}_{11}(0)$. Data for fully-flexible chains approximately follow gaussian behaviour, $\hat{C}_{pp}(0) \sim p^{-2.2}$ [69, 100]. The introduction of chain stiffness leads to strong non-gaussian behaviour, which can be quantified at intermediate and low p by an approximate power law $\hat{C}_{pp}(0) \sim p^{-x}$, with higher x-values for stronger barriers [52]. The exponent $x \approx 3$ observed in $(K_{\mathrm{B}}, K_{\mathrm{T}}) = (25, 1)$ at $T \approx 1.0$ (fig. 2.12b) is similar to that found in simulations of 1,4-polybutadiene [52] with chemically realistic force fields. This is consistent with the similar values of C^r_∞

obtained for this polymer and for the bead-spring model at the former state point (see previous chapter). In the case $(K_{\mathrm{B}}, K_{\mathrm{T}}) = (35, 4)$, at the lowest investigated T, we find $x = 3.8$. The most local effects of intramolecular barriers are manifested by flattening of $\hat{C}_{pp}(0)$ at large p.

The non-gaussian behaviour in the systems with intramolecular barriers is observed for all p-values, i.e., it persists over all the length scale of the chain. Recent simulations performed by Steinhauser *et al.* [54, 55] on the Kratky-Porod [112] worm-like model show similar anomalous scaling, and a crossover to ideality, $\hat{C}_{pp}(0) \sim (N/p)^2$, at large values of the wavelength N/p. We want to stress that this feature is not an artifact of bead-spring models. It is also observed in simulations of real polymers. See e.g., Refs. [52] for simulations of 1,4-polybutadiene. There anomalous scaling $\sim p^{-3}$ is observed at short and intermediate wavelengths. This exponent is in qualitative agreement with our observations for $(K_{\mathrm{B}}, K_{\mathrm{T}}) = (25, 1)$ in Fig. 2.12b, which has a C_{∞}^{r} similar to that of 1,4-polybutadiene (see section 1.2). The reason why we do not observe the crossover to Gaussian scaling in our simulations is that we simulate very short chains, $N = 10$, which cannot probe the corresponding value N/p for the crossover wavelength. Gaussian statistics will be recovered at values of the mode wavelength, N/p, that can only be probed by chains longer than those ($N = 10$) investigated here. In summary, at the relevant length scales investigated here, the chains are strongly non-ideal, except in the fully-flexible limit $(K_{\mathrm{B}}, K_{\mathrm{T}}) \rightarrow (0, 0)$.

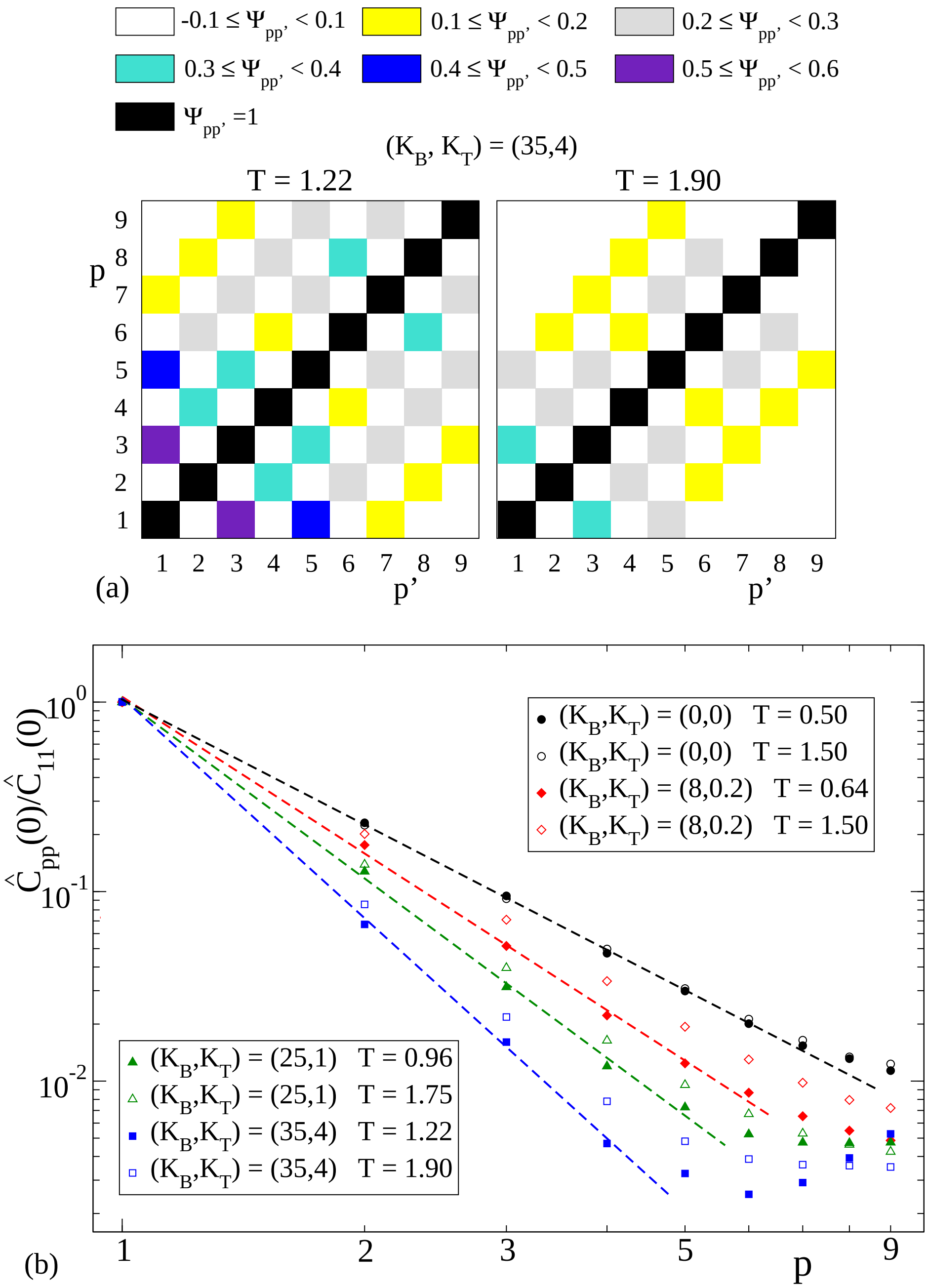

Figure 2.12: Static intrachain correlations computed from simulations. For each value of $(K_\mathrm{B}, K_\mathrm{T})$ (see legends) results include data at the highest and lowest investigated T. (a): for stiff chains with $(K_\mathrm{B}, K_\mathrm{T}) = (35, 4)$, contour plot of $\Psi_{pp'}$ (see text). (b): diagonal terms $\hat{C}_{pp}(0)$ (see text) normalized by $\hat{C}_{11}(0)$ for the sake of clarity. Each data set corresponds to a fixed value of $(K_\mathrm{B}, K_\mathrm{T})$ and T (see legend). Dashed lines indicate approximate power-law behaviour $\sim p^{-x}$. From top to bottom, $x = 2.2$, 2.7, 3.1, and 3.8.

2.3.2 Rouse Relaxation Times

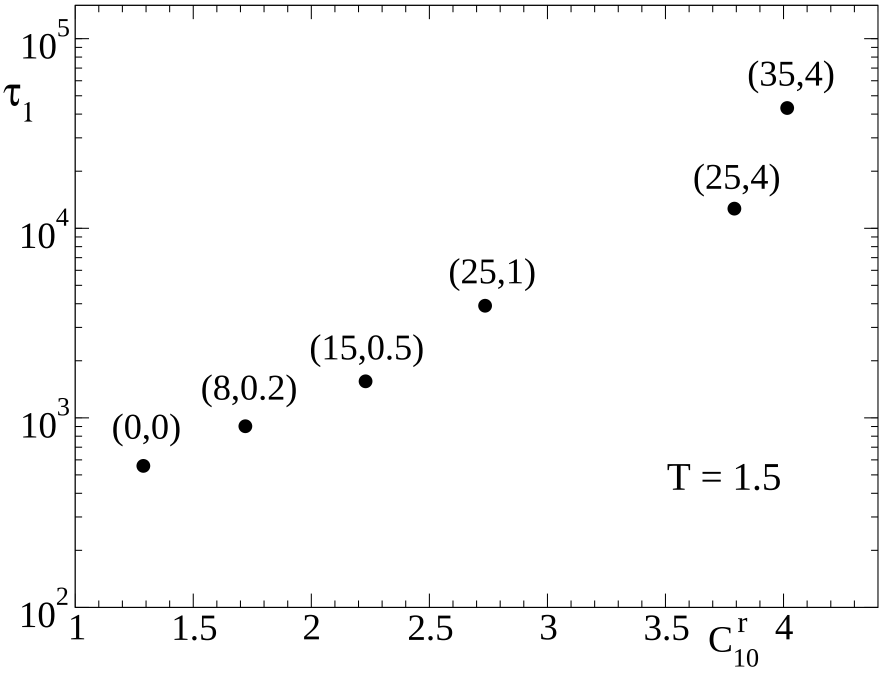

Figure 2.13: Relaxation time τ_1 of the mode $p = 1$ versus the characteristic ratio C^{r}_{10} at fixed temperature $T = 1.5$. The respective values of $(K_{\mathrm{B}}, K_{\mathrm{T}})$ are indicated on top of each symbol.

The trends observed for intrachain static correlations have their dynamic counterparts. Fig. 2.13 shows results for the relaxation time τ_1 of the mode $p = 1$ versus the characteristic ratio of the investigated systems at fixed $T = 1.5$. Relaxation times τ_p for the different p-modes are operationally defined as $\Phi_{pp}(\tau_p) = 0.3$, where $\Phi_{pp}(t) = C_{pp}(t)/\hat{C}_{pp}(0)$ is the normalized Rouse correlator. The obtained time τ_1 at $T = 1.5$ increases by about two decades over the investigated range of stiffness.

Fig. 2.14 shows the relaxation times τ_p, of the normalized mode correlators $\Phi_{pp}(t)$ as a function of the mode index p. We display data for several values of the bending and torsion constants $(K_{\mathrm{B}}, K_{\mathrm{T}})$ and temperatures T. The relaxation times have been operationally defined as $\Phi_{pp}(\tau_p) = 0.3$. Data can be again described at low-p by an effective power-law $\tau_p \sim p^{-x}$. The observed trends are analogous to those found for the static correlations (Fig. 2.12b). Rouse behavior ($x = 2$) is observed only in the fully-flexible limit. Again, as for the static amplitudes $\hat{C}_{pp}(0)$, x is weakly dependent on T (for example for $(K_{\mathrm{B}}, K_{\mathrm{T}}) = (25, 1)$ we find a variation of $\approx 7\%$ in x for a change in T of a factor 2) but strongly dependent on the barrier strength, taking higher values for stiffer chains. The x-values for $\hat{C}_{pp}(0)$ and τ_p at the same $(K_{\mathrm{B}}, K_{\mathrm{T}})$ and T are similar. This suggests that the structural origin of the observed dynamic anomalies is mainly controlled by intrachain static correlations.

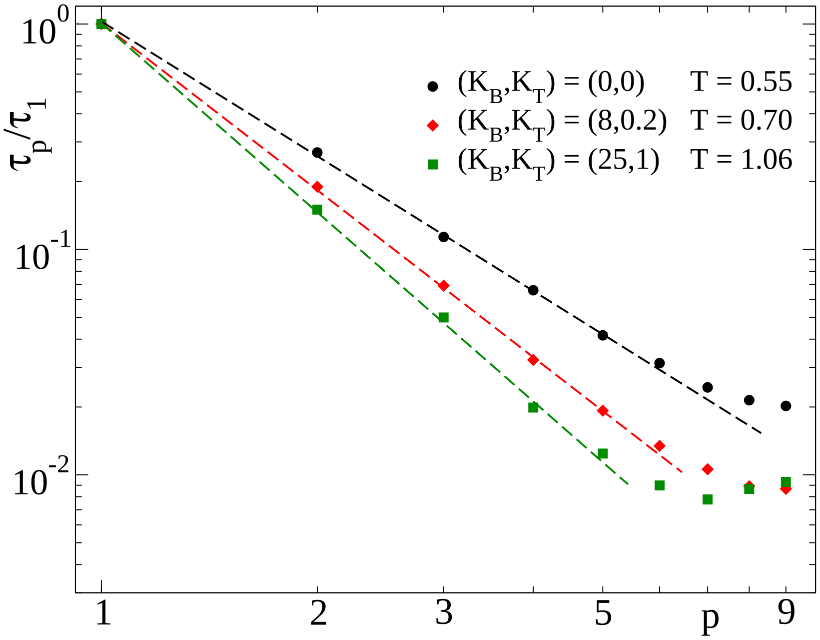

Figure 2.14: p-dependence of the relaxation times τ_p of the mode correlators. Each data set corresponds to a fixed value of $(K_{\mathrm{B}}, K_{\mathrm{T}})$ and T (see legends). For clarity, each set is rescaled by its respective τ_1. Dashed lines indicate approximate power-law behaviour $\sim p^{-x}$. From top to bottom: $x = 2.0$, 2.4, 2.8.

2.3.3 Rouse Correlators

Fig. 2.15 shows simulation results for the normalized Rouse correlators for the fully flexible and stiffest investigated case for two representative values of temperature T. Times are scaled by the relaxation time of the first mode τ_1. Data for fully flexible chains show the standard behaviour already observed in other works. After the plateau connected with the caging regime, correlators decay to zero in a single step. On the contrary data for stiff chains show new salient features. First, the unambiguous presence of a long-time plateau for the modes $p = 3$ and $p = 5$, followed by an ultimate slow decay. It must be stressed that this feature is not related to the structural α-relaxation. Indeed, the plateau arises at times far beyond the α-time scale ($\tau_\alpha \sim 5 \times 10^{-3}\tau_1$ for the considered T). This feature is instead intimately connected to the relaxation of the internal torsional degrees of freedom of the chain. Indeed fig. 2.16 shows that for fixed bending constant K_{B}, the long-time plateau tends to vanish as the value of the torsional constant K_{T} is decreased.

The observed long-time plateau constitutes a clear breakdown of the Rouse model, which predicts single, purely exponential decays of the mode correlators (see above). Its origin can be temptatively understood as follows. The relaxation of the pth-mode is equivalent to the relaxation of a harmonic oscillation of wavelength N/p . In the case of strong torsional barriers, the wavelengths of some particular modes probe characteristic lengths over which chain deformation involves a strong energetic penalty (due to the presence of the barriers). Thus, at the time scales for which the barrier amplitudes are probed, the relaxation of such modes becomes strongly hindered, leading to the observed long-time plateau regime and ultimate slow relaxation. Another intriguing feature of Fig. 2.15b, also inconsistent with the Rouse model, is the non-monotonous p-dependence of the mode correlators at intermediate times prior to the long-time plateau (see data for $p > 4$).

As we observed in Fig. 2.12 for $\Psi_{pp'}$, there are off-diagonal terms of the intrachain static correlations which are non-orthogonal. This non-orthogonality persists over long time scales, as can be seen in Fig. 2.17. The latter shows representative simulation results for normalized Rouse cross-correlators $\Phi_{pp'}(t)$, with $p = 3$ and $p' = 1, 3, 5, 7, 9$. Data correspond to the same temperatures and barrier strength (the stiffest investigated case) of the diagonal correlators of Fig. 2.15b.

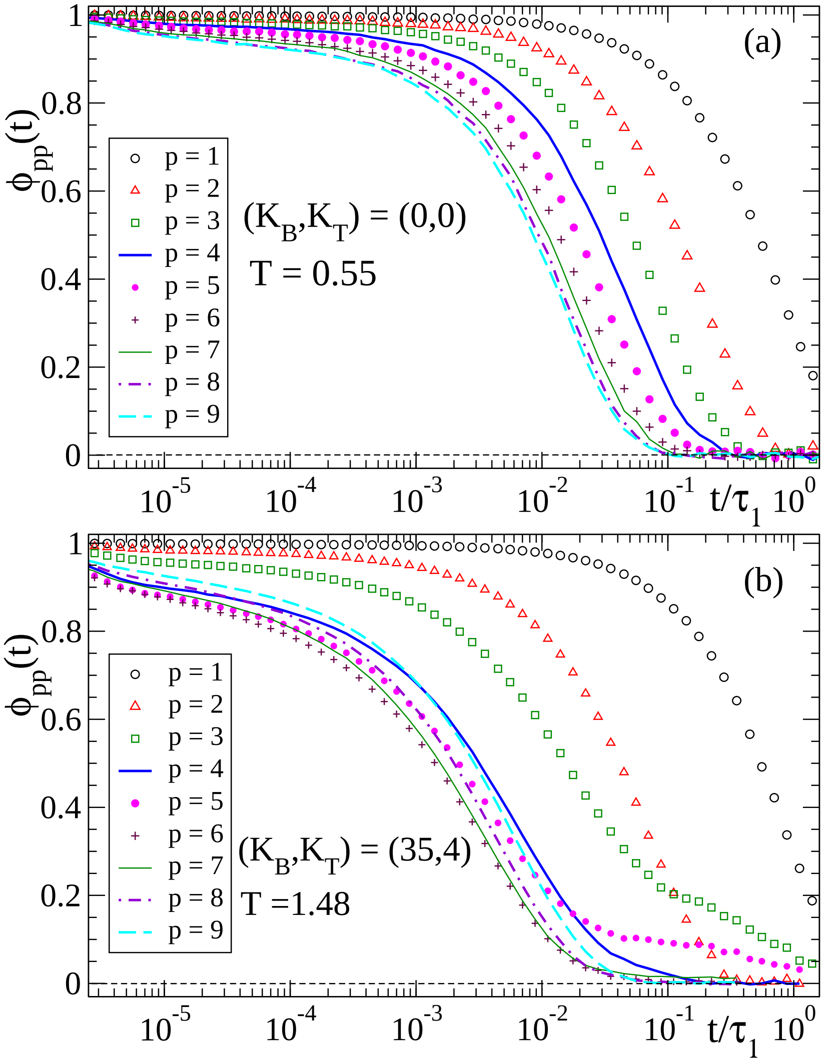

Figure 2.15: Panel (a): Normalized mode correlators $\Phi_{pp}(t)$ for fully-flexible chains with $(K_{\mathrm{B}}, K_{\mathrm{T}}) = (0, 0)$ at $T = 0.55$. Panel (b): $\Phi_{pp}(t)$ for stiff chains with $(K_{\mathrm{B}}, K_{\mathrm{T}}) = (35, 4)$ at $T = 1.48$. In both panels, the absolute time is rescaled by the relaxation time τ_1 of the $p = 1$ mode.

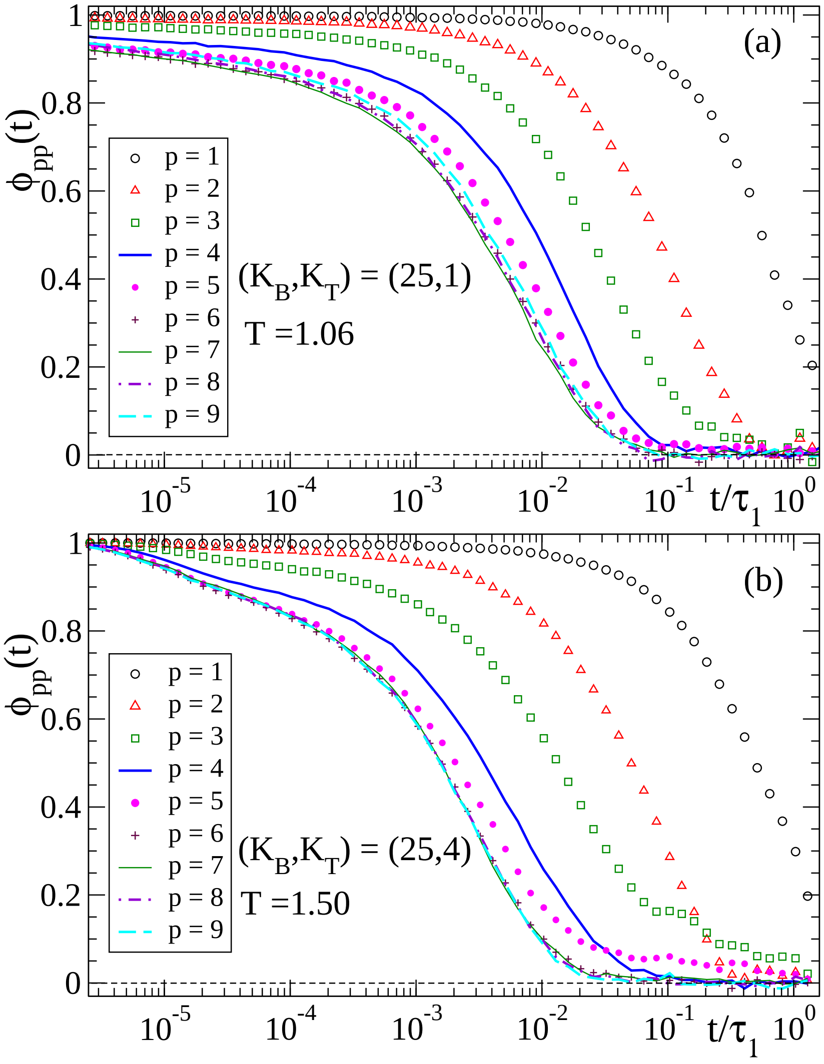

Figure 2.16: Normalized mode correlators $\Phi_{pp}(t)$ for stiff chains with $(K_\mathrm{B}, K_\mathrm{T}) = (25, 1)$ at $T = 1.06$ [panel (a)] and $(K_\mathrm{B}, K_\mathrm{T}) = (25, 4)$ at $T = 1.50$ [panel (b)]. In both panels, the absolute time is rescaled by the relaxation time τ_1 of the $p = 1$ mode

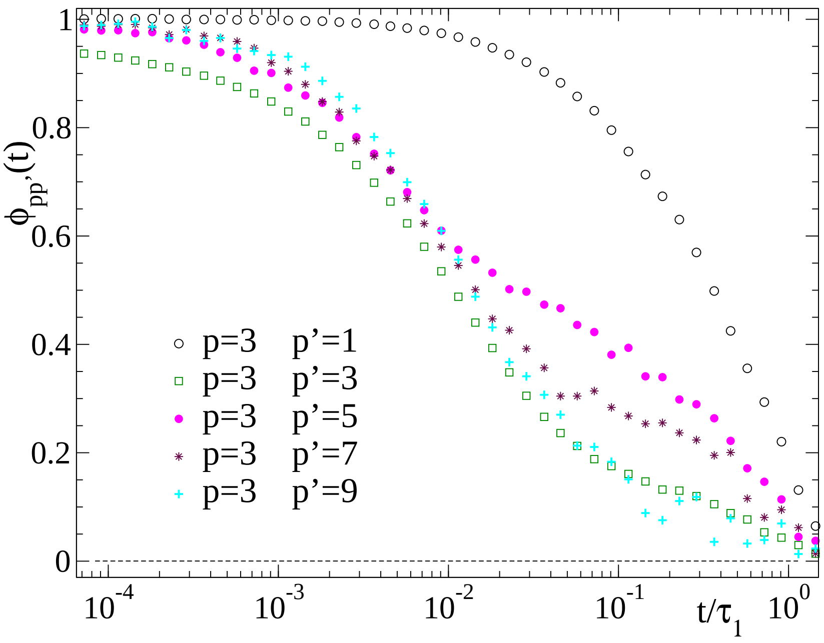

Figure 2.17: Normalized cross-correlators $\Phi_{pp'}(t)$ (for fixed $p = 3$) of stiff chains with $(K_{\mathrm{B}}, K_{\mathrm{T}}) = (35, 4)$ at $T = 1.48$. The absolute time is rescaled by the relaxation time τ_1 of the $p = 1$ mode.

Chapter 3

Mode Coupling Theory for Polymer Melts

Introduced in the early 80's by Götze and co-workers, the Mode Coupling Theory (MCT) of the glass transition is a theory aimed to describe the behaviour of density correlators as $F(q,t) = N^{-1}\sum_{i,j}\exp[i\mathbf{q}\cdot(\mathbf{r}_j(t)-\mathbf{r}_i(0))]$ in deeply supercooled liquids or dense colloids [4–8].

The important initial step in the theory is the fact that supercooled liquids show a separation of time scales, as we observed from the analysis of the MSD and the scattering functions computed from our simulation data in chapter 2. There are dynamical processes, such as vibrations, that occur on a microscopic time scale and others, such as the structural relaxation, that are observed on a time scale which is orders of magnitude longer than the former one. MCT makes use of this property of supercooled liquids by choosing the density distribution of the particle as the relevant slowly varying observable and by deriving equations of motion to describe the glass transition as a feedback mechanism driven by the slow density fluctuations.

The derivation of the MCT equations of motion from first principles is a rather complex and tedious mathematical task. A detailed exposition of it would require an unnecessary large space in this memory. Thus, here we just summarize the main steps and approximations involved in the former derivation. Complete expositions can be found in the extensive reviews of Refs. [4–8].

By starting from the fundamental Liouville equation of motion and using the Mori-Zwanzig projection operator formalism we arrive to an integro-differential equation for the density correlator:

$$\ddot{F}(q,t)+\frac{q^2k_BT}{mS(q)}F(q,t)+\frac{m}{Nk_BT}\int_0^t dt'\langle R_{-\mathbf{q}}(0)R_{\mathbf{q}}(t-t')\rangle\dot{F}(q,t')=0 \tag{3.1}$$

See appendix A for a schematic derivation of equation 3.1. This equation has been obtained by using projectors over the subspace spanned by the variables $A_{\mathbf{q}}=(\rho_{\mathbf{q}},\Upsilon^L_{\mathbf{q}})$, with $\rho_{\mathbf{q}}=\sum_i\exp(i\mathbf{q}\cdot\mathbf{r}_i)$ the total density fluctuation and $\Upsilon^L_{\mathbf{q}}=\sum_i\hat{\mathbf{q}}\cdot\mathbf{v}_i\exp(i\mathbf{q}\cdot\mathbf{r}_i)$ the so-called longitudinal current. Here $\hat{\mathbf{q}}=\mathbf{q}/q$, and $\mathbf{v}_i$ is the particle velocity. Equation 3.1 is equivalent to the equation of motion of a damped harmonic oscillator. The friction coefficient $\langle R_{-\mathbf{q}}(0)R_{\mathbf{q}}(t-t')\rangle$ of the damping term depends on the full history of the motion, so we refer to it as the MCT memory kernel. Equation 3.1 is exact, but however it is not solvable. This is because it contains a memory term $\langle R_{-\mathbf{q}}(0)R_{\mathbf{q}}(t-t')\rangle$ that cannot be exactly expressed in terms of the density correlators. This memory term is the correlator of the so-called fluctuating forces $R_{\mathbf{q}}(t)=R^0_{\mathbf{q}}(t)+R^1_{\mathbf{q}}(t)$. The latter terms are given by:

$$R^0_{\mathbf{q}}(t)=iq\sum_i(\hat{\mathbf{q}}\cdot\mathbf{v}_i(t))^2e^{i\mathbf{q}\cdot\mathbf{r}_i(t)}-\frac{iqk_BT}{mS(q)}\rho_{\mathbf{q}}(t) \tag{3.2}$$

and

$$R^1_{\mathbf{q}}(t)=\frac{i(2\pi)^3}{m}\sum_{\mathbf{k}}(\hat{\mathbf{q}}\cdot\mathbf{k})V_{\mathbf{k}}\rho_{\mathbf{q}-\mathbf{k}}(t)\rho_{\mathbf{k}}(t) \tag{3.3}$$

where $V_{\mathbf{k}}$ are the Fourier components of the interaction potential between particles. A closed set of solvable equations can only be achieved from (3.1) through the three MCT approximations:

i) We said above that the memory kernel can be regarded as a force-force correlation function. Interaction forces involve pairs of densities, for pair potentials. Thus we assume that the slow contribution to the fluctuating forces, which leads to the dynamic arrest in an amorphous phase, can be expressed in terms of the average of the product of four density fluctuations, schematically $\langle\rho_{-\mathbf{k}_1}(0)\rho_{-\mathbf{k}_2}(0)\rho_{\mathbf{k}_3}(t)\rho_{\mathbf{k}_4}(t)\rangle$. From Eqs. (3.2) and (3.3) it can be seen that the slow relaxation of the memory term $\langle R_{-\mathbf{q}}(0)R_{\mathbf{q}}(t-t')\rangle$ is dominated by $\langle R^1_{-\mathbf{q}}(0)R^1_{\mathbf{q}}(t-t')\rangle$. Thus, the first MCT approximation consists of reducing the (fast) regular part of the kernel (contributions from $R^0_{\mathbf{q}}(t)$) to a q-independent friction term (for Brownian dynamics), or dropping it (for Newtonian dynamics, as in the present case). This introduces an undertermined constant factor in the absolute time scale of the equations.

ii) Convolution approximation [105]: static three-point correlations (ensemble averages of products of three densities in q-space) are approximated in terms of products of static two-point correlations (i.e., products of static structure factors).

$$\langle \rho_{\mathbf{k}_1}(0)\rho_{\mathbf{k}_2}(0)\rho_{\mathbf{k}_3}(0)\rangle \approx N\delta_{-\mathbf{k}_3,\mathbf{k}_1+\mathbf{k}_2}S(k_1)S(k_2)S(k_3) \tag{3.4}$$

This approximation works well for isotropic interactions, not so much for directional ones (silica, systems with hydrogen bonds, patchy colloids...) [113].

iii)Kawasaki approximation: dynamic four-point correlations (two densities in q-space at $t = 0$ and other two at $t > 0$) are factorized in terms of products of dynamic two-point correlations (i.e., products of scattering functions).

$$\begin{aligned}\langle \rho_{-\mathbf{k}_1}(0)\rho_{-\mathbf{k}_2}(0)\rho_{\mathbf{k}_3}(t)\rho_{\mathbf{k}_4}(t)\rangle &\approx \langle \rho_{-\mathbf{k}_1}(0)\rho_{\mathbf{k}_3}(t)\rangle\langle \rho_{-\mathbf{k}_2}(0)\rho_{\mathbf{k}_4}(t)\rangle \\ &+ \langle \rho_{-\mathbf{k}_1}(0)\rho_{\mathbf{k}_4}(t)\rangle\langle \rho_{-\mathbf{k}_2}(0)\rho_{\mathbf{k}_3}(t)\rangle \end{aligned} \tag{3.5}$$

If we are too close to the glass transition the system becomes dynamically heterogeneous. We have coexistence of fast and slow regions which are not randomly distributed, but organized into clusters [114, 115]. This makes this third approximation no more valid around the time scale of the $\alpha-$relaxation. Indeed the so-called $\chi_4(t)$ functions [116–119], which quantify the breakdown of (3.5), exhibit a maximum around the $\alpha-$regime. This maximum grows in intensity on approaching the glass transition. Thus, if we are very close to the glass transition, MCT predictions for the $\alpha-$time scale break down.

After applying these three approximations, Eq. (3.1) is reduced to the following equation of motion for the normalized density-density correlator $f(q,t) = F(q,t)/S(q)$:

$$\ddot{f}(q,t) + \frac{q^2 k_B T}{mS(q)} f(q,t) + \frac{q^2 k_B T}{mS(q)} \int_0^t dt' m(q,t-t')\dot{f}(q,t') = 0 \tag{3.6}$$

The long time behaviour of $f(q,t)$ is governed by the memory function $m(q,t)$. This kernel is now a bilinear form in $f(q,t)$:

$$m(q,t-t') = \int \frac{d^3\mathbf{k}}{(2\pi)^3} \mathcal{V}(\mathbf{q}-\mathbf{k},\mathbf{k}) f(k,t-t') f(|\mathbf{q}-\mathbf{k}|,t-t') \tag{3.7}$$

where the vertex $\mathcal{V}(\mathbf{q}-\mathbf{k},\mathbf{k})$ is given by:

$$\mathcal{V}(\mathbf{q}-\mathbf{k},\mathbf{k}) = \frac{\rho}{2q^4} S(q)S(k)S(|\mathbf{q}-\mathbf{k}|)\left[\mathbf{q}\cdot\mathbf{k}c(\mathbf{k}) + \mathbf{q}\cdot(\mathbf{q}-\mathbf{k})c(|\mathbf{q}-\mathbf{k}|)\right]^2 \tag{3.8}$$

Here $c(q)$ is the so-called direct correlation function that, in a monoatomic fluid, is related to the static structure factor via the (exact) Ornstein-Zernike relation $c(q) = \rho^{-1}(1-1/S(q))$ [105]. Equation 3.8 shows that the memory kernel contains the factor $S(q)S(k)S(|\mathbf{q}-\mathbf{k}|)$. This means that the slow dynamics are mainly driven by fluctuations of pair densities on the length scale of the maximum $q_{\max}$ of the static structure factor $S(q)$.

Following a procedure analogous to the case of the density-density correlator, it is possible to derive a MCT equation of motion for the self-correlator:

$$\ddot{f}_s(q,t) + \frac{\rho k_B T}{m} f_s(q,t) + \frac{\rho k_B T}{m}\int_0^t dt' m_s(q,t-t')\dot{f}_s(q,t') = 0 \tag{3.9}$$

where the memory kernel is given by

$$m_s(q,t-t') = \int \frac{d^3\mathbf{k}}{(2\pi)^3} \mathcal{V}_s(\mathbf{q}-\mathbf{k},\mathbf{k}) f_s(|\mathbf{q}-\mathbf{k}|,t-t') f(k,t-t') \tag{3.10}$$

with the following expression for the vertex

$$\mathcal{V}_s(\mathbf{q}-\mathbf{k},\mathbf{k}) = \frac{\rho}{q^4} S(k)c^2(k)(\mathbf{q}\cdot\mathbf{k})^2 \tag{3.11}$$

Thus the memory function for the dynamics of the self correlator $f_s(q,t)$ contains the normalized density correlator $f(q,t)$ and hence we see that in order to obtain the time dependence of $f_s(q,t)$ [122] we need first to solve the MCT equations for the collective dynamics [6, 121].

According to Eqs. (3.6-3.8) and (3.9-3.11) the time evolution of density-density and self-correlators is *fully* determinated by the static structure of the system. Liquid state theories [105] provide a direct connection between the static structural information, given by $S(q)$ and $c(q)$, and the interaction potential of the system $V(r)$, as e.g., the Percus-Yevick (PY) theory: $c(r) = [1-\exp(V(r)/k_BT)](1+h(r))$. PY works well when the potential is strongly repulsive and short ranged [105]. Another well-known theory is the hypernetted-chain (HNC) theory: $c(r) = h(r) - \ln[1 + h(r)] - V(r)/k_BT$, which works better with soft-core potentials [120]. Thus MCT is, at least formally, a *first-principle* theory: if we know $V(r)$, we calculate the static quantities $S(q)$ and $c(q)$ through a good liquid state theory, insert these inputs in the MCT equations and obtain the dynamic correlators $f(q,t)$ and $f_s(q,t)$. If *a priori* we do not have a good theory for describing the $S(q)$ of our investigated system, we can provide $S(q)$ from experimental measurements or from simulations [19,113]. Equations (3.6-3.8) and (3.9-3.11) form a closed set of equations for the time dependece of $f(q,t)$ and $f_s(q,t)$. Thus the solutions of this set of equations are the correlation functions that can in principle be directly compared with experimental or simulation data.

So far we have discussed MCT equations for one-component monoatomic liquids. The archetype of them is the hard-sphere (HS) system [121–123]. Other examples, for which MCT equations have been solved, include effective ultrasoft potentials for highly penetrable colloids, as logarithmic interactions between star-polymers of high functionality (i.e., high number of arms) [13–15]. Another well-know case is the hard-sphere + square well (SW) model for the interaction between colloids in mixtures of colloids and polymers [47, 48]. The short-ranged SW comes out as an effective attraction between the colloids, which originates from the (entropic) depletion effect induced by the presence of the small polymers. Recently, a monoatomic model for effective interactions between fullerenes has been solved within MCT [124, 125].

Having said this, there are several universal predictions concerning the MCT-liquid-glass dynamics which follow as mathematical consequences of the general structure of the MCT equations and that are not restriced only to monoatomic liquids. Some of these universal predictions will be briefly summarized in the next section.

3.1 Universal MCT Predictions

One of the central predictions of MCT is the existence of a critical temperature T_c where the system shows structural arrest driven by the mutual blocking of each particle by its neighbours [4–8]. The *non-ergodicity parameter*, f_q, for wave vector q is defined as the long-time limit of $f(q,t)$, $\quad f_q = lim_{t \to \infty} f(q,t)$, and obeys the implicit equation

$$\frac{f_q}{1-f_q} = \mathcal{F}_q(\{f\}) \tag{3.12}$$

where we have introduced the mode-coupling functional $\mathcal{F}_q(\{f\}) = \lim_{t\to\infty} m(q,t)$, as the long time limit of the memory function. Using the definition of the memory kernel given in Eq. (3.7), Eq. (3.12) can be rewritten as

$$\frac{f_q}{1-f_q} = \int \frac{d^3\mathbf{k}}{(2\pi)^3} \mathcal{V}(\mathbf{q}-\mathbf{k},\mathbf{k}) f_{|\mathbf{q}-\mathbf{k}|} f_k \tag{3.13}$$

Analogously, we get the corresponding equations for the *self non-ergodicity parameter* $f_q^s = \lim_{t\to\infty} f_s(q,t)$

$$\frac{f_q^s}{1-f_q^s} = \mathcal{F}_q^s(\{f^s\},\{f\}) \tag{3.14}$$

$$\frac{f_q^s}{1-f_q^s} = \int \frac{d^3\mathbf{k}}{(2\pi)^3} \mathcal{V}_s(\mathbf{q}-\mathbf{k},\mathbf{k}) f^s_{|\mathbf{q}-\mathbf{k}|} f_k \tag{3.15}$$

The equations (3.13) and (3.15) can be solved by means of an iterative procedure. We observe that for all q, $f_q = 0$ ($f_q^s = 0$) is always a trivial solution. However if the vertices are sufficiently large there exist also solutions $f_q > 0$ ($f_q^s > 0$) and it can be shown that the physical nonergodicity parameter is the largest of these solutions. If such non-zero solutions exist, this implies that the system is no longer ergodic, since density fluctuations do not decay to zero even for long times. This means that cooperative rearrangements of the particles are inhibited and each particle becomes trapped in its cage because their neighbours are trapped. The highest temperature at which these positive solutions occur defines the critical temperature T_c of the mode-coupling theory. Fig. 3.1 illustrates the scenario predicted by MCT on approaching T_c.

This ergodic-to-nonergodic transition at T_c is called the idealized glass transition of the MCT and f_q (f_q^s) at T_c is referred to as the critical nonergodicity parameter f_q^c (f_q^{sc}) [6]. The latter quantifies the stability of the density fluctuations in the reciprocal space. Thus a higher value of f_q^c (f_q^{sc}) implies a stiffer character of the respective density fluctuations of wavelength $2\pi/q$. As we will see in the following, f_q^c (f_q^{sc}) has also the meaning of the plateau height in the two step relaxation of $f(q,t)$ ($f_s(q,t)$) (see also Fig. 3.1), and provides a measure of the localization length of the system (the dimension of the cage in which the particles are trapped).

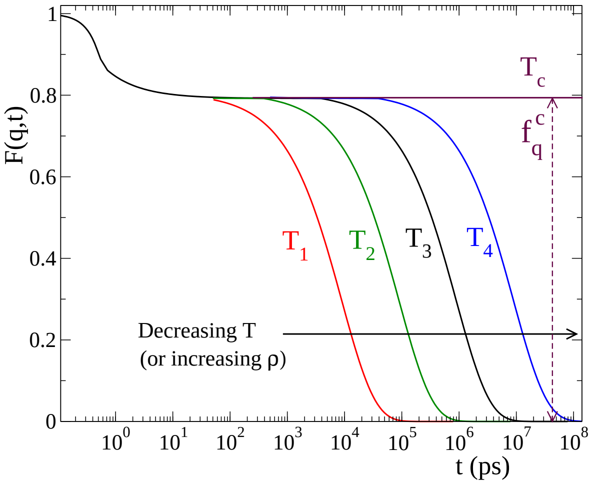

Figure 3.1: Schematic representation of the T-dependence of the density correlator $f(q,t)$ for a glass-forming system. For $T > T_c$ $f(q,t)$ exhibits a two step relaxation. On lowering the temperature, the long time limit of $f(q,t)$ jumps from zero to a finite value f_q^c when the critical temperature T_c is reached.

In reality, it is known that hopping events restore the ergodicity below T_c, and this transition is not really observed, i.e., the correlator does decay to zero at T_c [4–8, 107, 108, 126, 127]. Indeed T_c is higher than the real glass transition temperature T_g, typically $T_c \approx 1.2T_g$. Having said this, MCT is still a good theory for temperature higher but close to T_c. The existence of a critical temperature T_c allows us to introduce the separation parameter $|\epsilon| = |T - T_c|/T_c$ (it can also be $|\rho - \rho_c|/\rho_c$, and analogously for any other control parameter). The following results are valid only in the limit of small ϵ. This is why these predictions are often referred to as MCT asymptotic laws. MCT predicts that for temperature close to but above T_c, the dynamics of any time-dependent correlator $\phi(q,t)$, coupled to density fluctuations, exhibits a two step relaxation: the relaxation towards the plateau, and the final relaxation from the plateau to zero. These relaxations are respectively characterized by two different time scales defined by:

$$t_\sigma = t_0|\sigma|^{-\frac{1}{2a}} \tag{3.16}$$

$$\tau_\sigma = t_0 B^{-1/b}|\sigma|^{-\gamma} \tag{3.17}$$

where $\sigma = C_\sigma \epsilon$ and t_0 denotes some microscopic time scale [128]. The constants C_σ and B are q- and $|\epsilon|$-independent, and are evaluated from the MCT functional $\mathcal{F}_q(\{f\})$ with the knowledge of the critical nonergodicity parameter f_q^c. Thus, such constants are just system-dependent. The time scales t_σ and τ_σ are usually known as the time scales of, respectively, the β- and α-process.

According to MCT the dynamics slows down by approaching T_c from above, since the time scales diverge at $T = T_c$ with a power law dependence. The dynamics around the plateau, with $|\phi(q,t) - f_{\phi q}^c| \ll 1$, is referred to as the β-process. The height of the plateau is given by the critical nonergodicity paramater $f_{\phi q}^c = \phi(q, t \to \infty)$ of the correlator $\phi(q,t)$ and can be determined from the corresponding MCT-functional solving an equation analogous to Eq. (3.12). MCT predicts that for $T \to T_c^+$ the correlator $\phi(q,t)$ follows the asymptotic law:

$$\phi(q,t) \approx f_{\phi q}^c + h_q G(t) \tag{3.18}$$

with $G(t) = \sqrt{|\sigma|} g(t/t_\sigma)$.

Eq. (3.18) is called the **factorization theorem** or **first universality**. It means that deviations from $f_{\phi q}^c$ at intermediate times factorize in a q-dependent term and a t-dependent term. The function $g(t/t_\sigma)$ gives the whole temperature (through t_σ) and time dependence of $\phi(q,t)$ in the β-relaxation regime and it is referred to as the β-correlator. Since it is independent of the wave vector q, g is identical for all the correlators. The dependence on q and on the specific correlator enters only via $f_{\phi q}^c$ and the critical amplitude h_q. The function $G(t)$ is found to obey the equation:

$$\sigma - z^2 \tilde{G}^2(z) = \lambda z L[G^2(t)], \tag{3.19}$$

where $\tilde{G}(z)$ and $L[G^2(t)]$ are the Laplace transform of respectively $G(t)$ and $G^2(t)$. In this equation $\sigma = c|\epsilon|$, with c a constant (see [121] for its explicit expression), and λ is so-called exponent parameter of the theory given by

$$\lambda = \sum_{qk} e_q^{\mathrm{T}} C^{\mathrm{c}}(q, k, |\mathbf{q} - \mathbf{k}|) e_k e_{|\mathbf{q}-\mathbf{k}|}. \tag{3.20}$$

The quantities e_q and e_q^{T} are respectively the eigenvectors of the so-called stability matrix $\mathbf{C}^{\mathrm{c}}$ (see below) and its traspose, with the normalization conditions $\sum_q e_q^{\mathrm{T}} e_q = 1$

and $\sum_q e_q^{\mathrm{T}}(1-f_q^{\mathrm{c}})e_q^2 = 1$. The elements of the stability matrix are given by

$$(\mathbf{C}^{\mathrm{c}})_{q,k} = (1-f_k^{\mathrm{c}})^2 \left(\frac{\partial \mathcal{F}_q}{\partial f_k}\right)_{\{f=f^{\mathrm{c}}\}} . \tag{3.21}$$

The terms $C^{\mathrm{c}}(q,k,|\mathbf{q}-\mathbf{k}|)$ in Eq. (3.20) are given by:

$$\begin{aligned} &C^{\mathrm{c}}(q,k,|\mathbf{q}-\mathbf{k}|) = \\ &\frac{1}{2}(1-f_k^{\mathrm{c}})^2(1-f_{|\mathbf{q}-\mathbf{k}|}^{\mathrm{c}})^2 \left(\frac{\partial^2 \mathcal{F}_q}{\partial f_k \partial f_{|\mathbf{q}-\mathbf{k}|}}\right)_{\{f=f^{\mathrm{c}}\}} . \end{aligned} \tag{3.22}$$

Eq. (3.19) for the β-correlator does not have an analytical solution. However it can be shown that it has the following asymptotic forms:

$$g(t/t_\sigma) = \left(\frac{t}{t_\sigma}\right)^{-a} \qquad \text{for} \quad t \ll t_\sigma . \tag{3.23}$$

This functional form is called 'critical decay'. For times much longer than t_σ we have:

$$g(t/t_\sigma) = -B\left(\frac{t}{t_\sigma}\right)^{b} \qquad \text{for} \quad t_\sigma \ll t \ll \tau_\sigma . \tag{3.24}$$

This functional form is called 'von Schweidler law'.

The results discussed so far concerned the β-relaxation, i.e. the dynamics of the system on the time scale around the plateau. We turn now our attention to the α-relaxation, i.e. the time scale on which the correlators fall below the plateau. MCT predicts that in this regime the so-called 'time-temperature superposition principle' (TTSP) or **second universality** holds. This means that the correlator $\phi(q,t)$ at temperature T can be written as :

$$\phi(q,t,T) = \widetilde{\phi}(q,t/\tau_\sigma) \tag{3.25}$$

where $\widetilde{\phi}$ is a T-independent master function that follows as a scaling property of the MCT equations, and the temperature dependence is given by the time τ_σ introduced in Eq. (3.17). The superposition principle implies that the α-relaxation time, defined in this work as the time $\tau_{\phi,x}$ where the correlator $\phi(q,t)$ evaluated at the maximum of the static structure factor takes a value x well below the plateau, is proportional to τ_σ, i.e. it follows the asymptotic power law:

$$\tau_{\phi,x}(T) = C_\phi (T - T_c)^{-\gamma} \tag{3.26}$$

The initial part of the α-process, the von Schweidler regime, is given by the power law expansion:

$$\phi(q,t) = f_q^c - h_q (t/\tau)^b + h_q^{(2)} (t/\tau)^{2b} \tag{3.27}$$

which extends the von Schweidler law Eq. (3.24), including corrections up to next-to-leading order.

The dynamical universal exponents of the theory, a, b, and γ, are univocally related to the so-called exponent parameter $\lambda \leq 1$, through the following relation:

$$\lambda = \frac{\Gamma^2(1-a)}{\Gamma(1-2a)} = \frac{\Gamma^2(1+b)}{\Gamma(1+2b)} \tag{3.28}$$

with Γ the Euler's Gamma function, $\Gamma(x) = \int_0^\infty dy e^{-y} y^{x-1}$ and

$$\gamma = \frac{1}{2a} + \frac{1}{2b} \tag{3.29}$$

The explicit expression of λ is controlled by the static correlations ($S(q)$, $c(q)$) *evaluated at the point of the MCT glass transition* (i.e., at $|\epsilon| = 0$). This means that MCT exponents are q- and $|\epsilon|$-independent, but are *system-dependent*.

Coming back to the master function $\widetilde{\phi}$, its shape is often well described by an empirical Kohlrausch-Williams-Watts (KWW) function:

$$\phi^{KWW}(q,t) = A(q) \exp\left[-\left(\frac{t}{\tau^K(q)} \right)^{\beta(q)} \right] \tag{3.30}$$

Note that the KWW-law does not come out as an analytical solution of the MCT equations. However in the limit $q \to \infty$ of the relaxation time $\tau^K(q)$, MCT predicts that [129]:

$$\tau^K(q \to \infty) \sim q^{-1/b} \tag{3.31}$$

where b is the system-dependent von Schweidler exponent (see above).

3.2 MCT for Nonentangled Polymer Melts

In a recent work [38,39], Chong and co-workers have proposed an extension of the MCT to a fully flexible bead-spring model of polymer systems (corresponding to the case $K_B = 0, K_T = 0$ in our model) in the framework of the site formalism [40,102,130,131]. In this formalism polymer chains are divided into interaction sites (monomers), and the dynamics as well as the static structure (see section 2.1.1 of chapter 2) of the system are characterized by site-site correlation functions.

3.2.1 Collective Structural Dynamics

Collective structural dynamics are described by site-site density correlators

$$F_{ab}(q,t) = \frac{1}{n}\Big\langle \sum_{i,j=1}^{n} \rho_i^a(-\mathbf{q},0)\rho_j^b(\mathbf{q},t)\Big\rangle \qquad (a,b = 1, ...N) \tag{3.32}$$

whose initial values are the site-site static structure factors $S_{ab}(q) = F_{ab}(q, t = 0)$. N and n are respectively the number of monomers per chain and the number of chains in the system.

Following a derivation analogous to the monoatomic case, the Mori-Zwanzig exact equation of motion for $F_{ab}(q,t)$ reads [39]:

$$\ddot{F}_{ab}(q,t) + \sum_{x=1}^{N} q^2 v^2 S^{-1}_{ax}(q) F_{xb}(q,t) + \sum_{x=1}^{N} \int_0^t dt' M_{ax}(q, t-t') \dot{F}_{xb}(q,t') = 0 \tag{3.33}$$

Here $v^2 = k_B T/m$ denotes the monomer thermal velocity and $S^{-1}_{ab}(q)$ denotes the element (a, b) of the inverse of the matrix $S_{ab}(q)$. With the use of the approximations introduced above, the MCT expression for the kernel $M_{ab}(q,t)$ reads:

$$\begin{aligned} M_{ab}(q,t) = \frac{\rho_c v^2}{(2\pi)^3} \sum_{x,y=1}^{N} \int & d\mathbf{k}[(\widehat{\mathbf{q}}\cdot\mathbf{k})^2 c_{ax}(k)c_{by}(k)F_{xy}(k,t)F_{ab}(p,t) \\ & +(\widehat{\mathbf{q}}\cdot\mathbf{k})(\widehat{\mathbf{q}}\cdot\mathbf{p})c_{ax}(k)c_{by}(p)F_{xb}(k,t)F_{ay}(p,t)] \end{aligned} \tag{3.34}$$

in which $\widehat{\mathbf{q}} = \mathbf{q}/q$ and $\mathbf{p} = \mathbf{q} - \mathbf{k}$. $\rho_c = n/V$ is the density of chains.
Equations (3.33) and (3.34) constitute a set of coupled equations for the determination

of the site-site density correlators $F_{ab}(q,t)$, once the static input quantites $S_{ab}(q)$ and $c_{ab}(q)$ are known.

From a computational point of view, however, it is quite demanding to solve this $N \times N$ matrix set of equations, especially in the case of long polymer chains. Indeed, in order to do it more tractable, some approximations have to be introduced in the theory. The key assumption is the replacement of the site-specific intermolecular surroundings of a monomer by an averaged one, while keeping the full intramolecular site dependence. This is the essence of the *equivalent-site approximation* [40, 102], which involves the site-site direct correlation function. Assuming that chain end effects on interchain correlations are small, all sites of polymer chains can be treated equivalently. Another approximation, involving the site-site structure factor $S_{ab}(q)$ is the *ring approximation* [39, 40], which is also needed to further simplify the treatment of the MCT equations. We have already discussed the equivalent site and ring approximation in chapter 2, where we concluded that both approximations, introduced in the MCT equations, are fulfilled to the same degree of agreement with simulation results, in all the investigated systems covering the limits of fully flexible and stiff chains.

With the use of the equivalent-site and ring approximations, we can obtain a more tractable expression for the MCT kernel which does not depend on the site indices (a, b). Indeed, by taking the sum $(1/N)\Sigma_{a,b}$ on Eq. (3.32) we can derive a set of closed MCT equations for the normalized density-density correlator $f(q,t) \equiv F(q,t)/S(q)$, with $F(q,t) = N^{-1}\Sigma_{a,b}F_{ab}(q,t)$ [39]:

$$\ddot{f}(q,t) + \frac{q^2 k_B T}{mS(q)} f(q,t) + \frac{q^2 k_B T}{mS(q)} \int_0^t dt' m(q,t-t')\dot{f}(q,t') = 0 \tag{3.35}$$

$$m(q,t-t') = \int \frac{d^3\mathbf{k}}{(2\pi)^3} \mathcal{V}(\mathbf{q}-\mathbf{k},\mathbf{k}) f(k,t-t') f(|\mathbf{q}-\mathbf{k}|,t-t') \tag{3.36}$$

$$\mathcal{V}(\mathbf{q}-\mathbf{k},\mathbf{k}) = \frac{\rho}{2q^4} S(q)S(k)S(|\mathbf{q}-\mathbf{k}|)\left[\mathbf{q}\cdot\mathbf{k}c(\mathbf{k}) + \mathbf{q}\cdot(\mathbf{q}-\mathbf{k})c(|\mathbf{q}-\mathbf{k}|)\right]^2 \tag{3.37}$$

We note that these equations are formally *identical* to the MCT equations for monoatomic liquids that we discussed above (see Eqs. 3.6-3.8). Polymer-specific effects are accounted through the relation between the direct correlation function $c(q)$ and the static structure factor $S(q)$ given by the PRISM equation, $\rho c(q) = 1/\omega(q) - 1/S(q)$, which is different from the Ornstein-Zernike relation, $\rho c(q) = 1 - 1/S(q)$, for monoatomic liquids.

3.2.2 Self Dynamics

The MCT approximations discussed above, with the use of the equivalent-site approximation, permit also to derive MCT equations of motion for the single-chain site-site density correlator defined by:

$$F^s_{ab}(q,t) = \frac{1}{n}\Big\langle \sum_{i=1}^{n} \rho_i^a(-\mathbf{q},0)\rho_i^b(\mathbf{q},t)\Big\rangle \qquad (a,b=1,.....N) \tag{3.38}$$

For the derivation of the MCT equations for $F^s_{ab}(q,t)$ we refer to [39]. The resulting matrix equation can be summarized as [39]:

$$\ddot{F}^s_{ab}(q,t) + \sum_{x=1}^{N} q^2 v^2 \omega^{-1}_{ax}(q) F^s_{xb}(q,t) + \sum_{x,y=1}^{N} q^2 v^2 \omega^{-1}_{ax}(q) \int_0^t dt' m^s_{xy}(q,t-t')\dot{F}^s_{yb}(q,t') = 0 \tag{3.39}$$

Here the expression of the kernel $m^s_{ab}(q,t-t')$, by using the equivalent-site approximation, reads

$$m^s_{ab}(q,t) = \sum_{x=1}^{N} \omega_{ax}(q) \int \frac{d^3\mathbf{k}}{(2\pi)^3} \mathcal{V}^s(\mathbf{q}-\mathbf{k},\mathbf{k}) F^s_{xb}(k,t) f(|\mathbf{q}-\mathbf{k}|,t), \tag{3.40}$$

with the following expression for the vertex:

$$\mathcal{V}^s(\mathbf{q}-\mathbf{k},\mathbf{k}) = \frac{\rho}{q^4} S(|\mathbf{q}-\mathbf{k}|)[\mathbf{q}\cdot(\mathbf{q}-\mathbf{k})]^2 c(|\mathbf{q}-\mathbf{k}|)^2 \tag{3.41}$$

Equation 3.39 can be solved by providing the static quantities $S(q), c(q)$, $\omega^{-1}_{ab}(q)$ and the density-density correlator $f(q,t)$. Having said this, the self-correlator, introduced as $f_s(q,t) = (nN)^{-1}\sum_{i=1}^{n}\sum_{a=1}^{N}\langle \exp[i\mathbf{q}\cdot(\mathbf{r}_i^a(t) - \mathbf{r}_i^a(0))]\rangle$, is obtained by solving before the matrix equations (3.39)-(3.41) for $F^s_{ab}(q,t)$ and then taking the summation over the diagonal terms $f_s(q,t) = N^{-1}\sum_{a=1}^{N} F^s_{aa}(q,t)$.

3.2.3 Rouse Dynamics

In this section we derive the MCT equations for the Rouse mode correlators (see Ref. [39] for details) introduced in chapter 2. First of all we have to consider how the Rouse correlators $C_{pp'}(t)$ are related to the site-site self density correlators $F^s_{ab}(q,t)$. Since the density fluctuations of a tagged chain at large lenght scales (small q values) are given by $\rho^a_j(\mathbf{q},t) \sim 1 + i\mathbf{q}\cdot\mathbf{r}^a_j(t)$, Rouse correlators can be expressed as linear combinations of $F^s_{ab}(q,t)$ in the limit $q \to 0$. Indeed it can be shown that [39]:

$$\frac{1}{N}\sum_{a,b=1}^{N} P_{ap}F^s_{ab}(q\to 0,t)P_{bp'} = \begin{cases} 1+q^2[C_{00}(t)-A]+O(q^4) & p=p'=0, \\ q^2[C_{0p'}(t)-B_{p'}] & p=p', p'>0, \\ q^2C_{pp'}(t)+O(q^4) & p,p'>0, \end{cases} \tag{3.42}$$

where $A = R_g^2/3$ and $B_p = (1/3\sqrt{2}N^2)\sum_{a,b=1}^{N} n^{-1}\sum_{j=1}^{n}\langle(\mathbf{r}^a_j-\mathbf{r}^b_j)^2\rangle\cos[(b-1/2)p\pi/N]$ Using these relations, MCT equations for Rouse mode correlators can be obtained as the $q \to 0$ limit of eq 3.39:

$$\begin{aligned} \ddot{C}_{pp'}(t) + \frac{k_BT}{mN}\delta_{0p}\delta_{0p'} + \frac{k_{\mathrm{B}}T}{m}\sum_{k=0}^{N-1}E_{pk}C_{kp'}(t) + \\ \frac{k_{\mathrm{B}}T}{m}\sum_{k=0}^{N-1}\int_0^t dt' m_{pk}(t-t')\dot{C}_{kp'}(t') = 0, \end{aligned} \tag{3.43}$$

with $\hat{C}^{-1}_{pp'}(0)$ the inverse matrix of $\hat{C}_{pp'}(0)$, and $E_{pp'} = (1-\delta_{0,p\times p'})\hat{C}^{-1}_{pp'}(0)/N$.

The memory kernel is given by

$$m_{pp'}(t) = (\rho/6\pi^2)\int dk k^4 S(k)c^2(k)\sum_{a,b=1}^{N} P_{ap}F^s_{ab}(k,t)P_{bp'}f(k,t). \tag{3.44}$$

Thus, prior to solve Eq. (3.43), we obtained the density-density correlators $f(q,t)$ and self site-site density correlators $F^s_{ab}(q,t)$ from their respective MCT equations (see above). The static quantities $S(q), c(q), \omega_{ab}(q)$ and $\hat{C}^{-1}_{pp'}(0)$ enter the equations as external inputs.

In their work Chong and co-workers showed that the MCT for polymers dynamics reduces to the Rouse model in the asymptotic limit of large degree of polymerization

$N \rightarrow \infty$ [39]. By performing a Markovian approximation for the memory kernel, and assuming Gaussian chain statistics they obtained the subdiffusive regime for the monomer mean-square displacements Eq. (2.27) and the exponential decay of the Rouse correlators Eq. (2.22). Having noted this, MCT provides a unified and continuous microscopic description of both chain and glassy dynamics, down to time scales around and before the $\alpha-$process. This part of the dynamic window is just 'coarse-grained' in the phenomenological Rouse model.

Chapter 4

MCT vs Simulations: Data Analysis

In Chapter 3 we discussed several universal results which originate from the structure of the MCT equations of motion, in particular from the the fact that the memory kernel is bilinear in the density fluctuations. As mentioned above those predictions where initially derived for hard sphere systems [6, 121, 122]. On the other hand we observed that, following the derivation of Chong and co-workers [39], the MCT equations for polymer melts become formally identical to the ones initially derived for simple liquids. Having said this, the asymptotic scaling laws exposed in chapter 3 will also hold in the MCT for polymer melts. Thus a phenomenological analysis of our simulation data in terms of the MCT is justified. This kind of analysis, based on data fits to the MCT asymptotic laws, is usually performed when numerical solutions of the corresponding MCT equations are not available. It must be noted that the temperature and time intervals where these asymptotic laws can be applied, is *a priori* unknown. There is some freedom in the choice of these intervals and the choice can affect the numerical values of the fit parameters. Thus, a good strategy for the fitting procedure should ensure that the results are free of internal inconsistencies. In the following we will present our strategy based on our experience.

First we present a test of the factorization theorem and of the time temperature superposition principle (TTSP). Then we present a consistent fitting procedure of our simulation data to the MCT asymptotic power laws predicted for the $\alpha-$relaxation regime, in order to obtain information about the critical nonergodicity parameters, the critical temperature T_c and the dynamic exponents of the theory (a, b, γ, λ). We organize our discussion around the density-density and self-density correlators.

4.1 First Universality: Factorization Theorem

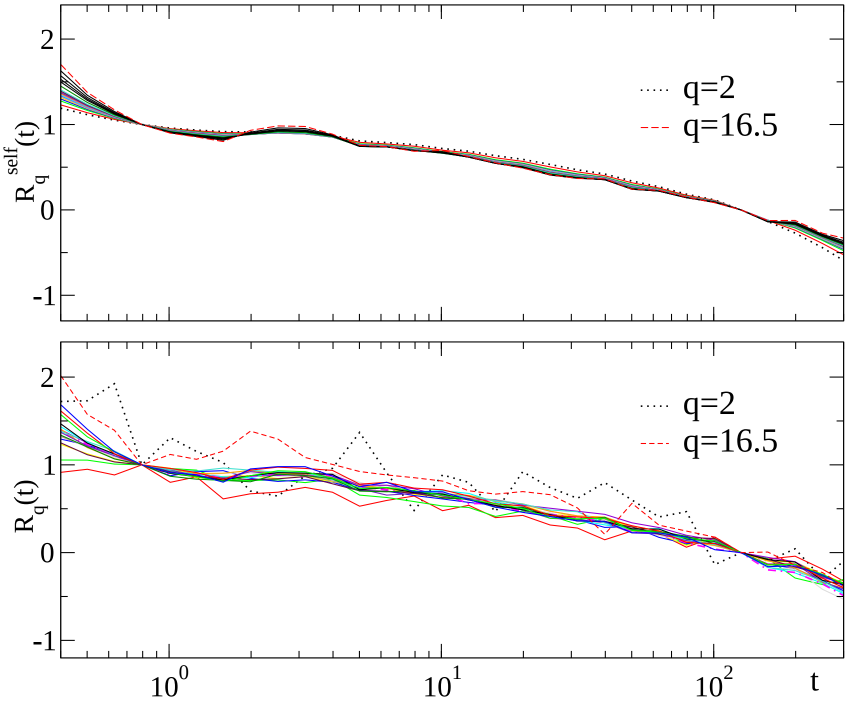

Figure 4.1: Test of the factorization theorem for self- and density-density correlators at T=0.96, $K_{\mathrm{B}} = 25$, and $K_{\mathrm{T}} = 1$ by plotting the time dependence of $R_q(t)$ defined by equation (4.1). Top and bottom panels show results for respectively self- and density-density correlators. In the $\beta-$regime all curves collapse into a single master curve. By definition $R_q(t = t' = 100) = 0$ and $R_q(t = t'' = 0.8) = 1$

In order to test the factorization theorem, Eq.(3.18), we computed the ratio:

$$R_q^{\phi}(t) = \frac{\phi(q,t) - \phi(q,t')}{\phi(q,t'') - \phi(q,t')} = \frac{G(t) - G(t')}{G(t'') - G(t')} \tag{4.1}$$

where $\phi(q,t)$ is an arbitrary density correlator and t' and t'' are arbitrary times in the β-regime (where $|\phi(q,t) - f^c_{\phi q}| \ll 1$). If the factorization property holds, the second equality of Eq. (4.1) also holds, and $R_q^{\phi}(t)$ depends only on the fixed times t' and t'' and on the temperature (via t_σ), but not on the correlator ϕ or on the wave vector q. Thus equation 4.1 will reveal whether the analysis of the observed

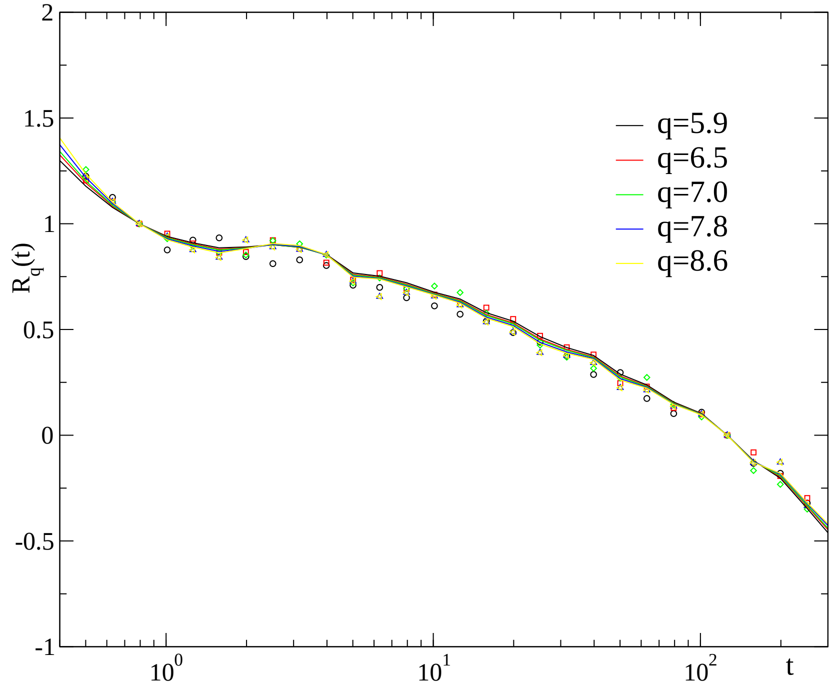

Figure 4.2: Time dependence of $R_q(t)$ for both self- (lines) and density-density (points) correlators, for a few values of the wave vector q. In the $\beta-$regime all curves collapse into a single master curve independently of the correlator.

two step relaxation of simulation data in terms of MCT is justified or not. Since the factorization theorem is predicted to hold close to T_c for small values of the separation paramater $\epsilon = (T - T_c)/T$, we can define a range of temperatures $T_c \lesssim T \lesssim T_{\max}$ where the asymptotic power laws can be applied to fit simulation data. $T_{\max}$ is some high temperature for which the density correlator still exhibits a two step relaxation. Figure 4.1 shows $R_q^\phi(t)$ computed from the density-density and self-density correlators for $K_{\rm B} = 25$ and $K_{\rm T} = 1$ over a range of 20 values of the wave vector q, from 2 to 16.5 and at the lowest temperature investigated $T = 0.96$. The fixed times t'' and t' take the values of 0.8 and 100, corresponding to the beginning and the end of the plateau. We observe that there is an intermediate time window of about two decades where the data for the self and density-density correlator collapse onto a q-independent master-curve, while they split at both short and late times. Figure 4.2 demonstrates that the master curve is, moreover, the same for both correlators.

4.2 Second Universality: TTSP

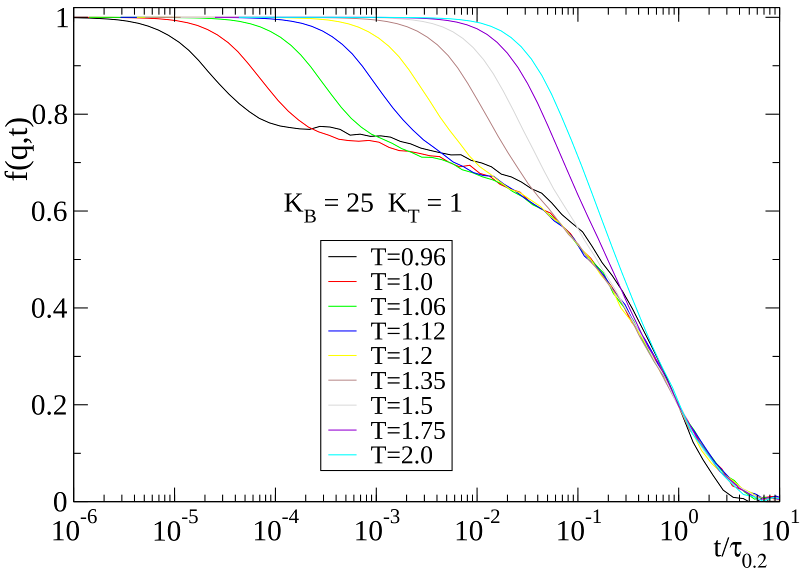

Figure 4.3: Test of the time-temperature superposition principle for the density-density correlators at $q_{\mathrm{max}} \approx 7$, for the case $K_{\mathrm{B}} = 25$, and $K_{\mathrm{T}} = 1$. In the α-regime all curves collapse into a single master curve.

Figure 4.3 shows a test of the TTSP for the density-density correlators evaluated at q_{max} (maximum of the static structure factor $S(q)$), for the case $K_{\mathrm{B}} = 25$, $K_{\mathrm{T}} = 1$. The rescaling time is the $\alpha-$relaxation time $\tau_{0.2}$ defined in chapter 2. The TTSP breaks down in the proximity of T_c and for $T < T_c$. Indeed we find deviations from the TTSP at $T = 0.96$. Within the framework of MCT, these deviations at low T from the ideal behaviour are connected with the presence of additional relaxation mechanisms ignored by the ideal MCT, the so-called ‘hopping processes‘, which become dominant on approaching T_c from above, and restore ergodicity below T_c. Thus the TTSP breaks down in the proximity of T_c, whose value will be determined in the next section, while equation 4.1 still holds. Thus the TTSP allows us to determine the lowest temperature T_{min} for which ideal MCT can be applied. In the following we will focus our data analysis on the lowest temperature simulated for which the TTSP holds.

4.3 MCT Asymptotic Power Laws: Simulation Data Analysis

In this section, density correlators and relaxation times, computed from our simulation data, will be analyzed within the framework of MCT.

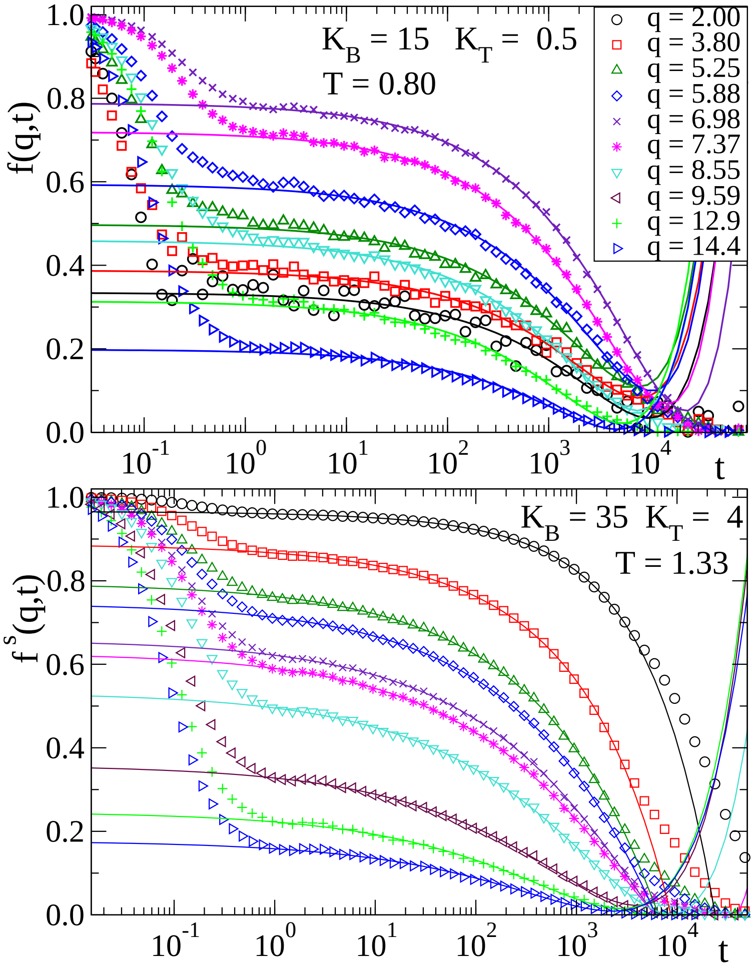

Figure 4.4: Symbols: simulation results for density correlators. Top panel: $f(q,t)$ for $(K_\mathrm{B}, K_\mathrm{T}) = (15, 0.5)$, at $T = 0.80$. Bottom panel: $f^\mathrm{s}(q,t)$ for $(K_\mathrm{B}, K_\mathrm{T}) = (35, 4)$, at $T = 1.33$. Identical symbols in both panels correspond to identical wave vectors q [values are given in the top panel]. Lines are fits to the von Schweidler expansion, Eq. (3.27) (up to second-order terms), with $b = 0.50$ (top) and 0.37 (bottom).

Consistency of the analysis requires that dynamic correlators and relaxation times are described by a common set of exponents, univocally related through Eqs. (3.28, 3.29). This consistency test has been done for all the systems here investigated, with different strength of the intramolecular barriers. Figs. 4.4, 4.6 and 4.7 display some representative examples. Fig. 4.4 shows for a broad q-range, fits to Eq. (3.27) of density correlators for the state points $K_{\mathrm{B}} = 15$, $K_{\mathrm{T}} = 0.5$, $T = 0.80$ (S1) and $K_{\mathrm{B}} = 35$, $K_{\mathrm{T}} = 4$, $T = 1.33$ (S2). A good description is achieved, for all the q-values and over several time decades, with a fixed b-exponent ($b = 0.50$ and 0.37 for respectively S1 and S2). Fig. 4.5 displays, for the former barrier strength, the q-dependence of the critical non-ergodicity parameters. The fully flexible case $K_{\mathrm{B}} = K_{\mathrm{T}} = 0$ is also included. As deduced from the stronger decay of f_q^c and f_q^{sc} for stronger barriers, chain stiffness induces a weaker localization at fixed density. By making an approximate fit of f_q^{sc} to Gaussian behavior, $\exp(-q^2 l_c^2/6)$, we estimate, a localization length $l_c = 0.19$, 0.21, and 0.23 for respectively $(K_{\mathrm{B}}, K_{\mathrm{T}}) =$ (0,0), (15,0.5), and (35,4).

Data of self-correlators from the plateau to the limit of the simulation window have been fitted to KWW functions, Eq. (3.30). Fig. 4.6 shows the q-dependence of the so-obtained KWW relaxation times τ_q^{K} for the former values of the barrier strength, at their respective lowest investigated temperatures. The lines represent tests of the MCT prediction $\tau_q^{\mathrm{K}} \propto q^{-1/b}$ for large q. A good description of the data is obtained with the same b-exponents used for the independently obtained von Schweidler fits of Fig. 4.4.

The increase of the barrier strength also induces a higher critical temperature T_c, and a longer relaxation time for fixed T. This is demonstrated in Fig. 4.7. The latter shows, for the same values of $(K_{\mathrm{B}}, K_{\mathrm{T}})$ in Fig. 4.6, a test of the power law $\tau_{0.2} \propto (T - T_c)^{-\gamma}$ for the temperature dependence of the estimated α-relaxation times. The fit covers about three time decades. By representing the data in terms of the separation parameter $\epsilon_T = T/T_c - 1$, clearly different γ-exponents are evidenced for different barrier strength. A good description of the data is obtained with the γ-values derived, through Eqs. (3.28, 3.29), from the b-values used in Figs. 4.4 and 4.6. This result demonstrates the consistency of the MCT analysis for the representative examples showed here, which cover all the range of investigated barrier strength between fully-flexible and stiff chains.

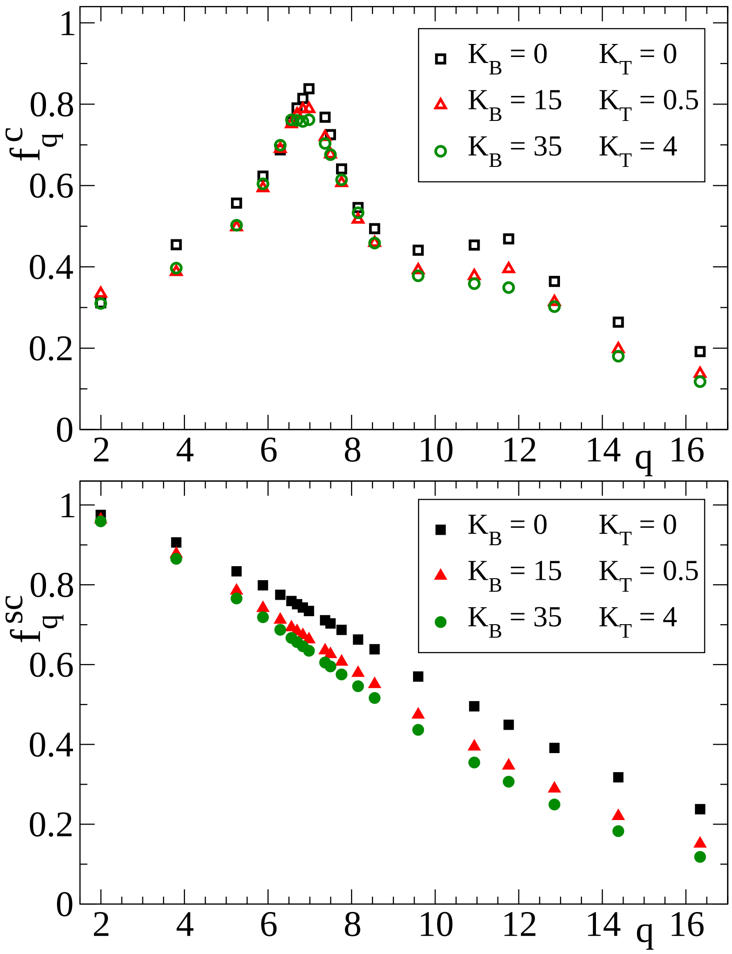

Figure 4.5: Critical nonergodicity parameters, as determined from fits to Eq. 3.27, for different barrier strength. Top and bottom panels show data for respectively f_q^c and f_q^{sc}.

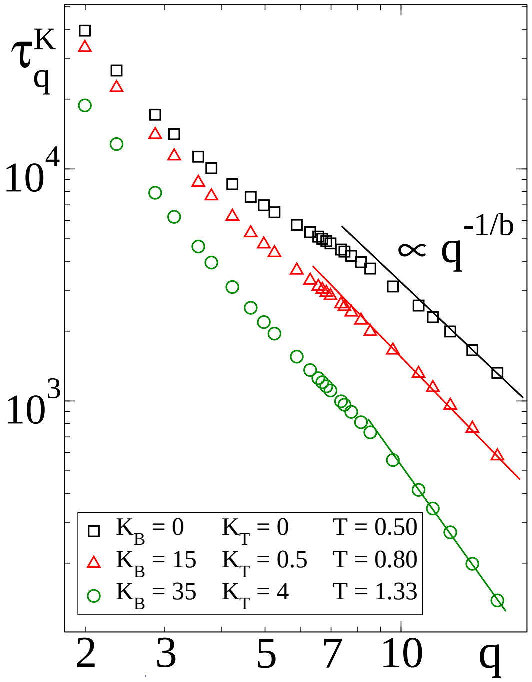

Figure 4.6: Symbols: q-dependence of KWW relaxation times for different barrier strength. Lines are fits to $\propto q^{-1/b}$ (see section 3.1). From top to bottom $b = 0.54$, 0.50 and 0.37.

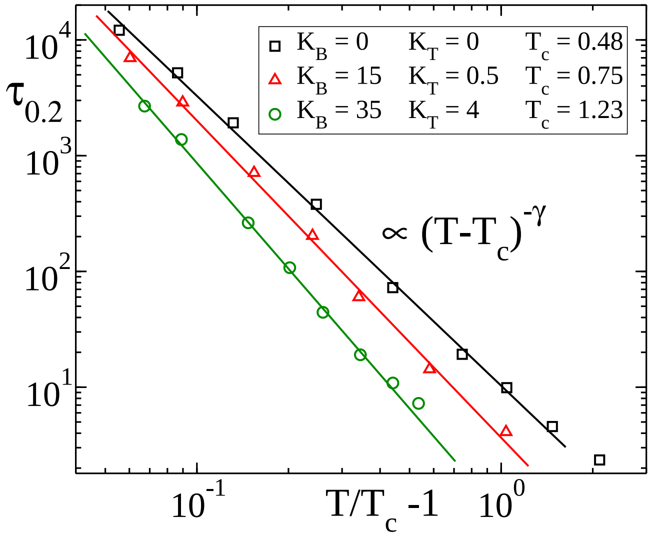

Figure 4.7: Symbols: T-dependence of relaxation times $\tau_{0.2}$ for different barrier strength. Lines are fits to $\propto (T - T_c)^{-\gamma}$ (see section 3.1). From top to bottom $\gamma = 2.60$, 2.74 and 3.43.

ρ	K_{B}	K_{T}	C_{10}^{rc}	T_c	a	b	γ	λ
1	0	0	1.3	0.48	0.299	0.54	2.60	0.761
1	4	0.1	2.0	0.54	0.296	0.53	2.63	0.767
1	8	0.2	2.3	0.67	0.293	0.52	2.67	0.773
1	15	0.5	2.8	0.75	0.287	0.50	2.74	0.785
1	25	1	3.2	0.82	0.263	0.43	3.06	0.827
1	25	4	4.2	1.02	0.251	0.40	3.24	0.845
1	35	4	4.4	1.23	0.240	0.37	3.43	0.862

Table 4.1: Values of the MCT exponents and critical temperature T_c for different barrier strength. Also included are the values of the characteristic ratio C_{10}^{rc} at T_c.

System	a	b	γ	λ
Hard spheres	0.31	0.58	2.5	0.74
Orthoterphenyl	0.30	0.54	2.6	0.76
Polyethylene (UA)	0.27	0.46	2.9	0.81
Poly(vinyl methyl ether) (FA)	0.23	0.35	3.6	0.87
1,4-Polybutadiene (UA)	0.21	0.30	4.1	0.90
1,4-Polybutadiene (FA)	0.18	0.24	4.9	0.93
Poly(vinyl ethylene) (FA)	0.18	0.24	4.9	0.93

Table 4.2: MCT exponents for different glass-formers. Data are taken from [42–44] and references therein. UA and FA denote respectively coarse-grained united atom and fully-atomistic models.

Table 4.1 displays the results of the MCT analysis (dynamic exponents and T_c) for all the investigated cases. It also includes the characteristic ratio at T_c, C_{10}^{rc}, as computed from the simulations. As already discussed in chapter 1, C_{10}^{rc} provides a quantitative characterization of chain stiffness. From numerical values in Table 4.1 a clear correlation between the exponent parameter λ and chain stiffness is unambiguously demonstrated. The competition between packing effects and intramolecular barriers induces a progressive increase of λ from the value $\lambda = 0.761$ for fully-flexible chains to $\lambda = 0.862$ for the stiffest investigated chains.

This observation rationalizes the large difference observed between MCT exponents for fully-flexible bead-spring chains and chemically realistic polymers. Table 4.2 shows a representative compilation of exponents for glass-formers of very different nature.

Exponents for fully-flexible bead-spring chains are similar to those of non-polymeric glass-formers, including the hard-sphere fluid, i.e., the archetype glass-former dominated by packing effects. Chemically realistic polymers of increasing complexity exhibit instead values approaching the limit $\lambda = 1$ characteristic of higher-order MCT transitions. The latter, or more generally transitions with $\lambda \simeq 1$, arise in systems with different competing mechanisms for dynamic arrest. These systems include short-ranged attractive colloids [46–48] in which the competing mechanisms are short-range attraction and hard-sphere repulsion or binary mixtures with strong dynamic asymmetry [17, 18, 49, 50] in which the mechanisms are bulk-like caging and confinement. The systematic study presented here strongly suggests a competition between general packing effects and polymer-specific intramolecular barriers as the origin of the mentioned difference between fully flexible bead-spring chains and real polymers.

In this chapter we have analyzed the simulation results within the framework of MCT. In the next chapter the observed phenomenological trends are compared with numerical solutions of the MCT equations of nonentangled polymer melts.

Chapter 5

MCT vs Simulations: Numerical Solutions

5.1 Structural Relaxation

The long-time coherent and self dynamics of the system are determined by solving the equations (3.35) and (3.39), provided the static quantities are given as initial inputs. By taking the long-time limit of Eq (3.35) we obtain an implicit equation for the nonergodicity parameter $f_q = \lim_{t\to\infty} f(q,t)$,

$$\frac{f_q}{1-f_q} = \int \frac{d^3\mathbf{k}}{(2\pi)^3} \mathcal{V}(\mathbf{q}-\mathbf{k},\mathbf{k}) f_{|\mathbf{q}-\mathbf{k}|} f_k = \mathcal{F}_q(\{f\}) \tag{5.1}$$

Let us remind that by approaching the MCT transition point at T_c from above, the solution of Eq. (5.1) jumps from $f_q = 0$ to a finite value f_q^c named the critical nonergodicity parameter.

Analogously, by taking the long-time limit in Eq. (3.39), we obtain a $N \times N$-matrix equation for the single-chain site-site nonergodicity parameters $f^s_{ab}(q) = \lim_{t\to\infty} F^s_{ab}(q,t)$,

$$f^s_{ab}(q) = \sum_{x,y=1}^{N} \mathcal{F}^s_{ax}(q)[\mathbf{I} + \mathcal{F}^s_q]^{-1}_{xy} \omega_{yb}(q) \tag{5.2}$$

with the following expression for the MCT functional $\mathcal{F}^s_{ab}(q)$:

$$\mathcal{F}^s_{ab}(q) = \sum_{x=1}^{N} \omega_{ax}(q) \int \frac{d\mathbf{k}}{(2\pi)^3} \mathcal{V}^s(\mathbf{q}-\mathbf{k},\mathbf{k}) f^s_{xb}(k) f(|\mathbf{q}-\mathbf{k}|) \tag{5.3}$$

The self nonergodicity parameters, defined as the long time limit of $f_q^s(q,t)$, can be obtained by solving Eqs. (5.2) and taking the summation over the diagonal terms, $f_q^s = N^{-1}\sum_{a=1}^{N} f_{aa}^s(q)$. We solved Eqs. (5.1-5.2) for our systems. The three-dimensional integrals over $\mathbf{k}$ appearing in these equations are transformed to bipolar coordinates. Due to the isotropy of the system a rotation around the $\mathbf{q}$-vector can be integrated out, and we can transform $d\mathbf{k} \rightarrow 2\pi\rho d\rho dz$ where ρ and z are the projections of $\mathbf{k}$ onto and orthogonal to $\mathbf{q}$ respectively. From these variables we transform further to $k = |\mathbf{k}|$ and $p = |\mathbf{q}-\mathbf{k}|$. Noting that $\rho|\partial(\rho z)/\partial(kp)| = (kp/q)$, we finally obtain:

$$\int \frac{d^3\mathbf{k}}{(2\pi)^3} \equiv \frac{1}{q}\int \frac{kdk}{2\pi}\frac{pdp}{2\pi}, \tag{5.4}$$

with both integrals on the right-hand side over $[0,\infty[$ and with the restriction $p \in [|q-k|, q+k]$. These integrals are discretised to an equidistant grid of $M = 600$ points with grid spacing $\Delta q = 0.1$ and evaluated as Riemann sums [121, 122]. Using the following relations

$$\mathbf{q}\cdot\mathbf{k} = (q^2+k^2-p^2)/2 \tag{5.5}$$

$$\mathbf{q}\cdot\mathbf{p} = (q^2+p^2-k^2)/2 \tag{5.6}$$

we obtain the discretised expression for the right-side of Eq. (5.1). This equation now reads:

$$\begin{aligned}\frac{f_q}{1-f_q} = \frac{\rho(\Delta q)^3}{32\pi^2}\sum_{x_k}\sideset{}{'}\sum_{x_p}\frac{x_k x_p}{x_q^5}S(q)S(k)S(p)\\ \times[(x_q^2+x_k^2-x_p^2)c(k)+(x_q^2+x_p^2-x_k^2)c(p)]^2 f_k f_p\end{aligned} \tag{5.7}$$

Here $q = \Delta q x_q$, $k = \Delta q x_k$, $p = \Delta q x_p$ and $x_q, x_k, x_p = 1/2, 3/2, ..., 1199/2$. The prime at the sum means that the summation is restricted to $x_p \in [|x_q-x_k|+1/2, x_q+x_k-1/2]$. The solutions were found by a standard iterative procedure $f_q^{j+1} = [1-f_q^j]\mathcal{F}_q(\{f^j\})$, with j the iteration step and with the initial condition $f_q^0 = 1$. It can be demonstrated that the stability matrix in Eq. (3.21) has always a maximum non-degenerate eigenvalue $E \leq 1$, which takes the upper value $E_\mathrm{c} = 1$ at the critical point [121]. Thus, by following the drift of E with changing temperature it is possible to bracket the values of the critical nonergodicity parameters f_q^c, and the critical temperature T_c, with very high precision. Once the values of f_q^c are obtained, the exponet paramater λ can be evaluated throug equation 3.20. The corresponding discretised expression for the self MCT functional in Eq. (5.3) can be obtained by following the same arguments and reads as:

$$\mathcal{F}^s_{ab}(q) = \frac{\rho(\Delta q)^3}{16\pi^2} \sum_{x=1}^{N} \omega_{ax}(q) \sum_{x_k} \sideset{}{'}\sum_{x_p} \frac{x_k x_p}{x_q^5} S(p)[(x_q^2 + x_p^2 - x_k^2)c(p)]^2 f^s_{xb}(k) f_p \tag{5.8}$$

The site-site nonergodicity parameters $f^s_{ab}(q)$ can be found by the same standard iterative procedure, provided the static quantities ($S(q)$, $c(q)$, $\omega_{ab}(q)$) and the coherent nonergodicity parameters f_q are given.

Following the procedure exposed above, we solved Eq. (5.7) by inserting as external inputs the structural quantities, $S(q)$ and $c(q)$, as directly computed from the simulations. However, as previously reported in Ref. [39] for fully-flexible chains, a MCT transition was not observed for any of the investigated barrier strength. This means that the theoretical critical temperature T_c lies below the lowest simulation temperature for which equilibration was possible. This result is different from the usual observation in non-polymeric systems, for which the theoretical critical point is accessible in simulation time scales. The reason of this difference is, in some way, related with the unability to crystallize of bead-spring models, which avoids a fast growing of peaks under cooling in the static structure factor $S(q)$, leading to MCT kernels which are not sufficiently strong to provide nonzero solutions of f_q.

Since static correlations computed from our equilibrium simulations do not induce a MCT transition, we are forced to use a structural theory for estimating $S(q)$ and $c(q)$ at lower temperatures, which will allow us to insert them in the MCT equations and to search for the critical temperature. Thus, we solve numerically the PRISM equation

$$\rho c(q) = 1/\omega(q) - 1/S(q), \tag{5.9}$$

with the Percus-Yevick (PY) closure relation [105] for the non-bonded potential $V(r)$ of Eq. (1.6). The PY relation is given by:

$$c(r) = [1 - \exp(V(r)/k_B T)](h(r) + 1), \tag{5.10}$$

The PY relation is most successful in describing the packing structure induced by interaction potentials of short-range and with a quickly divergent core [105]. Such potentials include hard sphere-like repulsions or soft-sphere potentials $\sim r^{-n}$ with n larger than about 10, as the one used in this work for monomer-monomer interactions, Eq. (1.6). The coupled set of nonlinear equations (5.9) and (5.10) can be solved by the Picard iteration method for the function $\Gamma(r) = h(r) - c(r)$. The reason why we work with $\Gamma(r)$ instead of $c(r)$ or $h(r)$ is that $\Gamma(r)$ is a smooth function over all the range of r, in contrast to $c(r)$ and $h(r)$, which exhibit strong rises and drops over a narrow range of r when entering the core of the potential $V(r)$ [105]. We solved equation (5.9) in the reciprocal q-space and equation (5.10) in the real r-space. We used fast Fourier tranforms to switch back and forth between the r- and q-space representation of the functions. The functions $h(r)$, $c(r)$ and $\Gamma(r)$ were discretized on a grid of $G_r = 6000$ points from $r = 0$ to $r_{max} = 40$ with a grid spacing $\delta r = r_{max}/G_r$. Their Fourier transformed quantities where discretized on a grid of $G_q = 800$ points from $q = 0$ to $q_{max} = 65$ with a grid spacing $\delta q = \pi/r_{max}$. We used the following criterion for convergence of the Picard iteration:

$$Err = \left[\frac{1}{G_r}\sum_{i=1}^{G_r}(\Gamma(r_i)^{(j+1)} - \Gamma(r_i)^{(j)})^2\right]^{1/2} < 10^{-7} \tag{5.11}$$

To achieve convergence, the iteration was performed by mixing the old solution $\Gamma^{(j)}$ with the current solution Γ in order to obtain the new solution $\Gamma^{(j+1)}$,

$$\Gamma^{(j+1)} = \alpha\Gamma + (1-\alpha)\Gamma^{(j)} \tag{5.12}$$

where α is a real number between 0 and 1 ($\alpha = 0.2$ in this work).

The form factor $\omega(q)$ in Eq. (5.9) is an *external* input in the PRISM theory. Since we have observed in Chapter 2 that $\omega(q)$ shows a very weak temperature dependence in comparison to the global static structure factor $S(q)$, we just used, for each system, the $\omega(q)$ of the lowest temperature simulated.

In figure 5.1 we show a comparison of the critical nonergodicity parameters f_q^c (top panel) and f_q^{sc} (bottom panel) as obtained from numerical solution of the MCT equations, with the results of the fitting procedure of simulation data . The theoretical results qualitatively reproduce the simulation trends, and in particular the observation that at fixed density the intramolecular barriers induce a weaker localization length. Quantitatively, the MCT solutions overestimate the amplitude of the nonergodicity parameters, except in the low-q region of f_q^{c}, for which MCT clearly understimates the results.

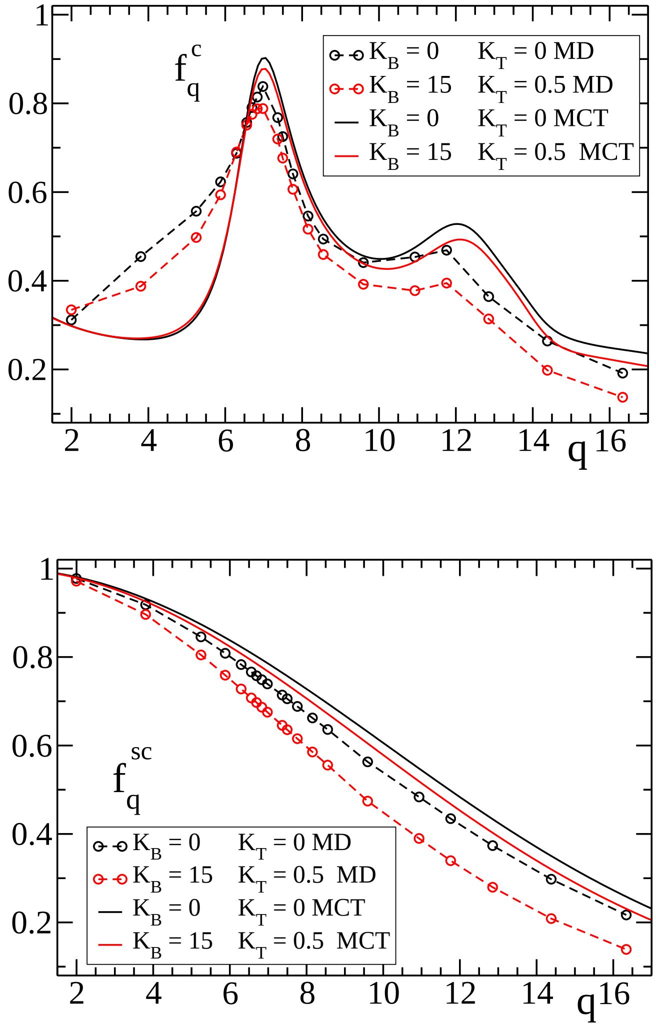

Figure 5.1: Comparison of the critical nonergodicity parameters f_q^c and f_q^{sc} obtained from MCT calculations (solid lines) with those obtained from the MCT analysis of the simulation data (symbols, dashed lines are guides for the eyes). Results are shown both for fully flexible chains and for representative stiff chains.

In Fig. 5.2 we show a representation of the critical temperature T_{c} and the exponent parameter λ as a function of the characteristic ratio C_{10}^{rc}, which quantifies chain stiffness. Superscripts 'MD' and 'MCT' are used respectively for simulation and theoretical values. A clear correlation between the barrier strength and the values of T_c^{MD} and λ^{MD} is unambiguously demonstrated (see section 4.3). The interplay between monomer packing effects and intramolecular barriers induces a progressive increase of T_c^{MD}. This trend is well reproduced by the theory for low and moderate values of the internal barriers. Thus, for values of bending and torsional constants $K_{\mathrm{B}} < 15$ and $K_{\mathrm{T}} < 0.5$, the dependence of T_c^{MCT} on C_{10}^{rc} roughly displays the same slope as for T_c^{MD}, with a shift factor $T_c^{\mathrm{MD}}/T_c^{\mathrm{MCT}} \approx 1.25$. Similar shifts between simulation and theory, which have their origin in the mean-field character of the MCT [6], are observed in other systems [48, 132, 133]. The range of barrier strength for which T_c^{MCT} and T_c^{MD} are roughly parallel is significant. Indeed, for $(K_{\mathrm{B}}, K_{\mathrm{T}}) = (8, 0.2)$ the characteristic ratio C_{10}^{rc} is a 70% larger than for fully-flexible chains. However, a strong discrepancy between simulation and theory becomes evident on increasing the barrier strength from $(K_{\mathrm{B}}, K_{\mathrm{T}}) = (15, 0.5)$. While beyond this point T_c^{MCT} seems to approach an asymptotic limit, T_c^{MD} increases up to 1.23 for the stiffest investigated chains.

Similar trends are observed for the λ-exponent. Simulation values increase from $\lambda^{\mathrm{MD}} = 0.76$ for fully-flexible chains to $\lambda^{\mathrm{MD}} = 0.86$ for the stiffest investigated chains. The first ones are typical of simple glass-formers as the archetype hard-sphere fluid ($\lambda = 0.74$ [121]), where dynamic arrest is driven by packing effects. The largest ones are similar to those observed in realistic models of polymer melts which incorporate the full chemical structure of the chains [42–44] (see tables 4.1-4.2). On the contrary, the theoretical exponent exhibits a very weak variation, $0.71 \leq \lambda^{\mathrm{MCT}} \leq 0.72$, over the investigated range of barrier strength. These discrepancies in the case of strong intramolecular barriers are also reflected in the q-dependence of density correlators computed from simulations and from solution of the MCT equations eq. 3.35 and eq. 3.39. See Appendix B for numerical details. In both cases we fitted the corresponding α-decay to a KWW function. Fig. 5.3 compares the q-dependence, at fixed T, of the KWW time τ_q^{K} for the self-correlators $f^{\mathrm{s}}(q,t)$, as obtained from simulations and from theory. Results are presented for the fully-flexible case and for the stiffest investigated chains.

Before discussing such results, some points must be clarified. As mentioned above, the mean-field character of MCT usually yields a temperature shift between simulation and theory (see Fig. 5.2a). Moreover, MCT times are affected by an undetermined constant factor [6, 128]. Thus, a proper comparison between theory and simulation for time-dependent correlators can be done by rescaling t by some characteristic relaxation time, and using a common separation parameter $\epsilon_T = (T - T_c)/T_c$ [39]. This is the case for the data of Fig. 5.3. Thus, each data set is rescaled by the respective KWW time

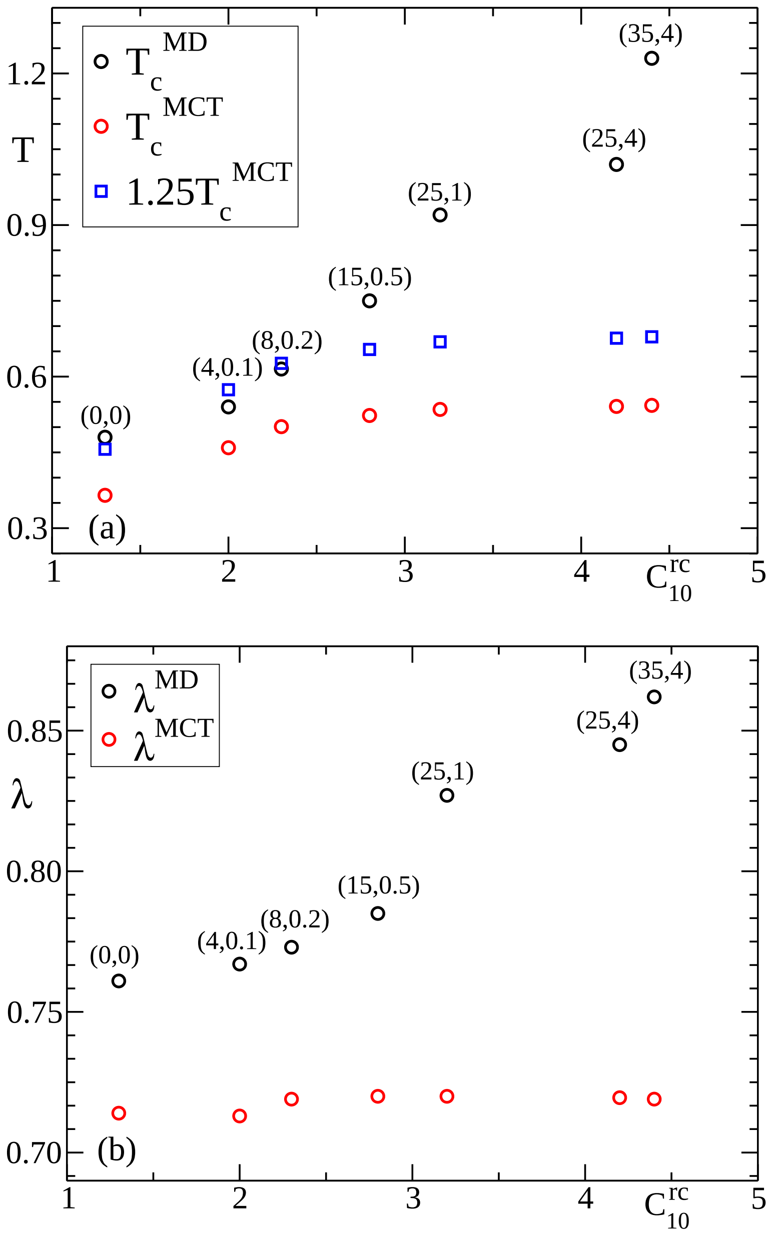

Figure 5.2: Critical temperature T_c (a) and λ-exponent (b) as a function of the characteristic ratio C_{10}^{rc} (measured at T_c^{MD}). The theoretical values T_c^{MCT} and λ^{MCT} are compared with the simulation values T_c^{MD} and λ^{MD} (see text). The respective values of the bending and torsional strength $(K_\mathrm{B}, K_\mathrm{T})$ are indicated on top of each symbol for T_c^{MD} in (a) and for λ^{MD} in (b).

$\tau_{q_{\max}}$ corresponding to $f^s(q_{\max}, t)$. Temperatures of both panels correspond to $\epsilon_T \approx 0.04$ and 0.08 for respectively fully-flexible and stiff chains. In the rest of the memory we will present several comparisons between simulation data and MCT solutions for dynamic observables. It will be understood that the times and temperatures of the compared data obey the former criteria.

A clear disagreement between simulation and theoretical trends becomes evident in Fig. 5.3. The two sets of KWW times obtained from simulations show a rather different q-dependence for $q > q_{max}$, which is more pronounced for the stiff chains. On the contrary, after rescaling by $\tau_{q_{\max}}$, the theoretical sets become essentially identical. In the low $q < q_{max}$ range, simulation data do not show the crossover to the hydrodynamic limit $\tau_q \sim q^{-2}$ The slope at $q \approx 2$ is consistent with exponents greater than 2.5. We remind that the asymptote $\tau_q \sim q^{-2}$ is a manifestation of the ultimate diffusive regime $\langle \Delta r^2(t) \rangle \sim t$. As discussed in the chapter 2 polymer systems exhibit, as a consequence of chain connectivity and even if they are non-entangled, subdiffusive dynamics over several time decades between the α-time scale and the final onset of diffusion. This is not the case, within a limited simulation time window, at temperatures close to T_c as those of Fig. 5.3. Thus, the low-q behavior in this figure actually reflects the beginning of the subdiffusive regime in the MSD (see fig. 2.7).

Fig 5.4 shows a similar comparison between simulation and theory for the rescaled KWW times of the density-density correlators, $f(q,t)$. For $q \geq q_{\max}$ the theory reproduces qualitatively the shape of the relaxation times, which are modulated by the respective static structure factor $S(q)$. However, MCT fails at reproducing the broad peak at intermediate $q_{\mathrm{C}} \approx 4$ which is present in the simulation data. This failure was already noted for fully-flexible chains in Ref. [39], and is confirmed here for the general case with intramolecular barriers. Apparently (note the error bars), the peak does not shift significantly and decreases its intensity as chains become stiffer, leading to a shoulder. In previous works [101] on similar fully-flexible bead-spring chains of $N = 10$, the value of q_{C} has been identified with $2\pi/R_{\mathrm{g}}$, where R_{g} is the chain radius of gyration. Data of Fig. 5.4a do not seem compatible with this assignment. Apart from results for fully-flexible and stiffest investigated chains of $N = 10$, we include data for $(K_{\mathrm{B}}, K_{\mathrm{T}}) = (15, 0.5)$ of additional simulations with $N = 21$. With this, the data sets of Fig. 5.4a cover a significant variation in R_{g}. Namely, for $(K_{\mathrm{B}}, K_{\mathrm{T}}) = (0, 0)$, (35,4), and (15,0.5) we respectively find $2\pi/R_{\mathrm{g}} = 4.2$, 2.8, and 2.0. Thus, the observation $q_{\mathrm{C}} \approx 2\pi/R_{\mathrm{g}}$ for fully-flexible chains is apparently fortuitous. The associated length scale $2\pi/q_C \approx 1.6\sigma$ rather seems to be a characteristic feature which does not depend significantly on the barrier strength. We will come back to these points in the next chapter.

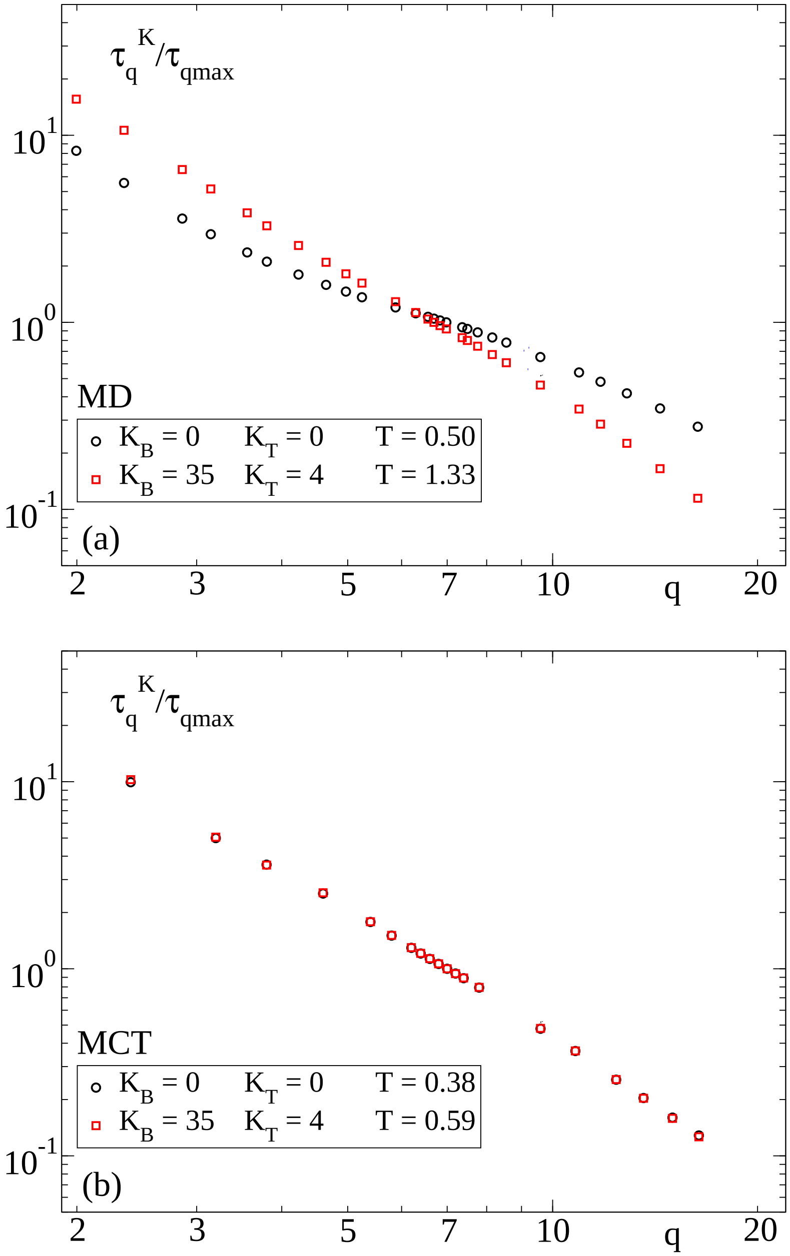

Figure 5.3: For fully-flexible and stiffest investigated chains, q-dependence of the KWW times for self-density correlators $f^s(q,t)$. Data are rescaled by the respective KWW times at $q_{\max}$. Data in panels (a) and (b) correspond respectively to simulation results and MCT solutions at selected temperatures (see legend).

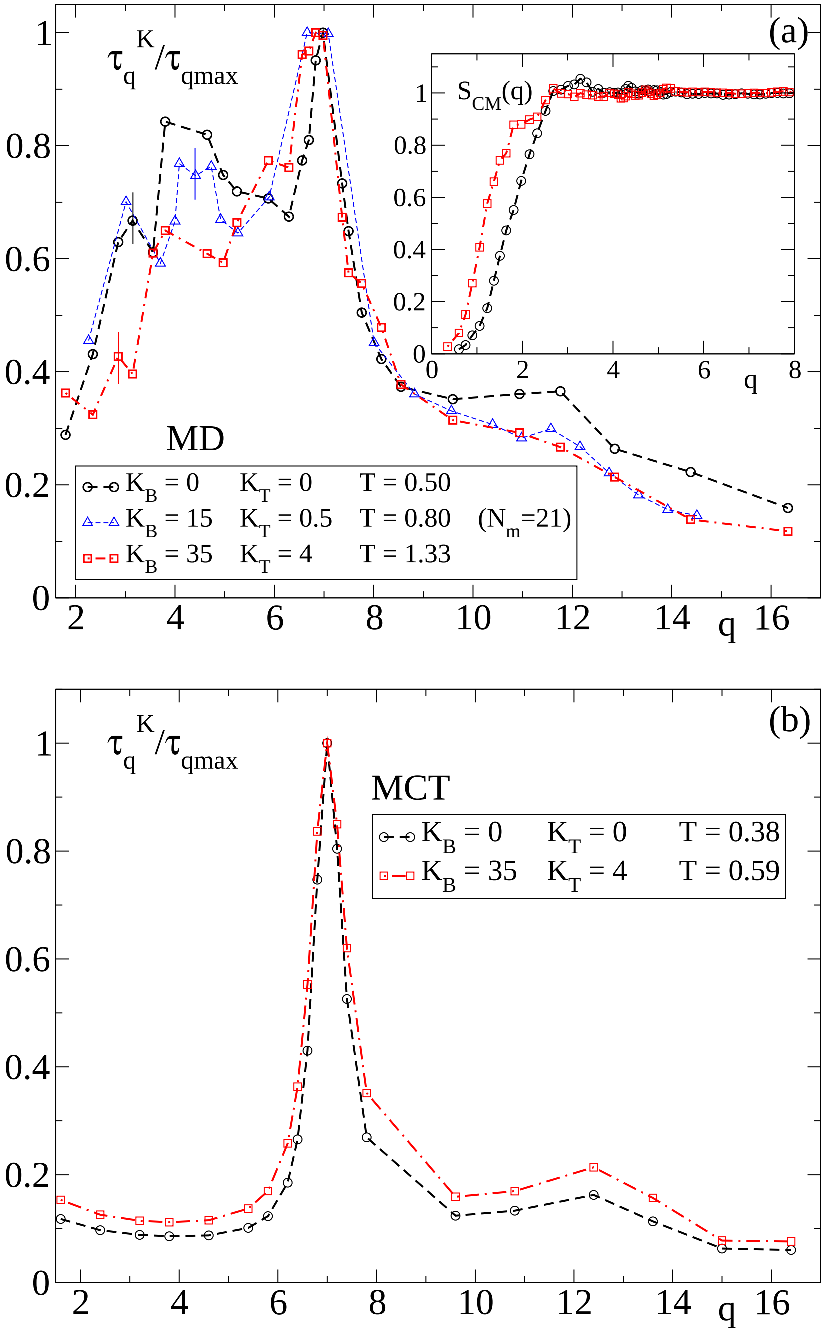

Figure 5.4: Main panels: for fully-flexible and stiffest investigated chains, q-dependence of the KWW times for density-density correlators $f(q,t)$. Data are rescaled by the respective KWW times at q_{max}. Data in (a) and (b) correspond respectively to simulation results and MCT solutions at selected temperatures (see legend). Typical error bars are included in (a). Dashed lines are guides for the eyes. Inset of panel (a): Static structure factors for the chains centers-of-mass, $S_{\mathrm{CM}}(q)$.

5.2 Chain Dynamics

All the highly non-trivial dynamic features we discussed in chapter 2, concerning the large scale chain dynamics in our systems, can be rationalized in terms of the MCT for polymer melts.

We solved the equation 3.43 for the normalized mode correlators $\Phi_{pp}(t)$ for fully flexible and stiffest chains investigated. The static quantities $S(q), c(q)$ and $\hat{C}^{-1}_{pp'}(0)$ enter the equations as external inputs. $S(q)$ and $c(q)$ have been estimated as described in the previous section and $\hat{C}^{-1}_{pp'}(0)$ were directly computed from simulations at the respective lowest investigated temperatures.

Fig. 5.5 shows a comparison, at $\epsilon_T \approx 0.2$, of the MCT solutions of equation 3.43 for the normalized mode correlators $\Phi_{pp}(t)$ [panel (b)] of the stiffest investigated chains, with the respective simulation results discussed in chapter 2 [panel (a)]. A full correspondence between MCT solutions and simulation trends is obtained. These include the long-time plateaux for $p = 3$ and $p = 5$, as well as the sequence in the complex, non-monotonous p-dependence for $p > 4$ at intermediate times. As previously done for the simulation data, we can obtain the theoretical relaxation times τ_p from the condition $\Phi_{pp}(\tau_p) = 0.3$ in the theoretical correlators. The p-dependence of the simulation and theoretical times are compared in Fig. 5.6, at common $\epsilon_T \approx 0.2$, for several values of $(K_{\mathrm{B}}, K_{\mathrm{T}})$. Again, MCT solutions are in semiquantitative agreement with the anomalous trends of simulations, with similar exponents for the effective power-laws.

As we observed in Fig.2.12 for $\Psi_{pp'}(0)$, there are off-diagonal terms of the intrachain static correlations which are non-orthogonal. We observed (see Fig. 2.17) that this non-orthogonality persists over long time scales. Fig. 5.7 shows simulation and theoretical results for normalized Rouse cross-correlators $\Phi_{pp'}(t)$, with $p = 3$ and $p' = 1, 3, 5, 7, 9$. Data correspond to the same temperatures and barrier strength (the stiffest investigated case) of the diagonal correlators of Fig. 5.5. Again, MCT qualitatively reproduces simulations trends for the case of the off-diagonal terms.

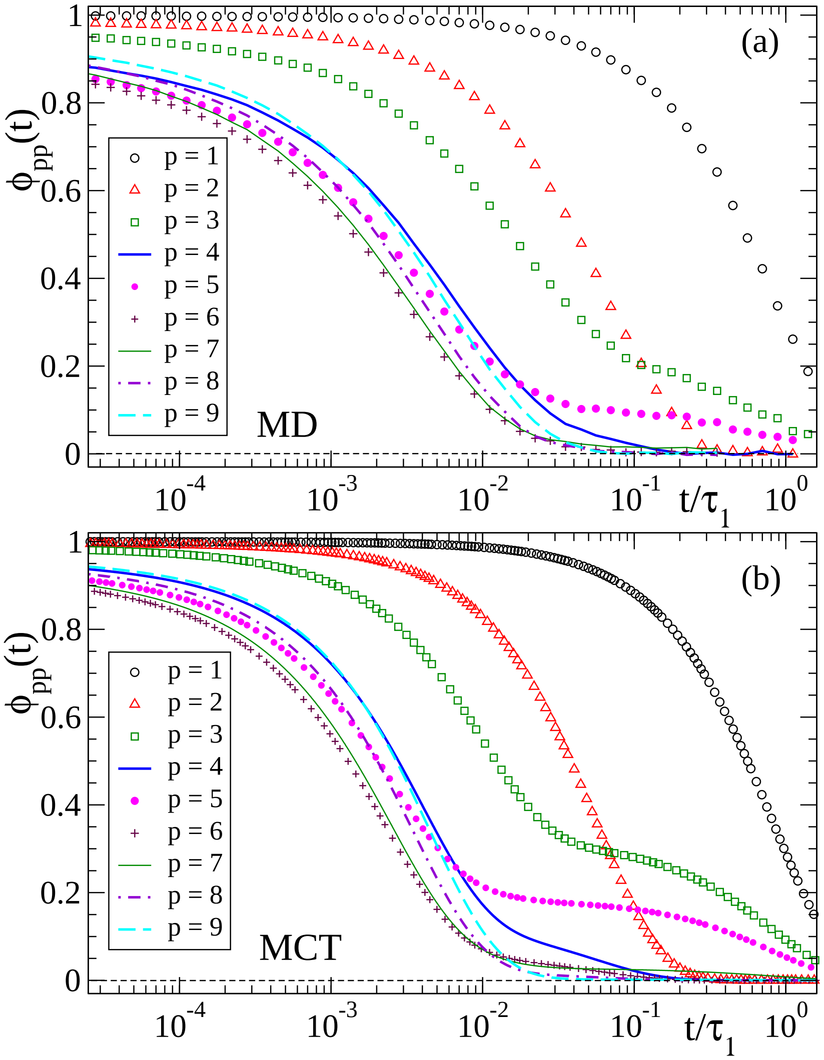

Figure 5.5: Normalized mode correlators $\Phi_{pp}(t)$ for stiff chains with $(K_\mathrm{B}, K_\mathrm{T}) = (35, 4)$. Panel (a): simulation results at $T = 1.48$. Panel (b): MCT numerical solutions at $T = 0.63$. In both panels, the absolute time is rescaled by the relaxation time τ_1 of the $p = 1$ mode.

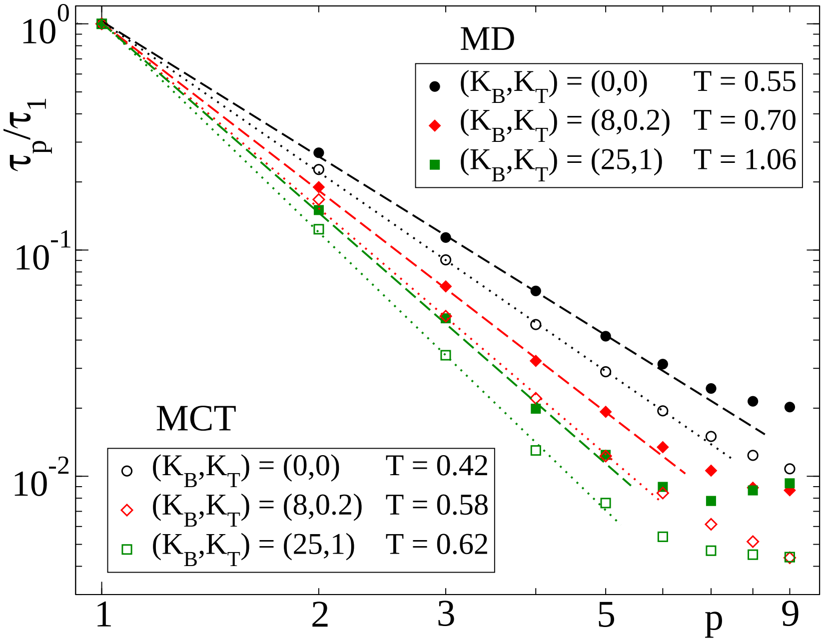

Figure 5.6: Simulation results (filled symbols) and MCT solutions (empty symbols), for the p-dependence of the relaxation times τ_p of the mode correlators. Each data set corresponds to a fixed value of $(K_\mathrm{B}, K_\mathrm{T})$ and T (see legends). For clarity, each set is rescaled by its respective τ_1. Dashed and dotted lines indicate approximate power-law behavior $\sim p^{-x}$. From top to bottom, simulations (dashed): $x = 2.0$, 2.4, 2.8; MCT (dotted): $x = 2.2$, 2.7, 3.1.

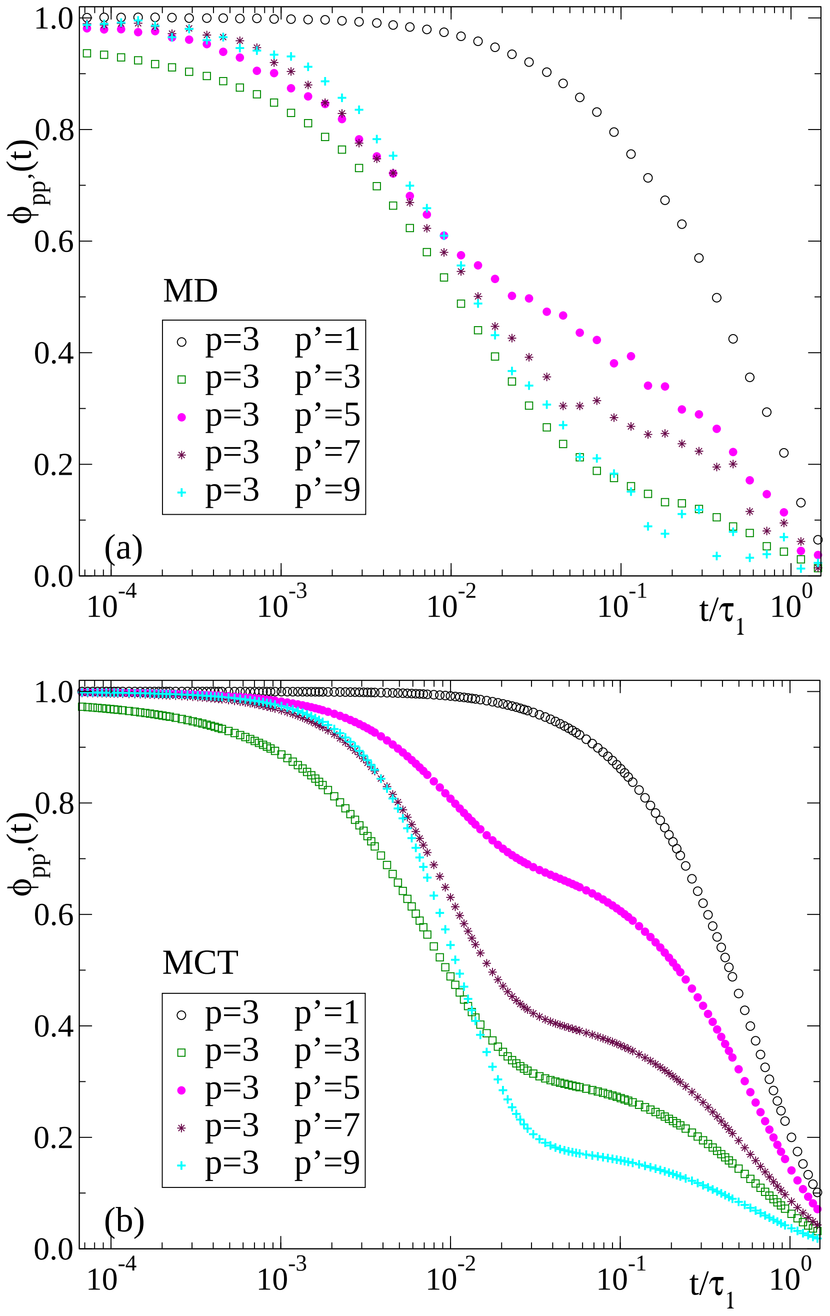

Figure 5.7: Normalized cross-correlators $\Phi_{pp'}(t)$ (for fixed $p = 3$) of stiff chains with $(K_{\rm B}, K_{\rm T}) = (35, 4)$. Panel (a): simulation results at $T = 1.48$. Panel (b): MCT numerical solutions at $T = 0.63$. In both panels, the absolute time is rescaled by the relaxation time τ_1 of the $p = 1$ mode.

Finally, it is worth noting that the good agreement between simulations and MCT for the Rouse correlators is similar for other observables probing chain dynamics. The reason is that, through the transformation $\mathbf{X}_p(t) = \sum_{j=1}^{N} P_{jp}\mathbf{r}_j(t)$, such observables can be expressed in terms of the Rouse diagonal and cross-correlators [27]. An example is given by the orientational bond correlator

$$P_{\mathrm{b}}(t) = \langle \mathbf{b}(0) \cdot \mathbf{b}(t) \rangle / \langle b^2(0) \rangle \tag{5.13}$$

where $\mathbf{b}(t)$ is the bond vector joining two consecutive monomers. Following the former transformation we find

$$\langle \mathbf{b}(0) \cdot \mathbf{b}(t) \rangle \equiv \sum_{j=1}^{N-1} \sum_{p,p'=0}^{N-1} [P^{-1}_{p,j+1} - P^{-1}_{p,j}][P^{-1}_{p',j+1} - P^{-1}_{p',j}] \langle \mathbf{X}_p(t) \cdot \mathbf{X}_{p'}(0) \rangle \tag{5.14}$$

where P^{-1} is the inverse of the matrix of coefficients P_{jp} we defined in chapter 2. Note that the expression (5.14) is *exact*. Since MCT solutions provide the Rouse correlators for all (p, p'), insertion of these in the former exact expression directly provides $P_{\mathrm{b}}(t)$. Fig. 5.8 shows simulation and MCT results of $P_{\mathrm{b}}(t)$ for several values of $(K_{\mathrm{B}}, K_{\mathrm{T}})$ from the fully-flexible limit to the stiffest investigated chains. As in previous figures, times are rescaled by the respective τ_1, and data in both panels correspond to a common separation parameter $\epsilon_T \approx 0.2$. MCT reproduces semiquantitatively the observed simulation trends. These include, on increasing barrier strength, a relative speed up and slowing down (in terms of the *scaled* time t/τ_1) of respectively the short-time and long-time dynamics. MCT also accounts for the emergence, for strong barriers, of a plateau at $t/\tau_1 \sim 10^{-2}$ and a change in the concavity of the decay.

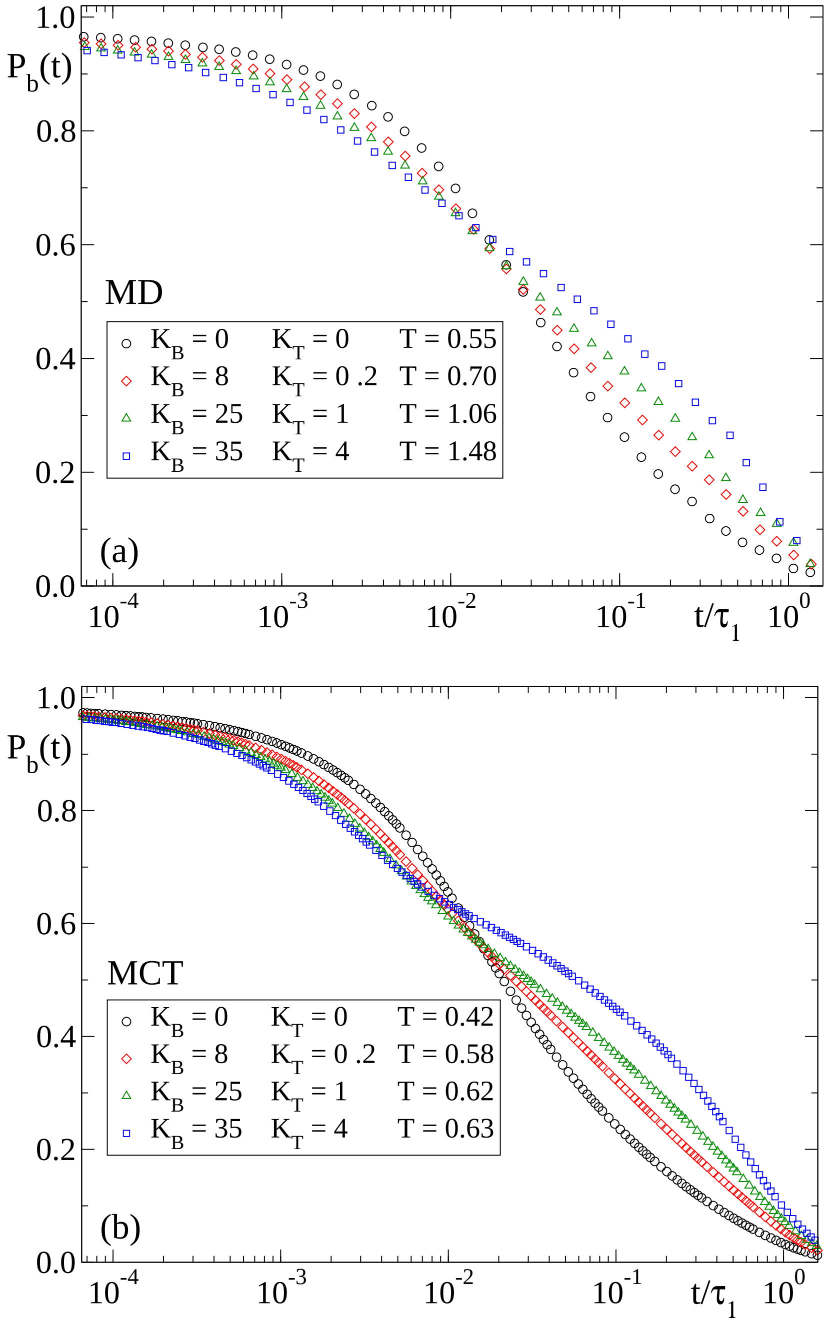

Figure 5.8: Normalized bond correlators $P_{\rm b}(t)$ for several values of the barrier strength at selected temperatures (see legend). Panel (a): simulation results. Panel (b): MCT numerical solutions. In both panels the absolute time is rescaled by the relaxation time τ_1 of the $p = 1$ mode.

Let us come back to the expression of the memory kernel of the MCT equations for the Rouse mode correlators (Eq. (3.44)). We remind that this kernel is dominated by contributions around the maximum of $S(q)$ which fully decay at times longer than the $\alpha-$relaxation time $t >> \tau_\alpha$. Thus in this long time limit, a Markovian model, like the Rouse model for fully-flexible chains, can be invoked. In their work Chong and co-workers [39] showed that the MCT for polymer dynamics in fully-flexible chains reduces to the Rouse model in the aymptotic limit of large degree of polymerization $N \to \infty$. By imposing Gaussian statistics for intrachain static correlations and performing a Markovian approximation for the memory kernel, they obtained the subdiffusive regime $\langle \Delta r^2(t) \rangle \sim t^{0.5}$ for the monomer mean-square displacements and the exponential decay of the Rouse correlators. Concerning stiff chains, we can invoke other Markovian models for semiflexible chains [54–56, 134, 135], based on the worm-like model [103, 112]. As we discussed in chapter 2, the starting point of the mentioned Markovian models is to assume a specific form for the intramolecular static correlations, e.g., the gaussian chain in the Rouse model or the worm-like model in [54–56, 134, 135]. In our work, all the correct correlations $\hat{C}_{pp'}(0)$ have been used from simulations (through the matrix $E_{pp'}$ in Eq. (3.43)). Thus, a *quantitative* confrontation of MCT with these specific Markovian models (based on the worm-like model for the intramolecular structure) is not possible. Still, we can state that the effective power laws $\tau_p \sim p^{-x}$ at intermediate and low p can be easily approximated, due to the short length of the chains ($N = 10$), by tuning γ in the expression $\tau_p \sim [p^2 + \gamma p^4]^{-1}$ proposed in [54, 55], where γ is a parameter quantifying stiffness. Still a proper discrimination between different phenomenological models would require information over a wide range of chain lengths ($N \gtrsim 100$), in order to discriminate the crossover proposed by such models from the Rouse-like behaviour at small $p-$values (large lenght scale) characterized by $\tau_p \sim p^{-2}$, to the bending regime at larger $p-$values, where the intramolecular barriers play a crucial role and $\tau_p \sim p^{-x}$ with $x > 2$. Having said this, we can create a Markovian model with the correct static correlations by using the MCT equation 3.43, but with $\delta(t)$-like functions in the kernel instead of the slow functions $F^s_{ab}(k,t)$ and $f(k,t)$. In this way the integral is reduced to an effective friction term, where the intermolecular structure $(S(k), c(k))$ is encoded. By solving the equations in this Markovian limit, we obtain the same qualitative features of Fig. 5.5. Obviously, the obtained absolute time scale is different from the solutions with the correct kernel. In Markovian models the time scale is proportional to the phenomenological friction, which is a fit parameter in such models. Therefore such models do not make predictions for, e.g., the temperature dependence of the times. This, as well as the friction, is however provided by MCT from a microscopic basis:

$$\frac{\zeta}{k_B T} = \frac{\rho}{6\pi^2} \int_0^\infty dt \int dk k^4 S(k) c^2(k) \left(\frac{1}{N} \sum_{i,j=1}^{N} F_{ij}^{\mathrm{s}}(k,t) \right) f(k,t) \tag{5.15}$$

Moreover MCT provides a unified and continuous description of both chain and glassy dynamics, down to time scales around and before the α-process. This part of the dynamic window is just ‘coarse-grained’ in the phenomenological Markovian models. Note that, e.g., the observed (and reproduced by MCT) nonmonotonous behavior of Rouse correlators (Fig. 5.5) indeed occurs in that time window.

Chapter 6

Discussion

In chapter 3 we have shown that, concerning the critical temperature T_c, MCT reproduces qualitative simulation trends for low and moderate barriers. However a strong disagreement is found on approaching the limit of stiff chains. We have also found a clear discrepancy in the trends of the λ-exponent, with a nearly constant value from theory and strongly barrier-dependent values from simulations. In this chapter we discuss possible origins of these discrepancies.

6.1 Three-Point Static Correlations

The observed disagreement between theory and simulation for strong barriers does not seem to be related with the failure of the equivalent-site approximation and ring approximation for stiff chains, which are invoked in the derivation of the MCT equations for polymers. Indeed we have shown in chapter 2 that the quality of such approximations appeared to be the same for all the range of barrier strength here investigated by simulation and MCT.

Having said this, it might be argued that the theory is simply wrong: the phenomenological MCT analysis is apparently successful, but one finds that it does not agree with the theory, for stiff chains, when solving the MCT equations. However, we remind that the phenomenological analysis has shown for all the investigated range of barrier strength: i) the validity of the two MCT universalities, i.e., the factorization theorem (Figs. 4.1 and 4.2) and the TTSP (Fig. 4.3) ii) the possibility of a good description of different dynamic observables (Figs. 4.4, 4.6 and 4.7) with a set of dynamic exponents which are consistently related, through Eqs. (3.28,3.29), to a single

λ-exponent.

We believe that all these observations, for all the investigated cases, are not fortuitous. At this point it must be noted that the predictions referred to in points i) and ii) arise, within MCT, as a consequence of the mathematical structure of the equations of motion, more precisely they originate from the bilinear form of the memory kernel, expressed as a linear combination of pair density fluctuations (see Eqs. 3.7-3.8). The specific values of the numerical solutions clearly depend on the coefficients of the bilinear products (which enter through the vertices of the kernel), but the factorization theorem, the TTSP, and the asymptotic scaling laws are universal properties provided the kernel is bilinear. Thus, the results of the phenomenological analysis suggest that the underlying physics may be connected to a bilinear memory kernel, though for high barriers the actual coefficients strongly differ from those introduced by MCT through the vertices, thus leading to theoretical results which strongly differ from simulations.

In other words, the present results suggest that there may be relevant static contributions for the case of stiff chains which are missing in the MCT vertices. Thus, the inclusion of such contributions might increase the strength of the kernel and might induce the theoretical transition at higher values of T_c, which might improve the comparison between T_c^{MCT} and T_c^{MD} of Fig. 5.2a. Recalling the three main approximations of MCT, we suggest that the convolution approximation, Eq. (3.4), might break for stiff chains. Though possibly it is not the case for intermolecular contributions, its breakdown for *intramolecular* contributions in stiff chains is, in principle, plausible.

Thus, we suggest that *intrachain* three-point static correlations should be explicitly included in the MCT vertex. Chain stiffness induces a strong directionality in the intrachain static correlations, at least at near-neighbor distances. It has been shown that directionality in static correlations can break the static convolution approximation of MCT, Eq. (3.4). A well-known example is given by silica, a network-forming system. For the latter the inclusion of three-point static correlations in the MCT vertex significantly improves the comparison between theory and simulation, with respect to the solutions obtained under the convolution approximation [113].

The calculation of the three-point static correlations involved in Eq. (3.4) is very demanding. This is because most of the computational time is consumed by the *interchain* three-point correlations. For intrachain three-point correlations the computation is not demanding. Fortunately, in the present case only the latter is necessary, since the directionality of correlations is only relevant along the chain. Thus, the convolution approximation is retained for interchain correlations, and it is modified only to include the intrachain three-point correlations. With this, the new MCT vertex reads [136]

$$\mathcal{V}(\mathbf{q},\mathbf{q}-\mathbf{k}) = \frac{\rho}{2q^4}S(q)S(k)S(|\mathbf{q}-\mathbf{k}|)[\mathbf{q}\cdot\mathbf{k}c(k) \\ +\mathbf{q}\cdot(\mathbf{q}-\mathbf{k})c(|\mathbf{q}-\mathbf{k}|)+\rho q^2 c_3(\mathbf{q},\mathbf{q}-\mathbf{k})]^2, \tag{6.1}$$

where $c_3(\mathbf{q},\mathbf{q}-\mathbf{k})$ is the three-point *intramolecular* direct correlation function, given by

$$\rho^2 c_3(\mathbf{q},\mathbf{q}-\mathbf{k}) = 1 - \frac{\omega_3(\mathbf{q},\mathbf{q}-\mathbf{k})}{\omega(q)\omega(k)\omega(|\mathbf{q}-\mathbf{k}|)}, \tag{6.2}$$

and $\omega_3(\mathbf{q},\mathbf{q}-\mathbf{k})$ is the three-point intramolecular structure factor

$$\omega_3(\mathbf{q},\mathbf{q}-\mathbf{k}) = \frac{1}{nN}\sum_{j=1}^{n}\sum_{a,b,c=1}^{N}\times \\ \exp\{i[-\mathbf{q}\cdot\mathbf{r}_j^a + \mathbf{k}\cdot\mathbf{r}_j^b + (\mathbf{q}-\mathbf{k})\cdot\mathbf{r}_j^c]\}. \tag{6.3}$$

The convolution approximation for intrachain correlations assumes $\omega_3(\mathbf{q},\mathbf{q}-\mathbf{k}) = \omega(q)\omega(k)\omega(|\mathbf{q}-\mathbf{k}|)$, or equivalently $c_3(\mathbf{q},\mathbf{q}-\mathbf{k}) = 0$, reducing the vertex (6.1) to the original Eq. (3.8).

Figs. 6.1 and 6.2 show representative tests of the convolution approximation for respectively fully-flexible and stiffest investigated chains. Following the scheme proposed in Ref. [39], the vectors $\mathbf{q}$, $\mathbf{k}$ and $\mathbf{p} = \mathbf{q}-\mathbf{k}$ define the sides of a triangle, the first two enclosing an angle ϕ given by $\cos\phi = (q^2+k^2-p^2)/2qk$. Panels (a) and (b) in Fig. 6.1 show a test of the corresponding expression for an equilateral triangle, $\omega_3(q,q,q) = \omega^3(q)$. Panels (a) and (b) in Fig. 6.2 show a similar test for equal moduli $k = q$ and all the relative orientations (given by $\cos\phi$) of $\mathbf{q}$ and $\mathbf{k}$. In other words, we test the approximation $\omega_3(q,q,p = q\sqrt{2(1-\cos\phi)}) = \omega^2(q)\omega(p)$. Data in Fig. 6.2 are represented as a function of $\cos\phi$ for two characteristic wave vectors, corresponding to the first minimum and second maximum of the respective $\omega_3(q,q,q)$ (see Fig. 6.1).

As already noted in Ref. [102], the convolution approximation for intrachain static correlations provides a good description of ω_3 in the fully-flexible limit. As expected, the quality of the approximation decreases by introducing intramolecular barriers. Still it constitutes a good approximation for all the investigated barrier strength. In the

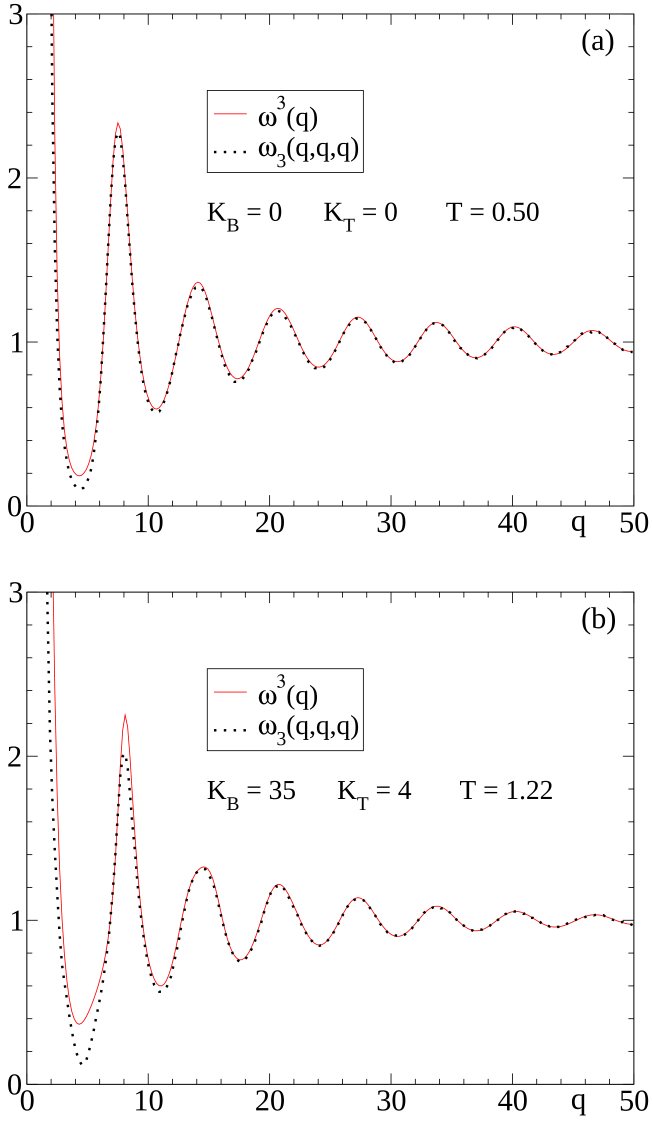

Figure 6.1: Comparison between $\omega_3(q, q, q)$ (dotted lines) and the convolution approximation $\omega^3(q)$ (solid lines). Panel (a): fully-flexible chains at $T = 0.50$. Panel (b): Stiffest investigated chains at $T = 1.22$.

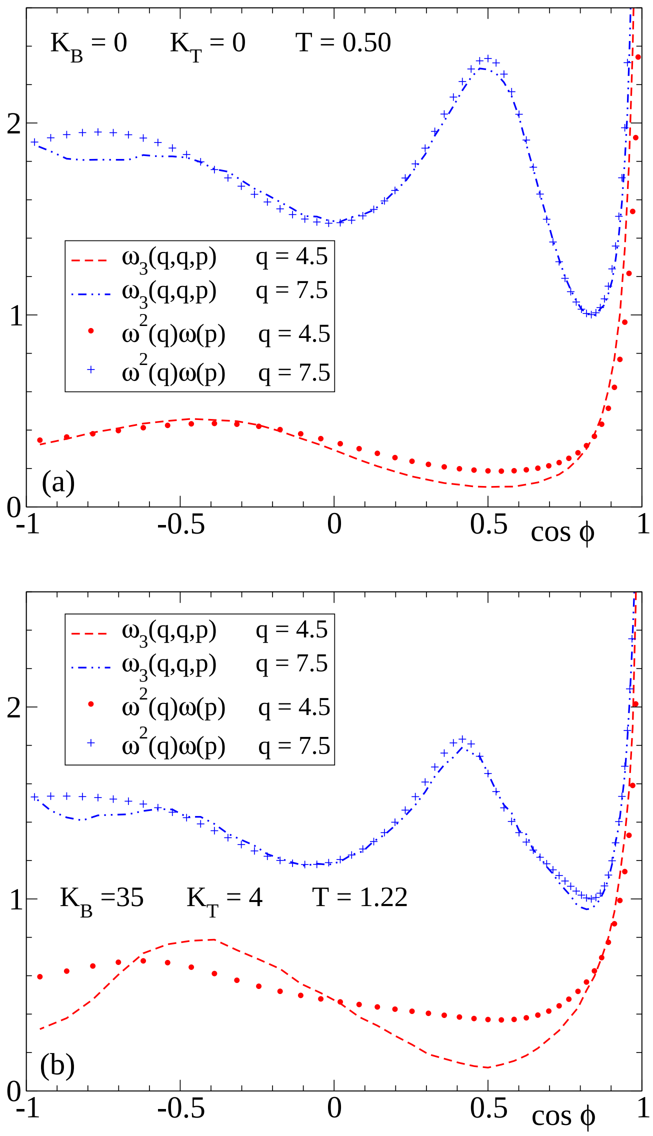

Figure 6.2: Comparison of $\omega_3(q, q, p = q\sqrt{2(1-\cos\phi)})$ (lines) with the convolution approximation $\omega^2(q)\omega(p)$ (symbols), for two selected values $q = 4.5$ and 7.5. Panel (a): fully-flexible chains at $T = 0.50$. Panel (b): Stiffest investigated chains at $T = 1.22$.

case of wave vectors around the first peak of $S(q)$, $q_{\max} \approx 7$, the quality is almost unaffected by the barrier strength, i.e., the terms $c_3(\mathbf{q}_{\max}, \mathbf{q}_{\max} - \mathbf{k})$ will be small even for the stiffest investigated chains. It must be noted that the MCT kernel is usually dominated by the contributions around $q_{\max}$. Thus, the former observations suggest that the inclusion of the three-point static correlations will modify weakly the MCT solutions obtained under the convolution approximation. We confirm this by obtaining numerical solutions with the vertex (6.1), for which we compute the input quantities involved in Eqs. (6.2, 6.3) directly from the simulations. The so-obtained values of the critical temperature T_{c} and λ-exponents raise by $\approx 1\%$ as much, even for the stiffest chains, with respect to the previous values (Fig. 5.2) found under the assumption $c_3 = 0$. With all this, we conclude that the observed discrepancies between simulation and theoretical trends of T_{c} and λ are not related to the breakdown of the convolution approximation for static three-point correlations. The latter indeed retains its validity for all the investigated range of barrier strength.

6.2 Dynamic Heterogeneities

As we discussed previously, the main weakness of the MCT is that it predicts dynamic arrest at the critical temperature T_c while the expected power-law divergences of the $\alpha-$relaxation times are not observed in practice (see chapter 3). This is connected with the quality of the Kawasaki approximation for dynamic correlations (see chapter 3) which breaks down on decreasing temperature. This feature is specially critical around the α-time scale [116–119, 137], leading to the complete failure of the MCT predictions associated to it, as the time-temperature superposition of density correlators, or the same power law behaviour for the monomer diffusion coefficient and $\alpha-$relaxation times $D, \tau_\alpha^{-1} \sim (T - T_c)^\gamma$, namely the Stokes-Einstein (S-E) relation for transport coefficients $D \sim \tau_\alpha^{-1}$. In chapter 4 we have shown that the time-temperature-superposition-principle fails for temperatures close to the critical temperature T_c. In order to test the S-E relation for our systems, we should be able to estimate the monomer diffusion coefficient D from simulation data through the relation $D = \lim_{t\to\infty} \langle \Delta r^2(t) \rangle / 6t$, where $\langle \Delta r^2(t) \rangle$ is the monomer mean squared displacement (MSD). In chapter 2 (see Fig. 2.7) we observed that after the caging plateau, monomers go through a subdiffusive regime in the range $1 \lesssim \langle \Delta r^2(t) \rangle \lesssim R_{ee}^2$. The linear diffusive regime $\langle \Delta r^2(t) \rangle \sim t$ is reached, within the simulation time window, only for low barriers and at the highest investigated

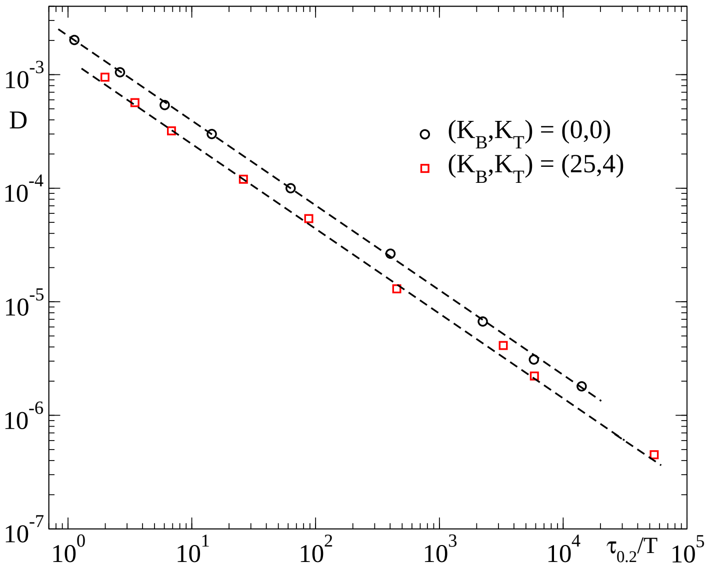

Figure 6.3: Power law fits of diffusivities D as a function of $\tau_{0.2}/T$: $D \sim (\tau_{0.2}/T)^{-0.75}$ for fully flexible and stiff chains.

temperatures. However the monomer diffusion coefficient D is equal to the diffusion coefficient D_{CM} of the chain center of mass, which indeed reaches the diffusive regime in the simulation time window and that can be estimated as $D_{CM} = \lim_{t\to\infty}\langle\Delta r^2_{CM}(t)\rangle/6t$.

Fig.6.3 shows a test of the S-E relation for fully flexible and stiff chains. We represent the monomer diffusion coefficient $D = D_{CM}$ as a function of τ_α/T. Let us remember that the α-relaxation time has been evaluated as $f(q_{\max}, \tau_\alpha) = 0.2$. We note that D and τ_α scale differently with temperature, violating the prediction of MCT. We note that $D \sim (\tau_{0.2}/T)^{-0.75}$ for fully flexible and stiff chains.

The decoupling of diffusion and relaxation, which is observed experimentally for temperatures close to the T_g, is usually assigned to the emergence of strong dynamic heterogeneities on approaching the glass transition [116–119,137]. The basic idea is that the system near the glass transition contain different fluctuating domains of particles possesing an enhanced or reduced mobility relative to the average. Domains with the slowest particles dominate structural relaxation and domains with the fast particles dominate diffusion. Having noted this we may speculate that, for some reason to be understood, increasing the barrier strength strongly enhances dynamic heterogeneity. This might result in a lower quality of the MCT and might be the reason for the observed discrepancies between theory and simulation trends for T_c.

Now we show that this is not actually the case, and that there is no correlation between barrier strength and enhanced dynamic heterogeneity. In order to probe dynamical heterogeneity in our systems, and elucidate the connection between this heterogeneity and the decoupling of transport coefficients, we should point out two different characteristic time scales connected with the domains of fast and slow particles, and that scale respectively as the inverse of the diffusion coefficient and the $\alpha-$relaxation time. To do this we introduce the concept of non-Gaussian parameters. The self-density correlator $f^s(q,t)$ can be written as the spatial Fourier transform of the Van-Hove self correlation function:

$$f^s(q,t) = \int 4\pi r^2 G^s(r,t)\frac{\sin(qr)}{qr}dr \tag{6.4}$$

The van Hove function $G^s(r,t)$ is proportional to the probability that a particle placed at the origin at time $t = 0$, can be found at distance r at time t. It can be easily demonstrated that the Van-Hove function is a Gaussian function of r in the ballistic limit $t \longrightarrow 0$ and in the Brownian diffusion limit $t \longrightarrow \infty$. If we suppose that $G^s(r,t)$ is Gaussian at all times we have:

$$G^s(r,t) = \left[\frac{3}{2\pi\langle\Delta r^2(t)\rangle}\right]^{3/2} \exp\left[-\frac{3r^2}{2\langle\Delta r^2(t)\rangle}\right] \tag{6.5}$$

where $\langle\Delta r^2\rangle$ is the mean square displacement (MSD) of a particle. If we insert eq. 6.5 in eq. 6.4 the self-density correlator takes the form:

$$f^s(q,t) = \exp\left(-\frac{q^2}{6}\langle\Delta r^2(t)\rangle\right) \tag{6.6}$$

Systematic corrections to the Gaussian approximation for $f^s(q,t)$ can be obtained in terms of its expansion in powers of q^2:

$$f^s(q,t) = \exp\left(-\frac{q^2}{6}\langle\Delta r^2(t)\rangle + \frac{\alpha_2(t)\langle\Delta r^2(t)\rangle^2}{72}q^4 + ...\right) \tag{6.7}$$

where the leading correction to the Gaussian behaviour is expressed in terms of the so-called non-Gaussian parameter $\alpha_2(t)$:

$$\alpha_2 = \frac{3\langle\Delta r^4\rangle}{5\langle\Delta r^2\rangle^2} - 1 \tag{6.8}$$

In the following we will refer to $\alpha_2(t)$ as the 'fast' non-Gaussian parameter. Recently a new function which quantifies deviations from Gaussian behaviour have been intro-

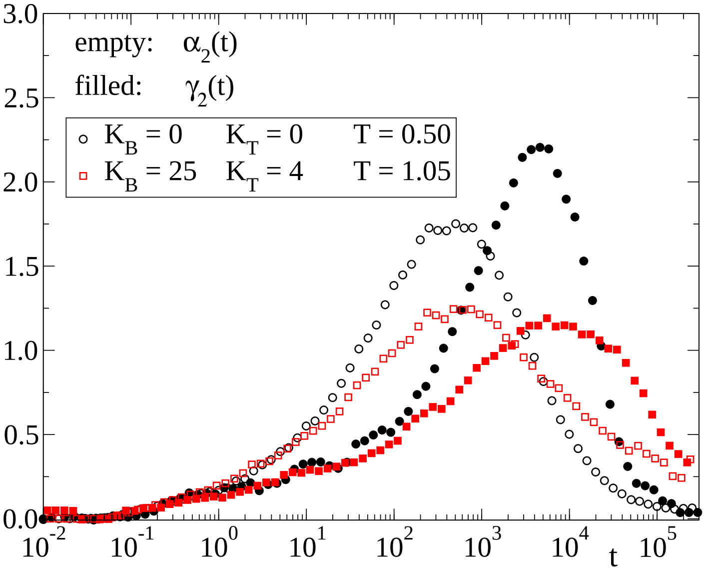

Figure 6.4: For two selected temperatures with similar decaging and α-relaxation times, non-gaussian parameters of fully-flexible (circles) and stiff chains with $(K_{\mathrm{B}}, K_{\mathrm{T}}) = (25, 4)$ (squares). Empty and filled symbols correspond respectively to the fast ($\alpha_2(t)$) and slow ($\gamma_2(t)$) parameters.

duced by Flenner and Szamel [137]. This new 'slow' non-Gaussian paramater is defined as:

$$\gamma_2 = \frac{1}{3}\langle \Delta r^2(t) \rangle \langle \frac{1}{\Delta r^2(t)} \rangle - 1 \tag{6.9}$$

In eq. 6.8 $\alpha_2(t)$ compares the mean quartic displacement of a monomer to the square of the MSD. Negative values of $\alpha_2(t)$ imply that a particle moves less far than expected from diffusion motion. On the other hand, positive valuse of $\alpha_2(t)$ indicate that a particle moves faster than a particle in the diffusive regime at the same time t. Thus, high values of $\alpha_2(t)$ are good indicators of enhanced mobility relative to free diffusion. This effect is generally maximum at the time t^* around the end of the caging regime. Thus, non-Gaussianity of $\alpha_2(t)$ arises because of caging and the resulted correlated motion necessary for a fraction of particles to escape from the cages formed by their neighbors. Thus, $\alpha_2(t)$ increases from zero at $t = 0$ up to a maximum at t^*, and decays to zero at longer times. The observed increase of the maximum $\alpha_2(t^*)$ on decreasing temperature reflects a progressive enhancement of dynamic heterogeneity, at the decaging process, on approaching the glass transition.

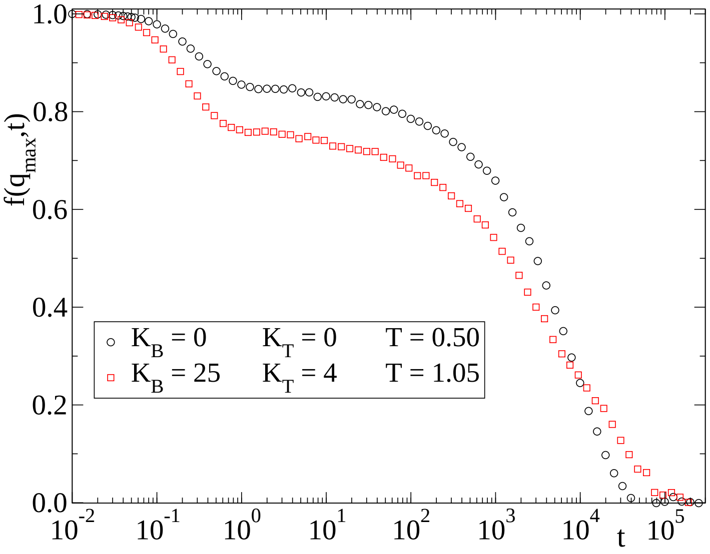

Figure 6.5: Density-density correlator $f(q_{\rm max}, t)$ for fully-flexible (circles) and stiff chains with $(K_{\rm B}, K_{\rm T}) = (25, 4)$ (squares). Data are shown for the same selected temperatures of Fig. 6.4.

The slow parameter $\gamma_2(t)$ exhibits analogous trends for the temperature and time-dependence. However the $\gamma_2(t)$ parameter, differently from $\alpha_2(t)$, weights very strongly particles which have moved less than expected from Gaussian behaviour through the term $\langle 1/\Delta r^2(t)\rangle$ in eq. 6.9. Indeed, the maximum of $\gamma_2(t)$ takes place at t^{**} greater than t^*, namely around the α-relaxation time τ_α. Thus, this effect originates from a significant population of particles which at $t^{**} \sim \tau_\alpha$ have performed much *smaller* displacements than the average [137].

Fig. 6.4 compares simulation results of $\alpha_2(t)$ and $\gamma_2(t)$, for the fully-flexible case and for very stiff chains. For a fair comparison we have selected temperatures at which the respective α-relaxation times are similar. These are $T = 0.50$ and $T = 1.05$, for respectively fully-flexible and stiff chains, and correspond to a separation parameter $\epsilon_T \sim 0.04$. In Fig. 6.5 we display $f(q_{\rm max}, t)$ for both systems at the former temperatures, showing that the respective α-time scales are roughly the same, $\tau_\alpha \sim 10^4$. The decaging times, which can be estimated from the start of the decay from the plateau in $f(q_{\rm max}, t)$, are also roughly the same, $t^* \sim 500$. This equivalence is indeed reflected in the trends of the non-gaussian parameters in Fig. 6.4. Thus, in both systems $\alpha_2(t)$ is peaked at $t^* \sim 500$ and $\gamma_2(t)$ is peaked at $t^{**} \sim 10^4$.

Fig 6.6 shows $(t^*)^{-1}$ as a function of t^{**}/T. In both fully flexible and stiff chains,

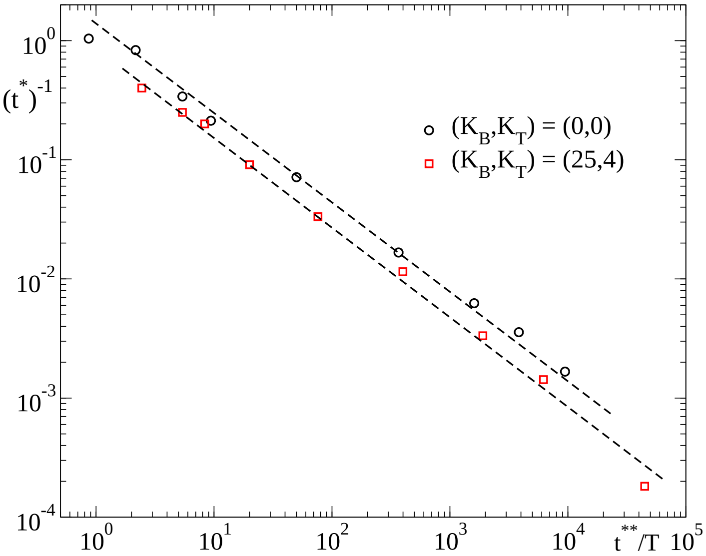

Figure 6.6: Power law fits of $(t^*)^{-1}$ as a function of t^{**}/T: $(t^*)^{-1} \sim (t^{**}/T)^{-0.75}$ for fully flexible and stiff chains.

we observe power law behaviour with the same exponent that we have found for the diffusion coefficient D as a function of τ_α/T (see Fig. 6.3). Therefore these results confirm the proposed interpretation for the violation of the S-E relation as due to the presence of dynamic heterogeneities (see above).

Having noted the equivalence for fully flexible and stiff chains of the time scales t^*, t^{**}, τ_α in Figs. (6.4) and (6.5), the data do not reflect any enhancement of dynamic heterogeneity on increasing the barrier strength. Actually, the opposite effect is suggested by the lower values of $\alpha_2(t)$ and $\gamma_2(t)$ for stiff chains with respect to the fully-flexible case. With this, we discard a major role of dynamic heterogeneities as the reason for the observed discrepancies between simulations and MCT solutions for very stiff chains.

6.3 Chain Packing

As mentioned in Chapter 5 and shown in Fig. 5.4, MCT fails at reproducing the peak around $q_{\mathrm{C}} \sim 4$ for the q-dependence of the KWW times of density-density correlators. As noted in Ref. [39] for the fully-flexible case, the origin of this peak may be related to dynamic correlations between centers-of-mass of the chains. The latter might arise from the effective packing between the polymer coils, interacting as fully penetrable spheres of size R_{g}. This interpretation is not clear in view of the results of Fig. 5.4, since the value of q_{C} does not seem to be related with $2\pi/R_{\mathrm{g}}$. Having noted this, Chong *et al.* [39] found that the incorporation of the static correlations between the centers-of-mass in the MCT equations did not improve the description of the simulation results. As shown in [39], this is not unexpected due to the almost featureless form of the static structure factor of the centers-of-mass $S_{\mathrm{CM}}(q)$. The inset of Fig. 5.4a shows simulation results of $S_{\mathrm{CM}}(q)$, for the same barrier strength and temperatures of the KWW times in the main panel. The introduction of chain stiffness does not induce significant features in $S_{\mathrm{CM}}(q)$, apart from a stronger signal at low q. The latter indeed suggests that packing effects between the polymer coils are even weaker than for the fully-flexible case. Within the former interpretation, this would be consistent with the lower intensity of the mentioned peak of $\tau_q^{\mathrm{K}}/\tau_{q_{\mathrm{max}}}$ at $q_{\mathrm{C}} \sim 4$. All these results suggest that discrepancies between simulations and MCT on increasing chain stiffness are not related to a dynamic coupling, not accounted for within the theory, to the slow modes at $q_{\mathrm{C}} \sim 4$. Indeed, this coupling seems to be weaker for stiff chains.

6.4 Outlook

In summary, in this chapter we have discussed possible origins for the discrepancies, concerning the structural relaxation, between simulations and MCT on increasing barrier strength. We discard a major role, in comparison with the fully-flexible case, of three-point static correlations, dynamic heterogeneities and chain packing. These effects become even weaker on increasing chain stiffness. We remind that such effects are indeed neglected in the derivation of the MCT equations used here (see Chapter 3). Results in this section suggest that this is not less justified for very stiff chains than for fully-flexible ones.

How to improve the theory to account for dynamic trends in stiff chains is an open question. A way might be the reformulation or extension of the MCT equations, retaining the bilinear form of the kernel, in terms of new dynamic observables coupled to density fluctuations. Such observables can be adequate for describing particular dynamic features which are not captured by the usual observables, i.e., the number density fluctuations $\rho(\mathbf{q}, t)$. Some examples are roto-translational site fluctuations adapted to the molecular symmetry, as has been shown, e.g., for dumbbell-like molecules [36, 138] or for a simple model of orthoterphenyl [37]. The inclusion of density fluctuations of centers-of-mass improve results for rigid molecules [37] concerning a peak in $\tau_q^{\mathrm{K}}/\tau_{q_{\max}}$ at intermediate q [139], similar to that observed here at $q_{\mathrm{C}} \sim 4$. As discussed above, this is not the case for polymer chains. Though there is no characteristic symmetry in polymer chains, roto-translational density fluctuations can also be defined over sites a, b at some characteristic distance $|a - b|$, perhaps probing the relevant length scale $2\pi/q_{\mathrm{C}}$, which according to the data of Fig. 5.4 seems to depend weakly on the barrier strength. Whether this procedure may improve the agreement between MCT and simulations remains to be solved.

Chapter 7

Polymer Blends

7.1 Model and Simulation Details

We simulate a binary mixture of bead-spring chains. Monomers in the same chain are identical, i.e, of the same species (A or B). Each chain consists of $N = 21$ monomers, which is below the entanglement lenght [68, 104]. All monomers have identical mass $m = 1$. The model for the intermolecular and intramolecular interactions is the same discussed fot the homopolymer case in chapter 1. Non-bonded interactions between monomers are given by the potential in Eq. 1.6 with α, $\beta \in \{\mathrm{A, B}\}$. The interaction diameters are $\sigma_{\mathrm{AA}} = 1.6$, $\sigma_{\mathrm{AB}} = 1.3$, and $\sigma_{\mathrm{BB}} = 1$. Chain connectivity is introduced by a FENE potential Eq. (1.7). Intramolecular barriers are implemented by means of the bending and torsional potentials Eqs. (1.8) and (1.9)

In all the investigated systems the A-chains are fully-flexible, i.e., $K_{\mathrm{B}} = K_{\mathrm{T}} = 0$. We investigate two models (I and II) for the B-chains. In the model I all the B-chains are fully-flexible. In the model II all the B-chains are semiflexible, with $K_{\mathrm{B}} = 15$ and $K_{\mathrm{T}} = 0.5$.

The blend composition is $x_{\mathrm{B}} = N_{\mathrm{B}}/(N_{\mathrm{A}} + N_{\mathrm{B}})$, with N_α the total number of α-monomers in the system. All simulations are performed at fixed composition $x_{\mathrm{B}} = 0.3$. Most of the simulated systems have 105 A-chains and 45 B-chains. At the lowest investigated temperatures we have used smaller systems of 49 A-chains and 21 B-chains. We have performed additional simulations for B-homopolymers of $N = 21$, with a system size ranging from 200 to 500 chains according to the simulated temperature. All the simulated systems have a packing fraction $\phi = [\pi/(6V)](N_{\mathrm{A}}\sigma_{\mathrm{AA}}^3 + N_{\mathrm{B}}\sigma_{\mathrm{BB}}^3) = 0.53$, with V the volume of the cubic simulation box. We implement periodic boundary conditions. Equations of motion are integrated in the velocity Verlet scheme [80], with a time step ranging from 10^{-4} to 4×10^{-3} according to the simulated temperature. The procedures for the preparation of the samples in the simulation box, the thermalization and the equilibration are the same employed for the homopolymer case (see section 1.1). After equilibration at each state point, the corresponding production run is performed in the microcanonical ensemble. The longest production runs are of about 400 million time steps. Averages are performed over up to four independent boxes, with 20 equispaced time origins per simulated box.

7.2 Chain Size and Mean Squared Displacements

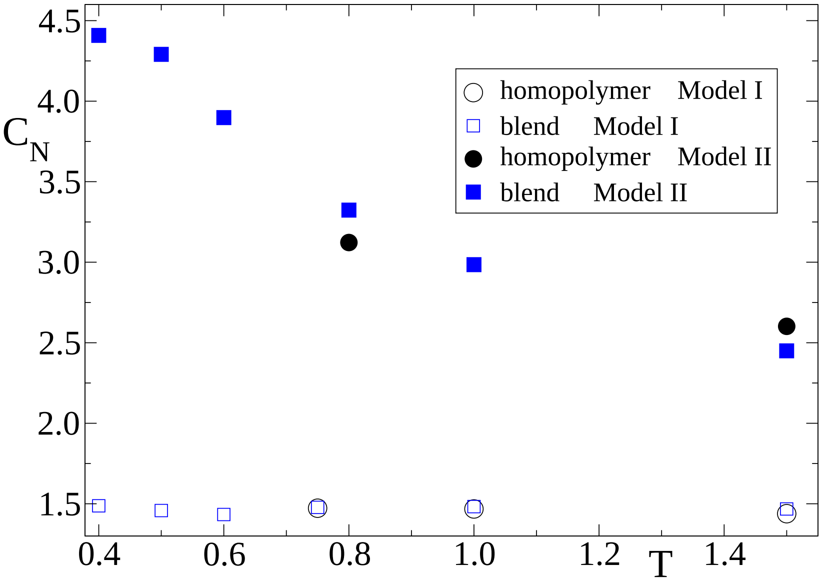

Figure 7.1: Temperature dependence of the characteristic ratio of the fully-flexible and semiflexible B-chains, both in the homopolymer and in the blend.

The selected values of the bending and torsion constants $(K_{\mathrm{B}}, K_{\mathrm{T}})$ considerably stretch the semiflexible B-chains in comparison with the fully-flexible case. As we already discussed in section 1.1, this can be quantified by the characteristic ratio, $C_N = \langle R_{ee}^2\rangle/(N\langle b^2\rangle)$, where $\langle R_{ee}^2\rangle$ and $\langle b^2\rangle$ are respectively the average squared end-to-end radius and bond length of the B-chains. Figure 7.1 shows results of C_N for the fully-flexible and semiflexible B-chains. The fully-flexible B-chains exhibit an almost T-independent value $C_N \lesssim 1.5$, both in the homopolymer and in the blend. On

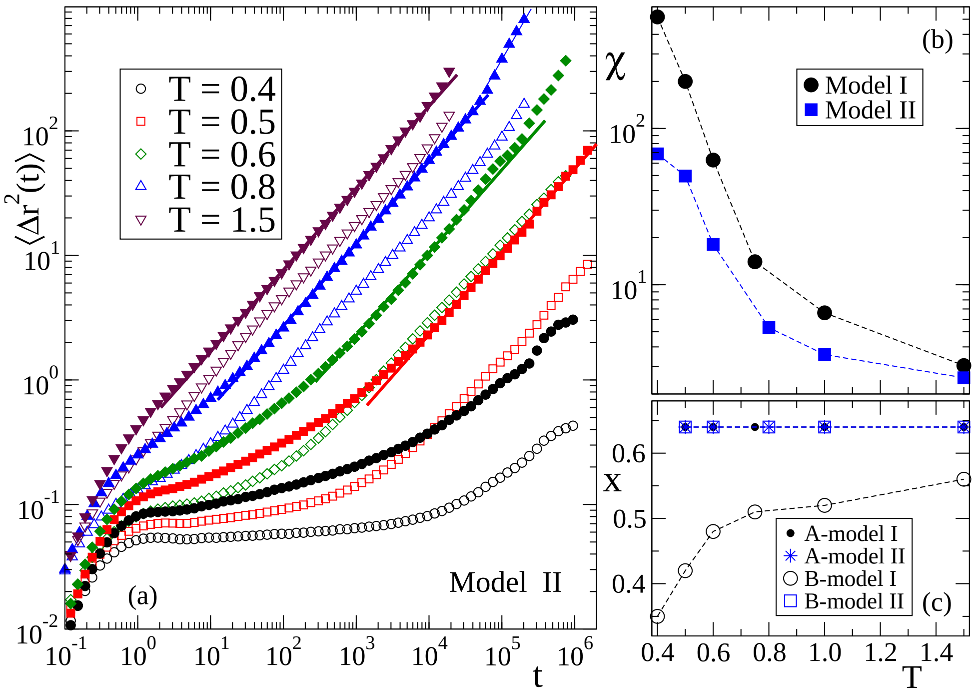

Figure 7.2: Panel (a): MSD in the model II at the different investigated temperatures. Empty and filled symbols correspond respectively to A- and B-monomers. Data sets with the same symbol code correspond to the same temperature. Thick straight lines indicate fits to power law behaviour $\langle\Delta r^2(t)\rangle \sim t^x$, with $x = 0.64$, over broad time windows. The thin line corresponds to the diffusive limit $\langle\Delta r^2(t)\rangle \sim t$. Panel (b): temperature dependence of the dynamic asymmetry (see text) for both models I and II. Panel (c): temperature dependence of the exponent x of the observed power law in the MSD (see above), for both models I and II.

the contrary, for the semiflexible B-chains decreasing temperature yields effectively higher intramolecular barriers. Thus, the chains become stiffer, and C_N shows a strong increase on decreasing temperature. In the blend we find a variation of an 80 %, from $C_N = 2.45$ to $C_N = 4.40$, over the investigated T-range.

Figure 7.2a shows results for the mean squared displacement (MSD) of both species A and B in the model II, at all the investigated temperatures. After the initial ballistic regime, a plateau arises for both components at $T < 1.5$, and extends over longer time scales on decreasing temperature. This reflects the usual caging regime observed in glass-forming systems when approaching a glass transition. In analogy with previous observations for the model I [65,66], there is a progressive separation, on decreasing T, of the time scales of the A- and B-monomers. We quantify the dynamic asymmetry in the blend as the ratio $\chi = \tau_{\mathrm{A}}/\tau_{\mathrm{B}}$, where τ_α is the time at which the MSD reaches the value $\langle \Delta r_{\alpha}^2(\tau_\alpha)\rangle = 0.45$. This roughly corresponds to the time scale of the structural α-relaxation (segmental relaxation). Figure 7.2b shows the T-dependence of the dynamic asymmetry, both for models I and II. In both cases the dynamic asymmetry becomes stronger on decreasing T. However, this effect is less pronounced in the model II, which shows a lower χ than the model I at the same temperature, blend composition and packing fraction. This is not surprising since the only difference between both models is the strength of the intramolecular barriers in the B-chains. Thus, dynamics of the B-monomers in the semiflexible homopolymer are strongly slowed down respect to the fully-flexible case (see discussion in section 2.2 and [98]), and blending with the same A-homopolymer leads to a weaker dynamic asymmetry in the model II.

For times longer than τ_α, the MSD of both species exhibits subdiffusive behaviour over several time decades, prior to the final crossover to diffusive behaviour at much longer times. The subdiffusive regime can be described by an effective power law $\langle \Delta r^2(t)\rangle \sim t^x$, with $x < 1$. This is a consequence of chain connectivity and a characteristic feature of polymer systems. In the case of fully-flexible homopolymers it reflects Rouse dynamics. Figure 7.2c shows the temperature dependence of the x-exponents for the two species in both models I and II. Within statistics, the (fully-flexible) A-chains show the same temperature independent exponent, $x \approx 0.64$, in both models. This is also the value observed for the fully-flexible A- and B-homopolymers (not shown), and can be easily understood in terms of Rouse dynamics. The value $x \approx 0.64$ is higher than the Rouse exponent $x = 0.5$, which is the effective value predicted by the Rouse model in the limit $N \to \infty$ [27]. Thus, the former difference is mostly due to the finite size, $N = 21$, of the chains [69]. We obtain a similar, almost T-independent, exponent $x \sim 0.64$ for the semiflexible B-homopolymer. This coincidence is probably fortuitous, since the x-value for the semiflexible homopolymer cannot be assigned to Rouse dynamics, which does not incorporate semiflexibility.

Concerning the exponents for the B-chains *in the blend* they exhibit a rather different behaviour in the models I and II (see Figure 7.2c). In the model I, the exponent x decreases monotonically, taking values much smaller than the T-independent value $x = 0.64$ found for the fully-flexible B-homopolymer.

This trend reflects the breakdown of the Rouse model for the fully-flexible B-chains in the blend, as discussed in [67]. This breakdown is also reflected in the anomalous scaling observed for the relaxation times of the Rouse modes on decreasing T (see below). The lowest investigated temperature in the model II at which x can be solved

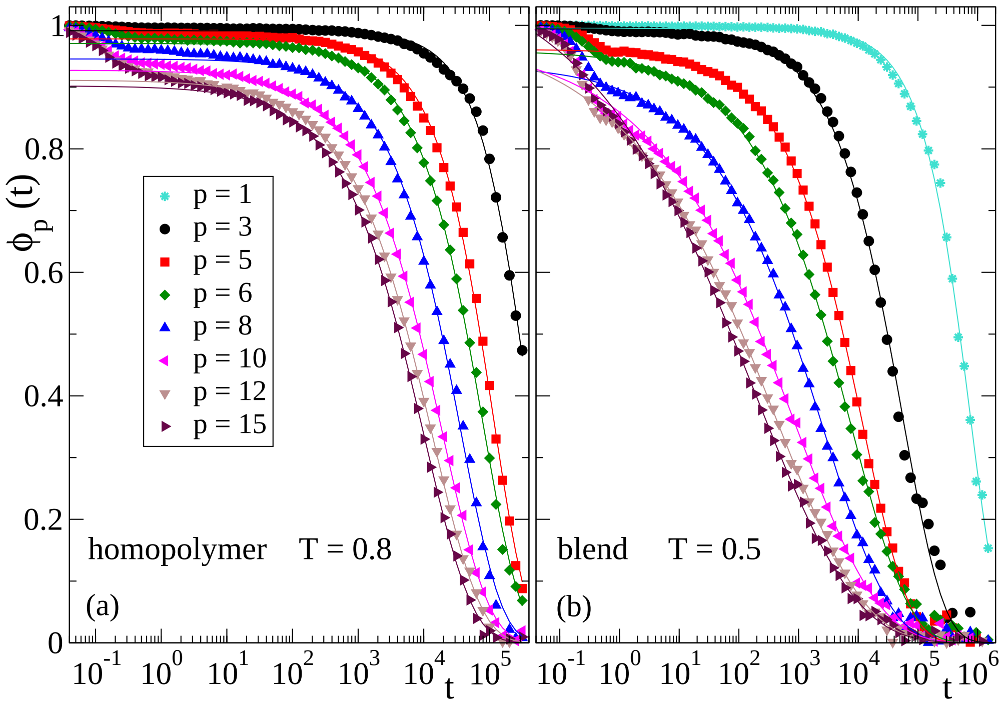

Figure 7.3: Symbols: Rouse correlators for semiflexible B-chains in the homopolymer state (a) and in the blend (b), at respectively $T = 0.8$ and $T = 0.5$. Lines are fits to stretched exponentials (see text).

is $T = 0.5$. The dynamic asymmetry at this T is the same that in the model I at $T \gtrsim 0.6$, for which x has decreased by about a 15% from its value at $T = 1.5$. On the contrary, in the model II it remains, within statistics, constant with a value $x \sim 0.64$, as observed for the semiflexible B-homopolymer (see above).

7.3 Rouse Modes

The latter observations suggest that, unlike for fully-flexible polymers, scaling properties for chain dynamics in semiflexible polymers may be unaltered by blending. We confirm this point by analyzing the relaxation of the internal chain degrees of freedom. This can be quantified by computing the correlators of the Rouse modes. Definitions of the Rouse modes $\mathbf{X}_p(t)$.and Rouse correlators $\Phi_p(t)$ have been already given in section 2.3.

Let us recall that according to the Rouse model, the correlators decay exponentially $\Phi_p(t) = \exp(-t/\tau_p)$, and the relaxation times scale as $\tau_p \sim (N/p)^2$. This is also the

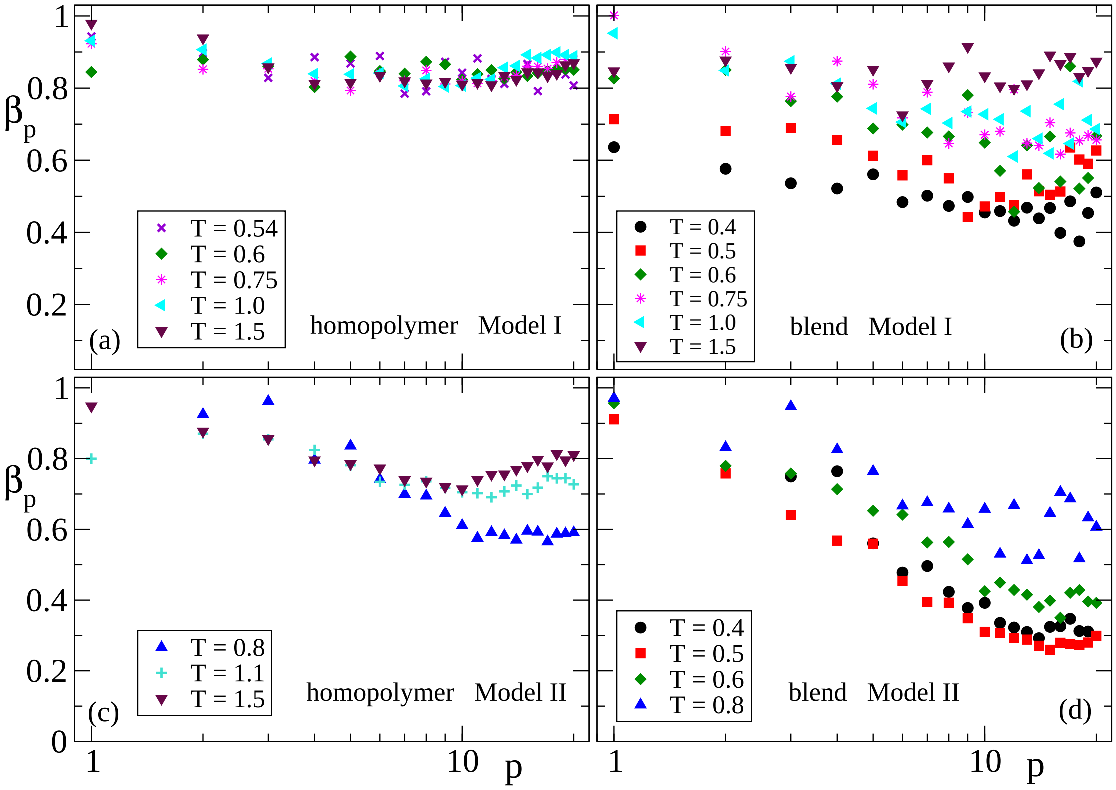

Figure 7.4: T- and p-dependence of the stretching exponents of the Rouse correlators for the B-chains (see text). The data in the left panels correspond to the fully-flexible (a) and semiflexible (c) B-homopolymer. The data in the right panels correspond to B-chains in the blend, for the models I (b) and II (d). The p-axis is represented in logarithmic scale for comparison with Figures 7.5 and 7.6.

scaling behaviour of the static amplitudes of the modes, $\langle X_p^2(0)\rangle \sim (N/p)^2$, which follows from the assumed gaussian model for the static intrachain correlations. In summary, according to the Rouse model $\tau_p \sim \langle X_p^2(0)\rangle \sim (N/p)^2$.

Figure 7.3 shows results of $\Phi_p(t)$ for semiflexible B-chains in the homopolymer state and in the blend (model II) at two selected low temperatures. The first decay, at short times, to the plateau reflects the onset of the caging regime already observed in the MSD. The second decay at long times reflects the relaxation of the corresponding p-mode. We analyze the latter by fitting the decay to a stretched exponential or Kohlrausch-Williams-Watts (KWW) function $\Phi_p(t) = A_p \exp[-(t/\tau_p)^{\beta_p}]$, with $A_p, \beta_p < 1$. The KWW time τ_p provides an estimation of the relaxation time of the p-mode. Figure 7.4 shows, at several temperatures, the stretching exponents β_p for the fully-flexible and semiflexible B-chains, both in the homopolymer and in the blend. The general trend displayed by the four panels is that stretching is enhanced both by the presence of intramolecular barriers and by blending. The data for the fully-flexible B-homopolymer (Figure 7.4a) are roughly T-independent and take values close to Rouse-like exponential behaviour $\beta_p = 1$ (see above). This is in agreement with observations in similar fully-flexible models [69]. A rather different behaviour is observed for the fully-flexible B-chains in the blend (Figure 7.4b). Exponential behaviour is only approached at high temperatures, in the limit of vanishing dynamic asymmetry. On decreasing temperature and increasing the dynamic asymmetry, the correlators exhibit stronger stretching, reaching values of even $\beta_p \sim 0.4$.

In principle, the observed non-exponentiality may be related to a distribution of intrinsically exponential processes originating from structural and/or dynamic heterogeneity. It is well-known that a KWW function can be, at least formally, expressed as a sum of pure exponential functions weighted by an adequate distribution G, though the latter does not necessarily have a physical meaning. Hence, we express the KWW function for the pth-mode as $\int d\tau_p^0 G(\tau_p^0) \exp[-t/\tau_p^0]$, where the distributed values τ_p^0 are the relaxation times of the different exponential Rouse modes. According to the Rouse model, these follow the p-scaling $\tau_p^0 = \xi\langle X_p^2(0)\rangle$, where the prefactor ξ is proportional to the p-independent friction constant [27]. Thus, if the observed stretching in the Rouse correlators essentially arises from a distribution of exponential Rouse-like processes, this reflects a distribution of friction terms $g(\xi)$. By simple mathematical transformation it is found [67] that the KWW time τ_p must follow the same scaling behaviour as the distributed Rouse times τ_p^0, i.e., $\tau_p \sim \langle X_p^2(0)\rangle$. Therefore, if this condition is fulfilled, stretching essentially arises from a distribution of exponential Rouse-like processes. Otherwise, though distribution effects can also be present, strong deviations from the scaling $\tau_p \sim \langle X_p^2(0)\rangle$ are the signature of a strong intrinsic non-exponential character of the mode relaxation. Analogous arguments have been applied, based on the scaling of the corresponding KWW times with the wave vector of the scattering functions, to solve the intrinsic non-exponential character of the α-relaxation associated to the glass transition [140].

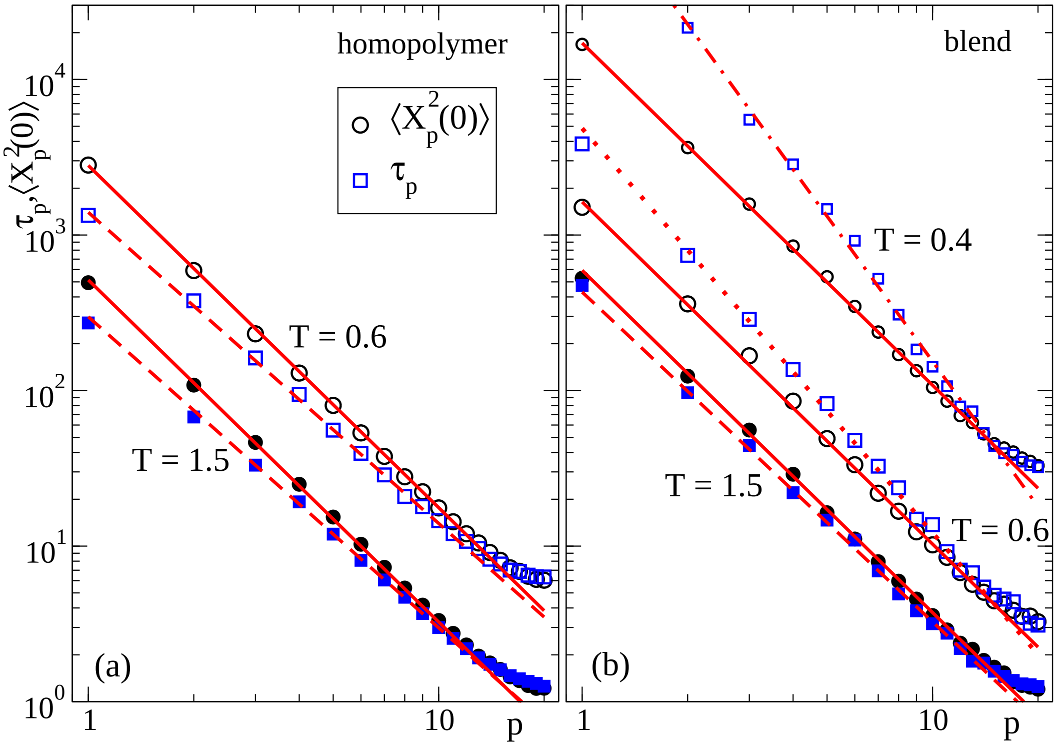

Figure 7.5: Squares and circles are respectively the relaxation times τ_p and the static amplitudes $\langle X_p^2(0)\rangle$ of the Rouse correlators for the fully-flexible B-chains. Panel (a): data for the fully-flexible B-homopolymer at $T = 0.6$ (empty symbols) and $T = 1.5$ (filled symbols). Panel (b): data for the fully-flexible B-chains in the blend, at $T = 0.4$ (small empty symbols), $T = 0.6$ (big empty symbols) and $T = 1.5$ (filled symbols). Units in the vertical axis are arbitrary. Each data set has been rescaled by a factor to facilitate comparison of τ_p and $\langle X_p^2(0)\rangle$ at common T. Solid lines in both panels are power laws with $x = 2.2$. Dashed lines are power laws with $x = 2.0$ in panel (a) and $x = 2.1$ in panel (b). The dotted ($T = 0.6$) and dashed-dotted ($T = 0.4$) lines in panel (b) are power laws with respectively $x = 2.7$ and $x = 3.3$.

Figure 7.5 shows results for the p-dependence of τ_p for the fully-flexible B-chains in the homopolymer and in the blend (Model I). The selected temperatures cover all the investigated range. We also include the amplitudes of the modes $\langle X_p^2(0)\rangle$, and rescale the data sets by arbitrary factors to facilitate comparison between dynamic and static quantities at the different temperatures. In agreement with similar fully-flexible models [69], relaxation times for the homopolymer are consistent with Rouse scaling, $\tau_p \sim p^{-2}$, and therefore the Rouse modes are essentially exponential. The observed dynamic Rouse scaling is consistent with the static scaling displayed by the amplitudes of the modes, $\langle X_p^2(0)\rangle \sim p^{-2.2}$, again in agreement with previous works [69] and very close to the ideal gaussian behaviour $\langle X_p^2(0)\rangle \sim p^{-2}$ expected within the Rouse model [27]. Thus, Rouse relaxation times and amplitudes for the homopolymer are roughly proportional, $\tau_p \sim \langle X_p^2(0)\rangle$, as already found in section 2.3 for the fully flexible homopolymer with $N = 10$.

The static scaling $\langle X_p^2(0)\rangle \sim p^{-2.2}$ observed in the fully-flexible B-homopolymer is not altered by blending at any investigated temperature (Figure 7.5b). On the contrary, dynamic Rouse scaling is observed in the blend only at high temperature. On decreasing temperature and increasing the dynamic asymmetry, a progressive deviation from the relation $\tau_p \sim \langle X_p^2(0)\rangle$ is observed. We describe the behaviour of the relaxation times by an effective power law $\tau_p \sim p^{-x}$, with x increasing on decreasing temperature, up to $x = 3.3$ for $T = 0.4$. Thus, dynamic asymmetry in the blend leads to an intrinsic strongly non-exponential character of the Rouse modes for the fully-flexible B-chains. Intrinsic non-exponentiality and the observed anomalous scaling for the relaxation times are not related to particular static features of the modes, which indeed are not affected by blending. The origin of the stretching of the Rouse correlators for the semiflexible B-chains [see panels (c) and (d) of Figure 7.4] will be discussed below.

Figure 7.6 shows results of τ_p and $\langle X_p^2(0)\rangle$ for the semiflexible B-chains in the homopolymer and in the blend (Model II), at temperatures covering all the investigated range. In analogy with the representation of Figure 7.5, we rescale the different data sets to facilitate comparison between times and amplitudes. This procedure yields a nice overlap of the latter for the B-homopolymer, and as in the fully-flexible case, the data follow the approximate relation $\tau_p \sim \langle X_p^2(0)\rangle$. These results are in agreement with those found for the semiflexible homopolymers with $N = 10$ discussed in section 2.3. The relation $\tau_p \sim \langle X_p^2(0)\rangle$ is also mantained for the semiflexible B-chains in the blend at high T and at the lowest $T = 0.4$ except for modes $p > 9$, corresponding to small wavelengths $N/p \lesssim 2.3$. However, it is noteworthy that the static data of Figure 7.6 follow a rather different p-dependence from the gaussian behaviour $\langle X_p^2(0)\rangle \sim p^{-2}$,

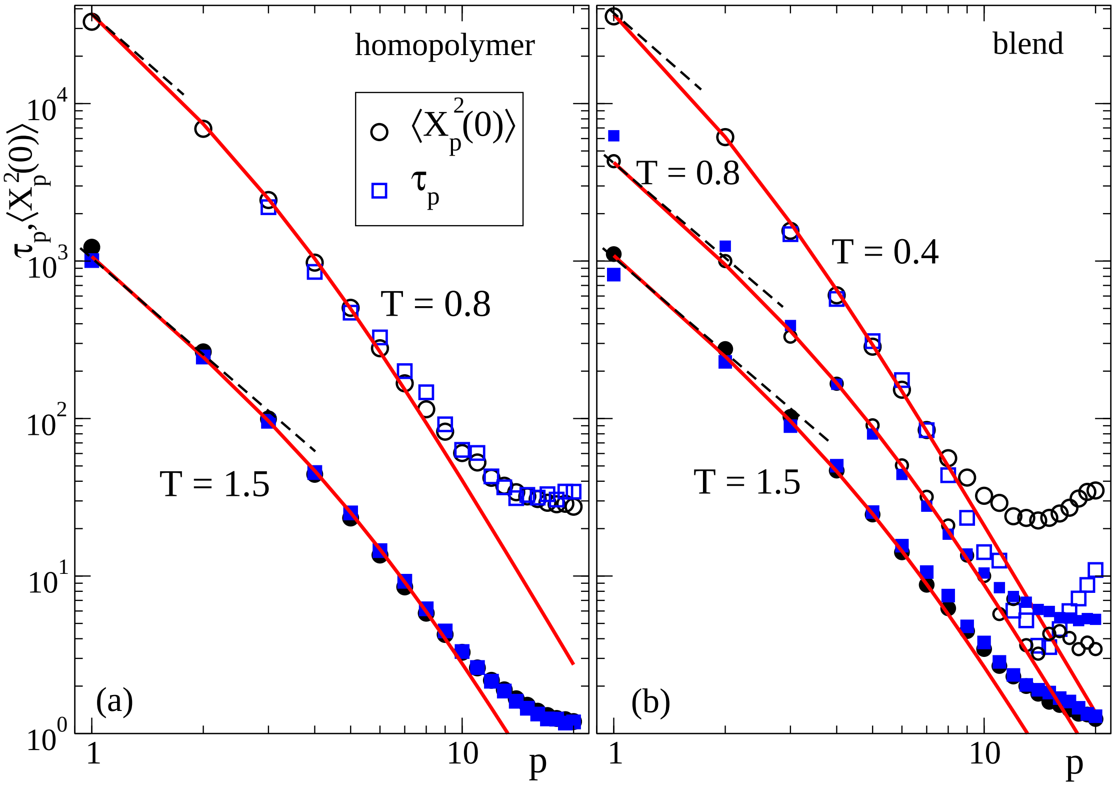

Figure 7.6: Squares and circles are respectively the relaxation times τ_p and the static amplitudes $\langle X_p^2(0)\rangle$ of the Rouse correlators for the semiflexible B-chains. Panel (a): data for the semiflexible B-homopolymer at $T = 0.8$ (empty symbols) and $T = 1.5$ (filled symbols). Panel (b): data for the semiflexible B-chains in the blend, at $T = 0.4$ (big empty symbols), $T = 0.8$ (small empty symbols) and $T = 1.5$ (filled symbols). Units in the vertical axis are arbitrary. Each data set has been rescaled by a factor to facilitate comparison of τ_p and $\langle X_p^2(0)\rangle$ at common T. Solid lines in both panels are fits to the Equation (7.5). Dashed lines represent Rouse-like behaviour $\tau_p, \langle X_p^2(0)\rangle \sim p^{-2}$.

which is only approached in the large scale limit $p \to 1$ at high T. This confirms the non-gaussian character of the semiflexible chains within all their length scale. Obviously, also the p-dependence of the times is very different from the scaling $\tau_p \sim p^{-2}$ predicted by the Rouse model. Let us recall that in chapter 2, we observed that the increase of the strength of the intramolecular barriers in semiflexible homopolymers, leads to progressive deviations from the Rouse scaling for $\langle X_p^2(0) \rangle$ and τ_p. However chains were too short, $N = 10$ monomers per chain, for recovering of the gaussian behaviour at large N/p.

As already discussed at the end of the section 5.2, deviations from the Rouse scaling observed for semiflexible polymers can be discussed in terms of a phenomenological Markovian model different from the Rouse model. Indeed, in the same spirit of the Rouse model for fully-flexible chains, other phenomenological models for semiflexible polymers, i.e. with intramolecular barriers, model the interactions of the tagged chain with the surroundings through a friction coefficient and random forces. Thus memory effects related to the slow fluctuation of the surrounding chains are neglected. Non-Rouse effects are of intramolecular origin, and amplitudes and relaxation times of the Rouse modes follow the same scaling behaviour. The behaviour of relaxation times τ_p and static amplitudes $\langle X_p^2(0) \rangle$ observed in Fig. 7.6 can be discussed in terms of the framework proposed in [54–56, 134, 135]. In this approach, the worm-like model [112] is assumed for the intramolecular correlations. In the worm-like model, positional fluctuations of the chain are not purely entropic like in the gaussian chain, but are governed by a bending energy U_{bend} and characterized by a persistence length L_p. The correspondig elastic energy takes the form:

$$U_{bend} = \frac{k}{2} \int_0^L ds \left(\frac{\partial^2 \mathbf{r}}{\partial s^2} \right)^2 \tag{7.1}$$

where L is the contour length, and depends on the local curvature of the contour s. In our model $L = Nb$ where b is the bond lenght. $\mathbf{r}(s)$ is the position vector of a monomer on the chain and k is the elastic constant. By applying the Hamiltonian principle together with constraints on the contour length L and on the curvature of the chain, Harnau and co-workers obtained the following Langevin equation for the worm-like chain:

$$\zeta \frac{\partial \mathbf{r}(s,t)}{\partial t} = \frac{3k_BT}{2L_p} \frac{\partial^2 \mathbf{r}(s,t)}{\partial s^2} - \frac{3k_BTL_p}{2} \frac{\partial^4 \mathbf{r}(s,t)}{\partial s^4} + \mathbf{f}^s(s,t) \tag{7.2}$$

with a friction coefficient ζ and Gaussian stochastic forces $\mathbf{f}^s(s,t)$. Eq.7.2 is essentially based on the Rouse model for Gaussian flexible chains and the introduced bending term can be considered as a small and local perturbation to the system. Therefore, in the limit of $L_p << L$, Rouse modes (Eq. 2.19) still represent a good base of orthogonal modes, to solve eq. 7.2. The Langevin equation for the normal modes now reads:

$$\zeta_p \frac{\partial \mathbf{X}_p(t)}{\partial t} = k_p^{semi} \mathbf{X}_p(t) + \mathbf{g}_p^s(t) \tag{7.3}$$

where $\zeta_p = 2L\zeta$ and the effective force constant is the sum of the bending and entropic tension contribution:

$$k_p^{semi} = k_p^b + k_p = \frac{3k_B T L_p \pi^4}{L^3} + \frac{3k_B T \pi^2 p^2}{L L_p} \tag{7.4}$$

Solutions of eq. 7.3 lead to a modified p-dependence of the amplitudes and relaxation times of the normal modes, but as in the case of the Rouse modes, they are still proportional:

$$\tau_p \sim \langle X_p^2(0) \rangle \sim \left[p^2 + \gamma p^4\right] \tag{7.5}$$

where $\gamma = \pi^2 L_p / N^2 b^2$ is a parameter quantifying chain stiffness and L_p is the persistence length of the chain. Recent simulation results by Steinhauser and co-workers [54,55] on semiflexible homopolymers are in good agreement with Equation (7.5). On the basis of this result, we use it for describing the data sets of Figure 7.6. Instead of using different definitions of the persistence length proposed in the literature (see e.g., Ref. [141]) as input, we just obtain L_p as a fit parameter. At each temperature, this is forced to be identical for $\langle X_p^2(0) \rangle$ and τ_p, to be consistent with the relation $\tau_p \sim \langle X_p^2(0) \rangle$. The obtained values of the persistence length change from $L_p \sim 1.2$ at high temperatures to $L_p \sim 3$ at the lowest investigated T in the blend. Equation (7.5) provides a good description of the data of Figure 7.6 in the region $p < 9$, both for the B-homopolymer and for the B-chains in the blend. The behaviour at smaller wavelengths ($p \geq 9$, $N/p \lesssim 2.3$) cannot be captured. Presumably this is mostly due to the influence of the torsional terms. The latter are not accounted for within the approach of Refs. [54–56,134,135] based on the worm-like model for the intramolecular interactions, which only includes bending terms.

7.4 Discussion

As shown in the previous section, the results presented in Figures 7.5 and 7.6 for the B-homopolymers are consistent with the approximate relation $\tau_p \sim \langle X_p^2(0)\rangle$, the specific p-dependence being distinct for fully-flexible and semiflexible chains. The latter is Rouse-like for fully-flexible chains, $\tau_p \sim p^{-2}$, and is well described by Equation (7.5) for semiflexible chains. Since the relation $\tau_p \sim \langle X_p^2(0)\rangle$ is fulfilled, the anomalous (in the meaning of non-Rouse) scaling of the relaxation times for the semiflexible homopolymers is essentially of static origin. More specifically, it is a direct consequence of the non-gaussian nature of the static intramolecular correlations. This is also the case for the semiflexible B-chains in the blend (Model II), for which $\tau_p \sim \langle X_p^2(0)\rangle$ is maintained, except for short wavelengths ($N/p \lesssim 2.3$, see Figure 7.6b) at low temperatures.

According to the approach of Refs. [54–56, 134, 135] for semiflexible chains, the Rouse correlators $\Phi_p(t)$ decay, as in the Rouse model, exponentially. Following the same argumentation as for the fully-flexible case (see Section 7.3), stretching in $\Phi_p(t)$ arises from a distribution of the predicted exponential processes if the KWW times fulfill the relation $\tau_p \sim \langle X_p^2(0)\rangle$. Otherwise non-exponentiality is intrinsic. Thus, from data in Figure 7.6, we conclude that non-exponentiality of the Rouse modes of the semiflexible chains is intrinsinc only for short wavelengths, in the blend state and at low temperature.

As shown by the data in Figure 7.2b, the dynamic asymmetry ($\chi \approx 68$) at the lowest investigated $T = 0.4$ of the Model II, is slightly higher than that of the Model I at $T = 0.6$ ($\chi \approx 63$). Though the strength of the confinement is essentially the same in both cases, the origin of anomalous chain dynamics seems to be very different. As discussed above, this is of intramolecular and static nature for the semiflexible B-chains of Model II. On the contrary, the origin is essentially dynamic for the fully-flexible B-chains of Model I, as indicated by the clear breakdown of the relation $\tau_p \sim \langle X_p^2(0)\rangle$. As shown in Figure 7.5b, we find strongly non-Rouse scaling for the times, $\tau_p \sim p^{-x}$ with $x = 2.7$, considerably *larger* than the exponent $x = 2.2$, close to gaussian behaviour, found for the amplitudes. Note that for the homopolymer we find a, Rouse-like, dynamic exponent $x = 2.0$ similar but *smaller* than the static $x = 2.2$ (Figure 7.5a).

As mentioned in the Section 2.3, within the Rouse model memory effects, related to slow density fluctuations of the matrix around the tagged chain, are neglected. The interactions of the tagged (gaussian) chain with the surroundings are simply modelled by a friction term and random forces [27]. This Markovian approximation is also followed by the approach of Harnau and co-workers [54–56, 134, 135], which just incorporates bending forces in the Rouse equations of motion to account for chain stiffness. The predicted scaling behaviour [Equation (7.5)] is observed for the semiflexible B-homopolymer and is not signifficantly affected by blending with a slower matrix, suggesting that memory effects are not relevant and the Markovian approximation can still be applied in the blend. As discussed above, the observed stretching of the Rouse correlators for the semiflexible B-chains in the blend essentially reflects a distribution of elementary exponential processes. It remains to be understood, from a microscopic basis, why memory effects induced by the matrix are apparently much weaker than intramolecular effects induced by the presence of the barriers. On the contrary, memory effects are crucial in the case of the fully-flexible B-chains in the blend [67], for which predictions of the Rouse model are strongly violated, and non-exponentiality is intrinsic.

Finally, we want to make a last remark on the dynamics of the semiflexible chains in the blend. As discussed above, the semiflexible chains considered here are strongly non-gaussian within all chain length scales. If longer chains were considered, with the same torsional and bending contributions, the semiflexible character would be lost beyond some mode wavelength, and gaussian statistics would be recovered for intrachain static correlations at large length scales (small p-values). We expect that in such length scales, as observed for the fast fully-flexible chains in blends with strong dynamic asymmetry, anomalous dynamic scaling will arise for the Rouse modes, distinct from the static gaussian scaling, and memory effects will be relevant. In fact this seems to be the case for the results reported in Ref. [64] from atomistic simulations of the dynamically asymmetric blend PEO/PMMA. There the relaxation times τ_p of the Rouse mode correlators of the fast component (PEO) still exhibit anomalous, non-Rouse, p-scaling at large mode wavelengths N/p for which gaussian behaviour, $\langle X_p^2(0)\rangle \sim (N/p)^2$, is recovered in the mode amplitudes (see Figure 11 in Ref. [64]). This would be the general expected behaviour in real blends with strong dynamic asymmetry.

Chapter 8

Conclusions

By means of simulations and solution of the equations of the Mode Coupling Theory, we have studied the role of intramolecular barriers, of arbitrary strength, on several aspects of polymer dynamics. The investigated dynamic range extends from the caging regime characteristic of glass-formers to the relaxation of the chain Rouse modes. In order to investigate the decisive role of intramolecular barriers on the glass transition of polymer melts, density-density correlators and relaxation times have been computed from simulations and analyzed in the framework of the Mode Coupling Theory (MCT) of the glass transition. This is justified, since the quality of the specific static approximations invoked by MCT for polymer melts, based on the polymer reference interaction site model (PRISM), are not affected by the introduction of the intramolecular barriers.

Critical nonergodicity parameters, critical temperatures and dynamical exponents of the theory have been obtained from consistent fits of the simulation data to the MCT asymptotic laws. From the analysis of the critical nonergodicity parameters we deduce that the presence of the barriers induces a weaker localization length in the system at fixed density. The increase of the barrier strength at fixed density induces also a higher critical temperature T_c, as well as a longer relaxation time for fixed density and temperature. The values of the dynamical exponents, as obtained from the MCT analysis of the simulation data, exhibit significant differences between the limit of fully flexible (with zero values of the internal barriers) and stiff chains. In particular the so-called exponent parameter λ takes standard values $\lambda \sim 0.7$ for the fully-flexible case and values approaching the upper limit $\lambda = 1$ for high values of the internal barriers. While the former λ-values are characteristic of systems dominated by packing effects, transitions with $\lambda \approx 1$ arise in systems with different competing mechanisms for dynamic arrest. In our systems these large values of λ suggest competition between two distinct mechanisms: general packing effects and polymer-specific intramolecular barriers.

The results of the simulation data analysis have been compared with the numerical solutions of the MCT equations for polymer melts. We observed that solutions of MCT for the structural relaxation reproduce qualitative trends of simulations for weak and moderate barriers. However, a progressive discrepancy between MCT and simulations is revealed as the limit of stiff chains is approached. We have tested the validity of several assumptions inherent to the theory. Deviations from the theoretical predictions do not seem related with dynamic heterogenities, which indeed are not enhanced by increasing the barrier strength. Moreover, the convolution approximation for three-point static correlations retains its validity for stiff chains. Even the role of slow modes at intermediate length scales, not accounted for by MCT, becomes less significant on increasing chain stiffness. At this point it is not clear how to improve the MCT equations in order to remove the mentioned discrepancies for the case of stiff chains. We have suggested the possibility of formulating the MCT equations in terms of roto-translational density fluctuations over specific length scales.

Concerning the relaxation of the chain degrees of freedom, we have analyzed simulation data in the framework of the Rouse model. We found that simulation data showed progressive deviations from the Rouse predictions. These include anomalous scaling of Rouse relaxation times, long-time plateaux, and non-monotonous wavelength dependence of the Rouse mode correlators. We solved the MCT equations of motion for the Rouse mode correlators and found that MCT solutions are in semiquantitative agreement with anomalous trends of simulations, with similar exponents for the effective power laws. Thus MCT provides a microscopic basis for the observed deviations from the Rouse model on increasing the barrier strength. Beyond usual phenomenological models for chain dynamics (the Rouse model being the corresponding one for fully-flexible chains), MCT provides a unified microscopic picture down to time scales around and before the α-process, which is not accounted for within the mentioned models.

We have also performed simulations of the bead-spring model with tunable intramolecular barriers blended with a slower component. Extending previous investigations for fully-flexible chains, we investigate the effect of the dynamic asymmetry in the blend on the relaxation of the semiflexible chains. We find the same anomalous scaling behaviour for the relaxation times and the static amplitudes of the Rouse modes, in agreement with Markovian models which extend the Rouse equations by the introduction of bending forces. Thus, anomalous dynamic features for the semiflexible chains essentially have a static and intramolecular origin. This is very different from the case of fully-flexible chains in blends with similar dynamic asymmetry. For the latter anomalous dynamic scaling is strongly correlated with the dynamic asymmetry, and not to features of the static amplitudes, which indeed still follow gaussian scaling.

The former results suggest that memory effects induced by the surrounding slow matrix in the blend are not relevant for non-entangled semiflexible polymers, and Markovian models can still be applied. However, if the chains are long enough, we expect that the influence of the memory effects will be recovered at large length scales where intrachain static correlations recover gaussian statistics.

Appendices

Appendix A

MCT: Schematic Derivation

In this appendix we schematically summarize the derivation of the equations of motion of the Mode Coupling Theory within the Mori-Zwanzig formalism. Detailed expositions can be found in extensive reviews in Refs. [4–8]

Le us consider a classical observable $A = A(\mathbf{r}_1, \mathbf{r}_2, ..., \mathbf{r}_N, \mathbf{p}_1, \mathbf{p}_2, ..., \mathbf{p}_N)$, being a function of the coordinates and momenta of an N-particle system. The equation of motion for A is given by:

$$i\mathcal{L}A(t) = \dot{A}(t) \tag{A.1}$$

where $\mathcal{L}$ is the hermitian *Liouville operator*, defined by:

$$i\mathcal{L} = \sum_i \left(\frac{\mathbf{p}_i}{m} \cdot \frac{\partial}{\partial \mathbf{r}_i} - \sum_j \frac{\partial V(\mathbf{r}_{ij})}{\partial \mathbf{r}_j} \cdot \frac{\partial}{\partial \mathbf{p}_i} \right) \tag{A.2}$$

and $V(\mathbf{r}_{ij}) = V(\mathbf{r}_i - \mathbf{r}_j)$ is the interaction potential between the particles. The set of all possible observables form a vector space and one can define a scalar product on the phase space via

$$(A|B) \equiv \langle A^* B \rangle \tag{A.3}$$

where $\langle ... \rangle$ denotes ensemble average. Now consider the *projection operator* $\mathcal{P}$

$$\mathcal{P} \equiv (A|...)(A|A)^{-1}A \tag{A.4}$$

If A is a vector itself, $(A|A)^{-1}$ is its inverse modulus. In geometrical terms the projection operator projects and arbitrary observable B on the space spanned by A. If we define the operator $\mathcal{Q} = 1 - \mathcal{P}$, it is easy to see that $\mathcal{Q}$ projetcs B on to the subspace orthogonal to A. From equation (A.1) it follows that the time dependence of A is given by $A(t) = \exp(i\mathcal{L}t)A(0)$. Inserting the identity operator $\mathcal{P} + \mathcal{Q}$ after the propagator $\exp(i\mathcal{L}t)$ and differentiating with respect to t we find

$$\dot{A}(t) = i\Omega A(t) + e^{i\mathcal{L}t}(1 - \mathcal{P})\dot{A}(0) \tag{A.5}$$

with $i\Omega = \frac{\langle A^*(0)\dot{A}(0)\rangle}{\langle A^*(0)A(0)\rangle}$. The last term in (A.5) can be written as

$$e^{i\mathcal{L}t}(1 - \mathcal{P})\dot{A}(0) = f(t) + \int_0^t dt' e^{i\mathcal{L}t'}\mathcal{P}i\mathcal{L}f(t - t') \tag{A.6}$$

with $f(t) = e^{i(1-\mathcal{P})\mathcal{L}t}(1 - \mathcal{P})\dot{A}(0)$. The function $f(t)$ is the result of projecting $\dot{A}(0)$ onto the subspace orthogonal to A(0) and propagating the result within that subspace. By construction $\langle A^*(0)f(t)\rangle = 0$ and $(1-\mathcal{P})f(t) = f(t)$, i.e., $f(t)$ is *always* orthogonal to $A(0)$. The function $f(t)$ is called the *fluctuating force*.

Using in Eq. (A.6) the relations $\mathcal{P}\mathcal{L}f(t) = (A|\mathcal{L}f(t))(A|A)^{-1}A$ and $\langle A^*(0)i\mathcal{L}f(t - t')\rangle = -\langle f^*(0)f(t - t')\rangle$, we obtain for the equation of motion (A.5) the following expression

$$\dot{A}(t) = i\Omega A(t) + f(t) - \int_0^t dt' K(t - t')A(t') \tag{A.7}$$

where we have introduced the memory function

$$K(t - t') = \frac{\langle f^*(0)f(t - t')\rangle}{\langle A^*(0)A(0)\rangle} \tag{A.8}$$

Thus the equation of motion for A has been trasformed into a generalized Langevin equation with $f(t)$ playing the role of the fluctuating force and the relation (A.8) is just the expression for the fluctuation-dissipation theorem.

To obtain an equation of motion for the time correlation function $C(t) = \langle A^*(0)A(t)\rangle = (A|A(t))$, we take the scalar product of Eq. (A.7) with A and use the fact that $(A|f(t)) = 0$:

$$\dot{C}(t) = i\Omega C(t) - \int_0^t dt' K(t - t')C(t') \tag{A.9}$$

This is the so-called ”memory equation”. It is exact since no approximations have been made till now. The problem with solving equation A.9 is embodied in the difficulty of determining the memory function $K(t)$. Let us now turn our attention to the case of supercooled liquids. For this type of systems the observables of interest are $\rho_{\mathbf{q}}(t)$, the fluctuations in density for wave vector $\mathbf{q}$, and hence the mode-coupling equations are equations of motion for the corresponding correlation function, the density-density correlator $F(q,t)$:

$$\rho_{\mathbf{q}}(t) = \sum_i e^{i\mathbf{q}\cdot\mathbf{r}_i(t)} \qquad \text{and} \qquad F(q,t) = \frac{1}{N}\langle \rho_{-\mathbf{q}}(0)\rho_{\mathbf{q}}(t)\rangle \tag{A.10}$$

Let us introduce the current related to the fluctuations of density by the continuity equation:

$$\dot{\rho}_{\mathbf{q}}(t) = \mathbf{q}\cdot\sum_i \frac{\mathbf{p}_i}{m} e^{i\mathbf{q}\cdot\mathbf{r}_i(t)} = i\mathbf{q}\cdot\boldsymbol{\Upsilon}_{\mathbf{q}} = iq\Upsilon^L_{\mathbf{q}} \tag{A.11}$$

where $\Upsilon^L_{\mathbf{q}}$ is the *longitudinal* current (the projection of the current onto $\mathbf{q}$).

We introduce the observable $\quad A = \begin{pmatrix} \rho_{\mathbf{q}} \\ \Upsilon^L_{\mathbf{q}} \end{pmatrix}$

The correlation function $C(t)$, is now a correlation matrix $C_{ij}(t) = \langle A^*_i(0)A_j(t)\rangle$:

$$C(t) = \begin{pmatrix} \langle \rho_{-\mathbf{q}}(0)\rho_{\mathbf{q}}(t)\rangle & \langle \rho_{-\mathbf{q}}(0)\Upsilon^L_{\mathbf{q}}(t)\rangle \\ -\langle \Upsilon^L_{-\mathbf{q}}(0)\rho_{\mathbf{q}}(t)\rangle & -\langle \Upsilon^L_{-\mathbf{q}}(0)\Upsilon^L_{\mathbf{q}}(t)\rangle \end{pmatrix}$$

We now evaluate the frequency matrix $i\Omega = \frac{\langle A^*(0)\dot{A}(0)\rangle}{\langle A^*(0)A(0)\rangle} = \dot{C}(0)C^{-1}(0)$. First of all we note that the first element in the diagonal of the correlation matrix evalutated at $t = 0$ is $C_{11}(0) = NS(q)$, where $S(q) = \frac{1}{N}\langle \rho_{-\mathbf{q}}(0)\rho_{\mathbf{q}}(0)\rangle = F(q, t = 0)$ is the static structure factor. The off-diagonal elements of the correlation matrix $C(0)$ are zero. This easily demonstrated. From Eq. (A.11) we have that $C_{12}(0) = -(i/q)\langle \rho_{-\mathbf{q}}(0)\dot{\rho}_{\mathbf{q}}(0)\rangle = -(i/q)\dot{F}(q,0)$. Since $F(q,t)$ must be time-reversible, $C_{12}(0) = 0$. Analogously $C_{21}(0) = 0$. By using Eq. (A.11) and the equipartition theorem $\langle \sum_i p_i^2(0)\rangle = 3mNk_BT$ we find that the second diagonal element of the matrix $C(0)$ is $C_{22}(0) = Nk_BT/m$. With a similar procedure we find that the derivative of the correlation matrix evalutated at time $t = 0$ is:

$$\dot{C}(0) = \langle A^*(0)\dot{A}(0)\rangle = \begin{pmatrix} 0 & iNk_BT/m \\ iNk_BT/m & 0 \end{pmatrix}$$

The frequencies matrix now reads:

$$i\Omega = \begin{pmatrix} 0 & iq \\ \frac{iqk_BT}{mS(q)} & 0 \end{pmatrix}$$

The fluctuating force can now be expressed as a vector $f(t) = \begin{pmatrix} 0 \\ R_{\mathbf{q}}(t) \end{pmatrix}$

where $R_{\mathbf{q}}(t) = \dot{\Upsilon}^L_{\mathbf{q}}(t) - \frac{iqk_BT}{mS(q)}\rho_{\mathbf{q}}(t)$.

The memory matrix is therefore $K(t-t') = \begin{pmatrix} 0 & 0 \\ 0 & \frac{m\langle R_{-\mathbf{q}}(0)R_{\mathbf{q}}(t)\rangle}{Nk_BT} \end{pmatrix}$

For the time derivative of the correlation matrix we have the following expression:

$$\dot{C}(t) = \begin{pmatrix} \langle \rho_{-\mathbf{q}}(0)\dot{\rho}_{\mathbf{q}}(t)\rangle & \langle \rho_{-\mathbf{q}}(0)\dot{\Upsilon}^L_{\mathbf{q}}(t)\rangle \\ -\langle \Upsilon^L_{-\mathbf{q}}(0)\dot{\rho}_{\mathbf{q}}(t)\rangle & -\langle \Upsilon^L_{-\mathbf{q}}(0)\dot{\Upsilon}^L_{\mathbf{q}}(t)\rangle \end{pmatrix}$$

We concentrate on the term $\dot{C}_{21}(t) = -\langle \Upsilon^L_{-\mathbf{q}}(0)\dot{\rho}_{\mathbf{q}}(t)\rangle$. From Eq. (A.11) and recalling that $\rho^*_{\mathbf{q}} = \rho_{-\mathbf{q}}$ and $(\Upsilon^L_{\mathbf{q}})^* = -\Upsilon^L_{-\mathbf{q}}$ we find that $\dot{C}_{21}(t) = (i/q)\langle \dot{\rho}_{-\mathbf{q}}(0)\dot{\rho}_{\mathbf{q}}(t)\rangle = q^{-1}\langle [\mathcal{L}\rho_{-\mathbf{q}}(0)]^*\dot{\rho}_{\mathbf{q}}(t)\rangle$ Recalling that the Liouville operator $\mathcal{L}$ is Hermitian we have that $\dot{C}_{21}(t) = -(i/q)\langle \rho_{-\mathbf{q}}(0)i\mathcal{L}\dot{\rho}_{\mathbf{q}}(t)\rangle = -(i/q)\langle \rho_{-\mathbf{q}}(0)\ddot{\rho}_{\mathbf{q}}(t)\rangle$. Therefore the element $\dot{C}_{21}(t)$ of the correlation matrix can be expressend in terms of the density-density correlator:

$$\dot{C}_{21}(t) = \frac{N}{iq}\ddot{F}(q,t) \tag{A.12}$$

Now we can determine the explicit form of the integro-differential equation for $\dot{C}_{21}(t)$. Recalling Eq. (A.9) we have:

$$\dot{C}_{21}(t) = [i\Omega C(t)]_{21} - \int_0^t dt'[K(t-t')C(t')]_{21} \tag{A.13}$$

By using the explicit expression for the frequency, correlation, and memory matrix that we have previously determined, we have :

$$[i\Omega C(t)]_{21} = \frac{iqNK_BT}{mS(q)}F(q,t) \qquad \text{and} \qquad [K(t-t')C(t')]_{21} = K_{22}(t-t')C_{21}(t') \quad (A.14)$$

By following argumets as those used for determining Eq. (A.12), we find:

$$C_{21}(t) = \frac{N}{iq}\dot{F}(q,t) \qquad \text{and} \qquad [K(t-t')C(t')]_{21} = \frac{m}{iqK_BT}\langle R_{-\mathbf{q}}(0)R_{\mathbf{q}}(t-t')\rangle\dot{F}(q,t') \quad (A.15)$$

Finally inserting Eq.(A.12), Eq. (A.14), Eq. (A.15) in Eq. (A.13) we arrive at the following integro-differential equation for the density-density correlator:

$$\ddot{F}(q,t) + \frac{q^2k_BT}{mS(q)}F(q,t) + \frac{m}{Nk_BT}\int_0^t dt'\langle R_{-\mathbf{q}}(0)R_{\mathbf{q}}(t-t')\rangle\dot{F}(q,t') = 0 \quad (A.16)$$

This equation is exact, but however is not yet solvable and we need to introduce approximations for the memory term $\langle R_{-\mathbf{q}}(0)R_{\mathbf{q}}(t-t')\rangle$.

Let us rewrite the term $R_{-\mathbf{q}}$ of the memory function in terms of the Fourier components of the potential $V(\mathbf{r}_{ij})$. From Eq. (A.11)we have:

$$R_{\mathbf{q}}(t) = \dot{\Upsilon}^L_{\mathbf{q}}(t) - \frac{iqk_BT}{mS(q)}\rho_{\mathbf{q}}(t) = \sum_i \frac{\hat{\mathbf{q}}\cdot\dot{\mathbf{p}}_i(t)}{m}e^{i\mathbf{q}\cdot\mathbf{r}_i(t)} + \frac{iq}{m^2}\sum_i(\hat{\mathbf{q}}\cdot\mathbf{p}_i(t))^2e^{i\mathbf{q}\cdot\mathbf{r}_i(t)} - \frac{iqk_BT}{mS(q)}\rho_{\mathbf{q}}(t) \quad (A.17)$$

Recalling that $\dot{\mathbf{p}}_i(t) = -\sum_j \frac{\partial V(\mathbf{r}_{ij}(t))}{\partial \mathbf{r}_j(t)}$ and $\rho_{\mathbf{q}} = \sum_i e^{i\mathbf{q}\cdot\mathbf{r}_i(t)}$, and expressing the potential $V(\mathbf{r})$ in Fourier components: $V(\mathbf{r}) = (2\pi)^{-3}\sum_{\mathbf{k}} V_{\mathbf{k}}e^{-i\mathbf{k}\cdot\mathbf{r}}$, we obtain: $R_{\mathbf{q}}(t) = R^0_{\mathbf{q}}(t) + R^1_{\mathbf{q}}(t)$ with:

$$R^0_{\mathbf{q}}(t) = \frac{iq}{m^2}\sum_i(\hat{\mathbf{q}}\cdot\mathbf{p}_i(t))^2e^{i\mathbf{q}\cdot\mathbf{r}_i(t)} - \frac{iqk_BT}{mS(q)}\rho_{\mathbf{q}}(t) \quad \text{and} \quad R^1_{\mathbf{q}}(t) = \frac{i(2\pi)^3}{m}\sum_{\mathbf{k}}(\hat{\mathbf{q}}\cdot\mathbf{k})V_{\mathbf{k}}\rho_{\mathbf{q}-\mathbf{k}}\rho_{\mathbf{k}} \quad (A.18)$$

Near the transition point, the term $R^1_{\mathbf{q}}(t)$ is much slower than $R^0_{\mathbf{q}}(t)$. Thus the memory function $\langle R_{-\mathbf{q}}(0)R_{\mathbf{q}}(t-t')\rangle$ will be dominated by the correlation functions of the mode pairs $\rho_{\mathbf{q}-\mathbf{k}}\rho_{\mathbf{k}}$: $\langle\rho_{\mathbf{k}-\mathbf{q}}(0)\rho_{-\mathbf{k}}(0)\rho_{\mathbf{q}-\mathbf{k}}(t-t')\rho_{\mathbf{k}}(t-t')\rangle$.

Appendix B

MCT: Solution of the Equations of Motion

The MCT equations of motion for the normalized density-density correlator $f(q,t)$ read:

$$\ddot{f}(q,t) + \Omega^2(q) f(q,t) + \Omega^2(q) \int_0^t dt' m(q,t-t') \dot{f}(q,t') = 0 \tag{B.1}$$

where $\Omega^2(q) = (mS(q))^{-1} q^2 k_B T$. Let us rewrite the memory kernel $m(q,t-t')$ as $M(q,t-t') = \Omega^2(q) m(q,t-t')$. Eq. B.1 represents a set N coupled integro-differential equations, with wave vectors discretized to N values. The equations were numerically solved by following the scheme of [142]. We solved the problem with $N = 300$ values of q in the range $0 \leq q \leq 60$. Equation B.1 can be discretized in the time domain with $t_i = i * \delta t$, $i \in \mathbb{N}$ and integrals are estimated as Rienmann sums. We will use the notation $f(q,t_i) = f_{qi}$ and $M(q,t_i) = M_{qi}$ in the following.

Time-domain integrals , involving the memory kernel in eq. B.1 are discretized using the following approximation: we split the integral at some intermediate time $\bar{t} \in \delta \cdot \mathbb{N}$, $0 < \bar{t} = \bar{i}\delta t < t$, and use partial integration in the first term to get:

$$\int_0^{t_i} M(q,t-t') \dot{f}(q,t') dt' = \sum_{k=1}^{\bar{i}} \int_{t_{k-1}}^{t_k} \left[\partial_t M(q,t-t')\right] f(q,t') dt'$$
$$+ \sum_{k=1}^{i-\bar{i}} \int_{t_{k-1}}^{t_k} M(q,t') \left[\partial_t f(q,t-t')\right] dt' + M(q,t-\bar{t}) f(q,\bar{t}) - M(q,t) f(q,0) \tag{B.2}$$

Time derivatives in eq. B.2 can be estimated by means of the mean value theorem of calculus:

$$\int_0^{t_i} M(q,t-t')\dot{f}(q,t')dt' = \sum_{k=1}^{\bar{i}}(M_{q,i-k+1} - M_{q,i-k})df_k$$
$$+\sum_{k=1}^{i-\bar{i}} dM_k(f_{q,i-k+1} - f_{q,i-k}) + M_{q,i-\bar{i}}f_{q,\bar{i}} - M_{q,i}f_{q,0} \tag{B.3}$$

where we have introduced the so-called moments

$$df_k = \frac{1}{\delta t}\int_{t_{k-1}}^{t_k} f(q,t')dt' \tag{B.4}$$

The second order derivative in Eq. B.1 is approximated by a differentiation of an interpolation polynomial [143]:

$$\ddot{f}_{q,t_i} = \frac{2f_{q,i} - 5f_{q,i-1} + 4f_{q,i-2} - f_{q,i-3}}{\delta t^2} \tag{B.5}$$

With all these ingredients we can now write down the discrete version of Eq. B.1. The value of $f_{q,i}$ can be obtained knowing the values of $f_{q,j}$, $M_{q,j}$, df_j and dM_j at all $j < i$. Rearranging all the terms, we can rewrite Eq. B.1 as:

$$A_q f_{q,i} = C_{q,i} \tag{B.6}$$

where A_q and $C_{q,i}$ read like:

$$A_q = \frac{2}{\delta t^2} + \Omega^2(q) + dM_1 \tag{B.7}$$

$$C_{qi} = M_{q,i}(f_{q,0} - df_1) + \frac{5f_{q,i-1} - 4f_{q,i-2} + f_{q,i-3}}{\delta t^2} + dM_1 f_{q,i-1} + M_{q,i-1}df_1$$
$$+M_{q,i-\bar{i}}f_{q,\bar{i}} - \sum_{k=2}^{i-\bar{i}} dM_k\left(f_{q,i-k+1} - f_{q,i-k}\right)$$
$$-\sum_{k=2}^{\bar{i}} df_k\left(M_{q,i-k+1} - M_{q,i-k}\right) \tag{B.8}$$

Finally from Eq. B.6 we can obtain the solution of the MCT equations B.1 at time t_i as:

$$f_{q,i} = A_q^{-1} C_{q,i} \tag{B.9}$$

Eq. B.6 is solved by an iterative procedure with the following criterion for convergence $|f_{q,i} - f_{q,i-1}| < 10^{-10}$. Once the solution for the normalized density-density correlator $f(q,t)$ has been determined with numerical accuracy it can be used to calculate the self-density correlator $f^s(q,t)$ and the Rouse mode correlators $C_{pq}(t)$ (see Chapter 3) with an analog iterative procedure.

Bibliography

[1] C.A. Angell, J. Non-Cryst. Solids, **73**, 1 (1985)

[2] P.G. Debenedetti, *Metastable Liquids*, (Princeton University Press, Princeton, 1996).

[3] A. Tölle, Rep. Prog. Phys. **64**, 1473 (2002).

[4] W. Götze and L. Sjögren, Rep. Prog. Phys. **55**, 241 (1992).

[5] W. Götze, J. Phys.: Condens. Matter **11**, A1 (1999).

[6] W. Götze, in *Complex Dynamics of Glass-Forming Liquids: A Mode Coupling Theory* (Oxford Univ Press, New York, 2009)

[7] D. R. Reichman and P. Charbonneau, J. Stat. Mech., P05013 (2005).

[8] S.P. Das, Rev. Mod. Phys. **76**, 785 (2004).

[9] K. Binder and W. Kob, *Glassy Materials and Disordered Solids*, (World Scientific, Singapore, 2005).

[10] A. Cavagna, Phys. Rep. **476**, 51 (2009).

[11] S.-H. Chong, A.J. Moreno, F. Sciortino, W. Kob, Phys. Rev. Lett. **94**, 215701 (2005).

[12] K.N. Pham, A.M. Puertas, J. Bergenholtz, S.U. Egelhaaf, A. Moussaïd, P.N. Pusey, A.B. Schofield, M.E. Cates, M. Fuchs, W.C.K. Poon, Science **296**, 104 (2002).

[13] G. Foffi, F. Sciortino, P. Tartaglia, E. Zaccarelli, F. Lo Verso, L. Reatto, K.A. Dawson, C.N. Likos, Phys. Rev. Lett. **90**, 238301 (2003).

[14] F. Lo Verso, L. Reatto, G. Foffi, P. Tartaglia, K.A. Dawson, Phys. Rev. E **70**, 061409 (2004).

[15] C. Mayer, F. Sciortino, C.N. Likos, P. Tartaglia, H. Löwen, and E. Zaccarelli, Macromolecules **42**, 423 (2009).

[16] C. Mayer, E. Zaccarelli, E. Stiakakis, C.N. Likos, F. Sciortino, A. Munam, M. Gauthier, N. Hadjichristidis, H. Iatrou, P. Tartaglia, H. Löwen, and D. Vlassopoulos, Nat. Mater. **7**, 780 (2008).

[17] T. Voigtmann, arXiv:1010.0440v1 (2010).

[18] A. J. Moreno and J. Colmenero, J. Chem. Phys **125**, 164507 (2006).

[19] T. Voigtmann and J. Horbach, Europhys. Lett. **74**, 459 (2006).

[20] H. Watanabe, Prog. Polym. Sci. **24**, 1253 (1999).

[21] T. C. B. McLeish, Adv. Phys. **51**, 1379 (2002).

[22] N. McCrum, B. Read, and G. Williams, *Anelastic and Dielectric Effects in Polymer Solids*, (Wiley, New York, 1967).

[23] H. Meyer and F. Müller-Plathe, Macromolecules **35**, 1241 (2002).

[24] T. Vettorel, H. Meyer, J. Baschnagel, and M. Fuchs, Phys. Rev. E **75**, 041801 (2007).

[25] P. E. Rouse, J. Chem. Phys. **21**, 1272 (1953).

[26] B. H. Zimm, J. Chem. Phys. **24**, 269 (1956).

[27] M. Doi and S. F. Edwards, *The theory of Polymer Dynamics*, (Clarendon, Oxford, 1986).

[28] P. G. de Gennes, *Scaling Concepts in Polymer Physics*, (Cornell University Press, Ithaca, London, 1979)

[29] C. Bustamante, J. Marko, E. Siggia, and S. Smith, Science **265**, 1599 (1994).

[30] J. Käs, H. Strey, J.X. Tang, D. Finger, R. Ezzell, E. Sackmann, P.A. Janmey, Biophys. J. **70**, 609 (1996).

[31] C. K. Ober, Science **288**, 448 (2000).

[32] A. Semenov, Eur. Phys. J. E **9**, 353 (2002).

[33] J. Ubbink and A. Khokhlov J. Chem. Phys. **120**, 5353 (2004).

[34] D. C. Morse, Macromolecules **31**, 7044 (1998).

[35] S.-H. Chong and F. Hirata, Phys. Rev. E **58**, 6188 (1998).

[36] S.-H. Chong and W. Götze, Phys. Rev. E **65**, 041503 (2002).

[37] S.-H. Chong and F. Sciortino, Phys. Rev. E **69**, 051202 (2004).

[38] S.-H. Chong and M. Fuchs, Phys. Rev. Lett. **88**, 185702 (2002).

[39] S.-H. Chong, M. Aichele, H. Meyer, M. Fuchs, J. Baschnagel, Phys. Rev. E **76**, 051806 (2007).

[40] K. S. Schweizer and J. G. Curro, Adv. Chem. Phys. **98**, 1930 (1972).

[41] J. Baschnagel and F. Varnik, J. Phys.: Condens. Matter **17**, R851 (2005).

[42] J. Colmenero, A. Narros, F. Alvarez, A. Arbe, A.J. Moreno, J. Phys.: Condens. Matter **19**, 205127 (2007).

[43] A. Narros, Ph.D. thesis, Universidad del Paı́s Vasco (UPV/EHU), 2007.

[44] S. Capponi, A. Arbe, F. Alvarez, J. Colmenero, B. Frick, and J.P. Embs, J. Chem. Phys. **131**, 204901 (2009).

[45] W. Götze and M. Sperl, Phys. Rev. E **66**, 011405 (2002).

[46] M. Sperl, Phys. Rev. E **68**, 031405 (2003).

[47] E. Zaccarelli, G. Foffi, K.A. Dawson, S.V. Buldyrev, F. Sciortino, and P. Tartaglia, Phys. Rev. E **66**, 041402 (2002).

[48] F. Sciortino, P. Tartaglia, and E. Zaccarelli, Phys. Rev. Lett. **94**, 065703 (2005).

[49] A. J. Moreno and J. Colmenero, Phys. Rev. E **74**, 021409 (2006).

[50] V. Krakoviack, Phys. Rev. Lett. **94**, 065703 (2005).

[51] W. Paul, G. D. Smith, and D. Y. Yoon, Macromolecules **30**, 7772 (1997)

[52] S. Krushev, W. Paul and G.D. Smith, Macromolecules **35**, 4198 (2002).

[53] M. Bulacu and E. van der Giessen, J. Chem. Phys. **123**, 114901 (2005).

[54] M. O. Steinhauser, J. Schneider and A. Blumen, J. Chem. Phyis. **130**, 164902 (2009).

[55] M. O. Steinhauser, Mech. Time-Depend. Mater. **12** 291 (2008).

[56] L. Harnau, R. G. Winkler, and P. Reineker J. Chem. Phys. **102**, 7750 (1995).

[57] G. Allegra and F. Ganazzoli, Adv. Chem. Phys. **75**, 265 (1989).

[58] J. Colmenero and A. Arbe, Soft Matter **3**, 1474 (2007).

[59] J. K. Maranas, Curr. Opin. Colloid Interface Sci. **12**, 29 (2007).

[60] C. Lorthioir, A. Alegría, and J. Colmenero, Phys. Rev. E **68**, 031805 (2003)

[61] T. R. Lutz , Y. He, and M. D. Ediger, Macromolecules **36**, 1724 (2003).

[62] K. Niedzwiedz, A. Wischnewski, M. Monkenbusch, D. Richter, A. C. Genix, A. Arbe, J. Colmenero, M. Strauch, and E. Straube, Phys. Rev. Lett. **98**, 168301 (2007).

[63] A. C. Genix, A. Arbe, F. Alvarez, J. Colmenero, L. Willner, and D. Richter, Phys. Rev. E **72**, 031808 (2005).

[64] M. Brodeck, F. Alvarez, A. J. Moreno, J. Colmenero, and D. Richter, Macromolecules, **43** 3036 (2010).

[65] A. J. Moreno and J. Colmenero, J. Chem. Phys. **124**, 184906 (2006).

[66] A. J. Moreno and J. Colmenero, J. Phys.: Condens. Matter **19**, 466112 (2007).

[67] A. J. Moreno and J. Colmenero, Phys. Rev. Lett. **100**, 126001 (2008).

[68] G. S. Grest and K. Kremer, J. Chem. Phys. **92**, 5057 (1990).

[69] C. Bennemann, J. Baschnagel, W. Paul, and K. Binder, Comput. Theor. Polym. Sci. **9**, 217226 (1999).

[70] J. S. Shaffer, J. Chem. Phys. **103**, 761 (1995).

[71] T. Kreer, J. Baschnagel, M. Müller, and K. Binder, Macromolecules **34**, 1105 (2001).

[72] K. Kremer, G. S. Grest, and I. Carmesin, Phys. Rev. Lett. **61**, 566 (1998).

[73] J. T. Padding and W. J. Briels, J. Chem. Phys. **117** 925 (2002).

[74] V. Yamakov and A. Milchev, Phys. Rev. E **55**, 1704 (1997).

[75] V. Yamakov and A. Milchev, Phys. Rev. E **56**, 7043 (1997).

[76] R. Chang and A. Yethiraj, Phys. Rev. Lett. **96**, 107802 (2006).

[77] R. Chang and A. Yethiraj, J. Chem. Phys. **126**, 174906 (2007).

[78] K. S. Schweizer, M. Fuchs, G. Szamel, M. Guenza, and H. Tang, Macromol. Theory Simul. **6**, 1037 (1997).

[79] R. Kimmich and N. Fatkullin, Advan. Polym. Sci. **170**, 1 (2004).

[80] D. Frenkel and B. Smit, *Understanding Molecular Simulation*, (Academic Press, San Diego, 1996).

[81] M. P. Allen and D. J. Tildesley, *Computer Simulation of Liquids*, (Clarendon Press, Oxford, 1987).

[82] D. Marx and J. Hutter *Modern Methods and Algorithms of Quantum Chemstry (NIC series* vol.3) ed. J. Grotendorst, D. Marx and A. Muramatsu (Jülich: NIC) pp. 329-477 (available from http://www.fz-juelich.de/nic-series).

[83] R. Car and M. Parrinello, Phys. Rev. Lett. **55**, 2471 (1985).

[84] I. Teraoka, *Polymer Solutions: An Introduction to Physical Properties*, (John Wiley and Sons, New York, 2002).

[85] W. Paul and G.D. Smith, Rep. Prog. Phys. **67**, 117 (2003).

[86] F. Müller-Plathe, Soft Materials **1**, 1 (2003).

[87] J. Baschnagel *et al.*, Adv. Polym. Sci. **152**, 41 (2000).

[88] Discover 2.9.8/96.0/4.0.0: Forcefields Simulations, (Accelrys Inc., San Diego, CA, 1996).

[89] Cerius^2 4.8: Forcefield-Based Simulations, (Accelrys Inc., San Diego, CA, 2003).

[90] J. Colmenero, F. Alvarez and A. Arbe, Phys. Rev. E **65**, 041804 (2002).

[91] J. Colmenero *et al.*, J. Phys.: Condens. Matter **15**, S1127 (2003).

[92] A. V. Lyulin and M.A. J. Michels, Macromolecules **35**, 9595 (2002).

[93] A. V. Lyulin, N. K. Balabaev and M.A. J. Michels, Macromolecules **36**, 8574 (2003).

[94] P. V. Krishna Pant, J. Han, G. D. Smith and Richard H. Boyd, J. Chem. Phys. **99**, 597 (1993).

[95] W. Paul, D. Y. Yoon and G. D. Smith, J. Chem. Phys.**103**, 1702 (1995).

[96] W. Paul, G. D. Smith, D. Y. Yoon, B. Farago, S. Rathgeber, A. Zirkel, L. Willner and D. Richter, Phys. Rev. Lett. **80**, 2346 (1998).

[97] V. A. Harmandaris, V. G. Mavrantzas and D. N. Theodorou, Macromolecules **319**, 7934 (1998).

[98] M. Bulacu and E. van der Giessen, Phys. Rev. E **76**, 011807 (2007).

[99] G. S. Grest and K. Kremer, Phys. Rev. A **33**, R3628 (1986).

[100] C. Bennemann, J. Baschnagel, and W. Paul, Eur. Phys. J. B **10**, 323 (1999).

[101] M. Aichele and J. Baschnagel, Eur. Phys. J. E **5**, 229 (2001); *ibid.* **5**, 245 (2001).

[102] M. Aichele, S.-H. Chong, J. Baschnagel, M. Fuchs, Phys. Rev. E **69**, 061801 (2004).

[103] M. Rubinstein and R. H. Colby, *Polymer Physics*, (Oxford University Press, New York, 2003).

[104] M. Pütz, K. Kremer, and G. S. Grest, Europhys. Lett. **49**, 735 (2000).

[105] J. P. Hansen and I. R. McDonald, *Theory of Simple Liquids*, 2nd ed. (Academic Press, London, 1986).

[106] D. Chandler and H. C. Andersen, J. Chem. Phys. **57**, 1 (1997).

[107] W. Kob and H.C. Andersen, *Phys. Rev. E* **51**, 4626 (1995).

[108] J. Horbach and W. Kob, *Phys. Rev. B* **60**, 3169 (1999).

[109] P. J. Flory, *Statistical Mechanics of Chain Molecules*, (Oxford University Press, New York, 1988).

[110] P. J. Flory, J. Chem. Phys **13**, 453 (1945).

[111] P. J. Flory, J. Chem. Phys **17**, 303 (1949).

[112] O. Kratky and G. Porod, Recl. Trav. Chim. Pays-Bas **68**, 1106 (1949).

[113] F. Sciortino and W. Kob, Phys. Rev. Lett. **86**, 648 (2001).

[114] C. Donati, S. C. Glotzer, P.H. Poole, W. Kob, and S.J. Plimpton, Phys. Rev. E **60**, 3107 (1999).

[115] Y. Gebremichael, T.B. Schroder, F.W. Starr, and S. C. Glotzer, Phys. Rev. E **64**, 051503 (2001).

[116] S. C. Glotzer, J. Non-Cryst. Solids **274**, 342 (2000).

[117] N. Lačević, F. W. Starr, T. B. Schroder, and S. C. Glotzer, J. Chem. Phys. **119**, 7372 (2003).

[118] L. Berthier, G. Biroli, J. P. Bouchaud, L. Cipelletti, D. El Masri, D. L'Hôte, F. Ladieu, and M. Pierno Science **310**, 1797 (2005).

[119] L. Berthier, G. Biroli, J. P. Bouchaud, W. Kob, K. Miyazaki, and D. R. Reichman, J. Chem. Phys. **126**, 184503 (2007).

[120] A.J. Archer, C.N. Likos, R. Evans, J. Phys.: Condens. Matter **14**, 12031 (2002).

[121] T. Franosch, M. Fuchs, W. Götze, M. R. Mayr, and A. P. Singh, Phys. Rev. E **55**, 7153 (1997).

[122] M. Fuchs, W. Götze, and M. R. Mayr, Phys. Rev. E **58**, 3384

[123] M. Fuchs, I. Hofacker, A. Latz, Phys. Rev. A **45**, 898 (1992).

[124] M.J. Greenall and T. Voigtmann, J. Chem. Phys. **125**, 194511 (2006).

[125] D. Costa, R. Ruberto, F. Sciortino, M.C. Abramo, C. Caccamo, J. Phys. Chem. B **111**, 10759 (2007).

[126] W. Kob and H.C. Andersen, *Phys. Rev. E* **52**, 4134 (1995).

[127] J. Horbach and W. Kob, *Phys. Rev. E* **64**, 041503 (2001)

[128] T. Franosch, W. Götze, and M. R. Mayr, and A. P. Singh, J. Non-Cryst. Solids **235-237**, 71 (1998).

[129] M. Fuchs, J. Non-Cryst. Solids **172**, 241 (1994).

[130] K.S. Schweizer, E.F. David, C. Singh, J.G. Curro, J.J. Rajasekaran, Macromolecules **28**, 1528 (1995).

[131] M. Pütz, J. G. Curro, and G. S. Grest, J. Chem. Phys. **114**, 2847 (2001)

[132] W. van Megen and S.M. Underwood, Phys. Rev. Lett. **70**, 2766 (1993).

[133] T. Voigtmann, A.M. Puertas, and M. Fuchs, Phys. Rev. E **70**, 061506 (2004).

[134] L. Harnau, R. G. Winkler, and P. Reineker, J. Chem. Phys. **104**, 6355 (1996).

[135] L. Harnau, R. G. Winkler, and P. Reineker, Europhys. Lett.**45**, 488 (1999).

[136] S.-H. Chong, private communication.

[137] G. Szamel and E. Flenner, Phys. Rev, E **74**, 021507 (2006).

[138] S.-H. Chong and W. Götze, Phys. Rev. E **65**, 051201 (2002).

[139] A. Rinaldi, F. Sciortino, P. Tartaglia, Phys. Rev. E **63**, 061210 (2001).

[140] A. Arbe, J. Colmenero, M. Monkenbusch, and J. Colmenero, Phys. Rev. Lett. **81**, 590 (1998).

[141] H. P. Hsu , W. Paul, and K. Binder, Macromolecules **43**, 3094 (2010).

[142] W. Götze, J. Stat. Phys. **83**, 1183 (1996).

[143] M. Abramowitz and I. A. Stegun, *Handbook of Mathematical Functions* (Dover, New york, 1970 7th ed).

Publications

The results contained in this memory have been presented in the publications:

[A1] *Dynamic Arrest in Polymer Melts: Competition between Packing and Intramolecular Barriers.*

M. Bernabei, A. J. Moreno, J. Colmenero, Phys. Rev. Lett. **101**, 255701 (2008).

[A2] *The Role of Intramolecular Barriers on the Glass Transition of Polymers: Computer Simulations vs. Mode Coupling Theory.*

M. Bernabei, A. J. Moreno, J. Colmenero, J. Chem. Phys. **131**, 204502 (2009).

[A3] *From Caging to Rouse Dynamics in Polymer Melts with Intramolecular Barriers: a Critical Test of the Mode Coupling Theory.*

M. Bernabei, A. J. Moreno, E. Zaccarelli, F. Sciortino, and J. Colmenero, J. Chem. Phys. **134**, 024523 (2011).

[A4] *Chain Dynamics in Nonentangled Polymer Melts: A First-Principle Approach for the Role of Intramolecular Barriers.*

M. Bernabei, A. J. Moreno, E. Zaccarelli, F. Sciortino, and J. Colmenero, Soft Matter **7**, 1364 (2011).

[A5] *Static and Dynamic Contributions to Anomalous Chain Dynamics in Polymer Blends.*

M. Bernabei, A. J. Moreno, J. Colmenero, J. Phys. Condens. Matter (to be published) arXiv:1011.2402 (2011).